Magnetic spectroscopy and microscopy of functional materials

Dissertation
zur Erlangung des Grades
"Doktor der Naturwissenschaften"
am Fachbereich Chemie, Pharmazie und Geowissenschaften
der Johannes Gutenberg-Universität Mainz

vorgelegt von
Catherine Ann Jenkins
geboren in Pennsylvania, USA
Mainz, 2011

Die vorliegende Arbeit wurde in der Zeit von Nov 2007 bis Jan 2011 am Institut für Anorganische Chemie im Fachbereich Chemie, Pharmazie und Geowissenschaften der Johannes Gutenberg-Universität Mainz und in der Advanced Light Source, Berkeley angefertigt.

Mainz, 2011

Hiermit versichere ich, dass ich die vorliegende Dissertation selbständig verfasst und keine anderen als die angegebenen Hilfsmittel benutzt habe. Alle der Literatur entnommenen Stellen sind als solche kenngezeichnet.

Mainz, 2011

The ALS is a national user facility supported by the Department of Energy, Office of Basic Energy Sciences and operated by the University of California under contract No. DE-AC02-05CH11231.

Mainz, 2011

Abstract

Heusler intermetallics Mn_2YGa and X_2MnGa (X, Y=Fe, Co, Ni) undergo tetragonal magnetostructural transitions that can result in half metallicity, magnetic shape memory, or the magnetocaloric effect. Understanding the magnetism and magnetic behavior in functional materials is often the most direct route to being able to optimize current materials and design future ones.

Chapters include an introduction to the concepts and materials under consideration (Chapter 1); an overview of sample preparation techniques and results, and the kinds of characterization methods employed (Chapter 2); spectro- and microscopic explorations of X_2MnGa/Ge (Chapter 3); spectroscopic investigations of the composition series Mn_2YGa to the logical Mn_3Ga endpoint (Chapter 4); and a summary and overview of upcoming work (Chapter 5). Appendices include the results of a Think Tank for the Graduate School of Excellence MAINZ (Appendix A) and details of an imaging project now in progress on magnetic reversal and domain wall observation in the classical Heusler material Co_2FeSi (Appendix B).

Abstrakt

Mn_2YGa and X_2MnGa (X, Y=Fe, Co, Ni) mit Heuslerstruktur sind Halbleiter und Formgedächtnislegierungen. Um das Verhalten zu verstehen, muss man das magnetische Materialverhalten charakteresieren. Weiche Röntgenstrahlung von einer Synchrotron-Strahlungsquelle sowie die Advanced Light Source in Berkeley sind ideal für diese Untersuchungen geeignet.

Inhalt: Kapitel 1 ist ein Übersicht über die verwendeten Methoden und Materialien. Kapitel 2 gibt eine Einleitung zu Sputtering und Charakterisierungsverfahren. Kapitel 3 präsentiert Ergebnisse von X_2MnGa/Ge. In Kapitel 4 werden Ergebnisse zu Mn_2YGa präsentiert. In Kapitel 5 werden die Ergebnisse zusammengefasst. Appendix A beschreibt das "Think Tank"-Projekt. Appendix B beschreibt einen neuen Absatz für die Beobachtung der magnetischen Domänenwand in Co_2FeSi.

Contents

List of Figures

Chapter 1

Concepts

Functional materials are those with an industrial use or application, whether in energy such as magnetocaloric metals or in recording such as thin films with perpendicular magnetic anisotropy. Understanding the magnetism and magnetic behavior in functional materials is often the most explicit route to being able to optimize currently available materials for today's applications and to design novel ones for tomorrow.

Manganese based Heusler compounds are ternary intermetallics, often exhibiting a tetragonal distortion in the crystallographic unit cell. In this work the tetragonal phase transition in combination with controlled ferro- or ferrimagnetic behavior is exploited for applications from spintronics to multiferroic shape memory, with the eventual goal of integrating these phenomena in thin film vertical heterostructures with complex, magnetically mediated coupling. Synchrotron soft x-ray magnetic spectroscopy and scattering techniques are uniquely suited to elucidate the the competing effects in these materials as they provide detailed element-, valence-, and site-specific information on the coupled effects of structural ordering and magnetism as well as external parameters like temperature and pressure on the electronic structure.

1.1 Heuslers

The Heusler designation encompasses compounds with compositions XYZ or X_2YZ crystallizing in the $C1_b$ and $L2_1$ structure type, respectively [1]. Half Heuslers with XYZ can be more simply envisioned as modified zincblende (ZnS) where X^+ ions populate half the octahedral sites of a rocksalt YZ^- lattice, where Y and Z sit in tetrahedral and octahedral environments, respectively. The four interpenetrating pseudo-close-packed lattices of an X_2YZ compound have X ions in every octahedral site of a YZ lattice, and follow the Cu_2MnAl structure type and space group $Fm\overline{3}m$. X is most commonly a transition metal with more than a half-filled d-shell and the most electropositive element; Y is either a transition metal with a less than half-filled d-shell or a lanthanide with a more than half-filled f-shell; Z is a medium- to heavy-mass main group metalloid with up to a half-filled p-shell.

Strong $X - X$ bonding means that X and Y occupy independent magnetic sublattices [2], although $X - Y$ antisite disorder can occur when X and Y have similar atomic radii such as Ni and Mn [3]. X is typically of higher valence than Y and the combination will determine the site preference. If the transition metal X and main group Z are in the same period of the elemental table, their similar scattering coefficients lead to ambiguous diffraction patterns from conventional structural characterization and the tunable incident radiation of the synchrotron becomes necessary. The presence of larger Z components going down a periodic column is more strongly associated with ferromagnetism, although the ternary compound can be ferromagnetic despite a total absence of nickel, iron, or cobalt.

The class of Heusler compounds has several systematic advantages from the perspective of a material designer. Their magnetic properties such as net magnetization and Curie temperature are very well predicted by the linear Slater-Pauling rule as a function of valence electrons for non-close-packed crystal structures, that is, below about 8.5 electrons per atom [4]. Simple counting of valence

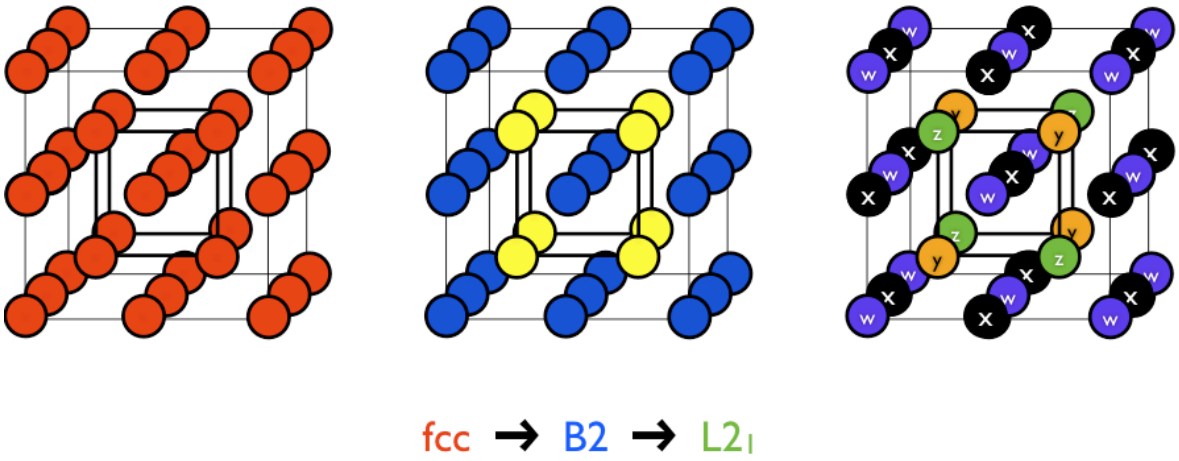

Figure 1.1: Development from face-centered cubic to the CsCl prototype to the Heusler structure removes the statistical definition of the atoms in a full alloy, leaving rigidly defined atomic positions and neighbors in a compound. Heusler compounds are primarily $AlCu_2Mn$ type for X_2MnZ composition or $CuHg_2Ti$ type for Mn_2YZ (w=x=X, y=Mn, z=Z or w=y=Mn, x=Y, z=Z, respectively, where lowercase letters represent lattice points and uppercase letters represent the occupancy.)

electrons includes s and d contributions from the transition metal and s and p contributions from the main group element. Intrinsic lattice matching around 6 Å for the entire class is a natural consequence of the lattice parameter being primarily determined by the Z atom. For example, series of compounds can be prepared between stoichiometries of Ni_2MnGa and Ni_2MnIn to isolate the structural effects of a larger lattice parameter since Ga and In are isoelectronic. Good agreement between experiment and density functional theory computations is often achieved because electrons in a Heusler structure are not strongly correlated. Finally, the range of electronic transport properties achievable with the tuning in a ternary compound is extensive, from conventional superconducting (Pd_2YSn) and heavy fermion (Fe_2VAl) compounds to semiconductors (PtMnSb), half-metals (Co_2MnSi) [5], and topological insulators (LaPtSb) [6].

Properties not fully generalized to the entire class of Heusler materials, *i.e.*, those that do vary according to composition, nonetheless divide cleanly into compounds obeying Co_2YZ behavior and those better governed by rules describing X_2MnZ compounds [7]. Magnetic ordering is most usually strongly localized at

a magnitude of about $1\mu_B$ per Co in Co_2YZ and $4\mu_B$ per Mn in X_2MnZ, unless X is Co or Fe and although smaller moments can also be induced on Ru, Rh, or Ni atoms by polarization of the conduction electrons as suggested by Mössbauer spectroscopy [8]. X_2MnZ compounds are often ferromagnetic with the manganese atoms interacting via and indirect exchange at an average separation of over 4 Å. The magnetic moment carried by the cobalt is slightly reduced from the expected value due to $p-d$ hybridization [9], with high spin polarization and ferromagnetism persisting if not being enhanced down to 65 atom nanoclusters strained far from their cubic Heusler structure [10]. Superconducting magnetometry (SQUID) indicates that the magnetic properties are retained far below room temperature [11].

The most extensively investigated set of purely ferromagnetic Heusler materials are based on cobalt and crystallize in the $AlCu_2Mn$ structure type as depicted in Figure 1.1. Co_2YZ where $Z =$ Si are most likely to show full $L2_1$ ordering and $Z =$ Al is most likely to exhibit some B2 disorder. Ferri- and antiferromagnetic Cr_2YZ compounds, in particular Cr_2MnZ, are predicted to be fully compensated [12] with the property of being spin polarized as further detailed in Section 1.3. $Z =$ P, As, Sb, or Bi can have a net spin magnetization of zero, consistent with the Slater-Pauling prediction from their 24 valence electrons per formula unit. The number 24 comes from the 12 occupied electronic states in a full Heusler compound, so it can be intuited that more or fewer than exactly two electrons per orbital allows for the unpaired spins associated with magnetism. Orbital magnetization is neglected in the Slater-Pauling rule of thumb since it is relatively much smaller in the cubic phase [13, 14], but in a material with tetragonal or higher anisotropy such as one where the magnetic shape memory effect is manifest, the orbital contribution can become considerable and can be directly measured by x-ray circular magnetic dichroism, as explained in Section 2.2.3.

Mn_2YZ take the $CuHg_2Ti$ structure type, with a site occupation as shown in Figure 1.1. They are often tetragonal, spin polarized, and partially or fully compensated ferrimagnets, and as such are the focus of the majority of this thesis.

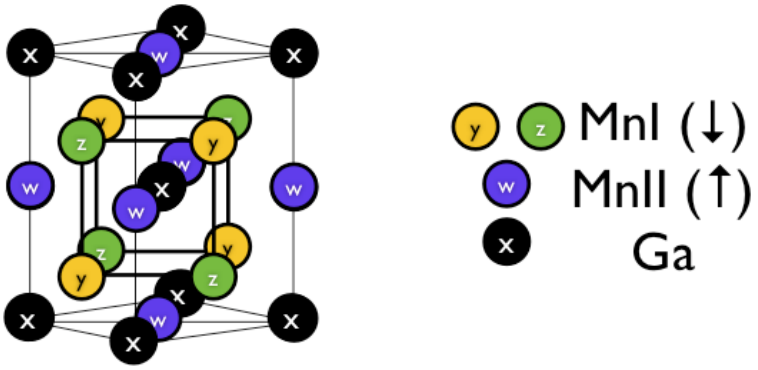

Figure 1.2: Drawing the unit cell a little differently shows how the DO_3 structure is developed, with a tetragonal distortion along [001] as the only change to achieve DO_{22}, of which ferrimagnetic Mn_3Ga is a relevant example.

The Mn^{3+} ion is the origin of both an energy-lowering Jahn-Teller structural distortion and a van Hove electronic instability. As consequence of this, the canonical magnetic shape memory compound Ni_2MnGa with approximately 10% magnetic-field-induced strain (MFIS, the mechanism of which is explained in Section 1.2.1) can be made to undergo 20% MFIS simply by doubling the manganese content as the source of both the spin-orbit coupling and the macroscopic strain. Spin-orbit coupling can be most straightforwardly considered as the inability of a spin to align itself with an externally applied field because of limits imposed by directional bonding within a lattice. A major thrust of the work is to fabricate a series of off-stoichiometric $Mn_{3-x}Y_xGa$ ($Y = Ni, Fe, Co, Ru$) in various forms to explore the further contribution of the elemental ferromagnet to the shape memory effect.

With only a slight uniaxial deviation from our structural prototype, the martensitic phase of the cubic Heusler structure can be understood. As an example, ground state Mn_3Ga can be visualized by redrawing the unit cell in such a way that the tetragonal distortion brings the face-centered cubic system not to B2 and $L2_1$ in sequence with progressively stricter definitions of atomic occupancy but from fcc to $L1_0$ (CuAl structure type; $P4/mmm$) to DO_{22} (Al_3Ti type; $I4/mmm$). Other systems based on the CuAl prototype, such as iron–platinum (FePt) and iron–palladium (FePd), are important for both their structurally and magneti-

cally anisotropic properties and for application in magnetic recording [15]. $L1_0$ compounds can be structurally equivalent to the face-centered cubic lattice when the a and c axes have the same magnitude but the occupancy of the faces and the corners are separately and not statistically defined, thus reducing the highest symmetry from cubic to tetragonal. They can be ferro- or antiferromagnetic and have high ordering temperatures, and so are of interest for industry.

1.2 Magnetostructural transitions

Structural phase transitions mediated by magnetic interactions and temperatures allow complex possibilities in the lattice behavior. Conventional shape memory is a heat driven manifestation of superelastic behavior in alloys of bronze, brass, and more complex unit cells. Magnetic shape memory shows the same superelastic behavior but the microscopic variant reorientation that leads to the macroscopic form change can be driven by an external magnetic field and not just a temperature gradient. The magnetocaloric effect (MCE) is a change in temperature with an external magnetic field, and is commonly observed in alloys exhibiting shape memory. The importance of these effects in magnetic refrigeration and actuation makes it appealing to search for a spectroscopic fingerprint that could be used to suggest future materials for exploration in either application.

1.2.1 Shape memory

The shape memory effect manifests as the ability of a material to repeatedly recover large (10% or more) plastic deformation and has applications including medicine (arterial stents), robotics (precision manipulators), and active (energy scavenging) or passive (seismic composites) vibration damping. Conventional shape memory materials can be driven by heating or applied stress, but in some magnetic compounds the magnetocrystalline anisotropy energy is coupled to the axis of tetragonal distortion, meaning that the recovery can now be triggered

by a third external variable, an applied magnetic field [16]. The mechanism is well known: stress-induced deformation is first accommodated by the diffusionless rearrangement of low symmetry crystallographic variants and then recovered by application of an external driving force in opposition to the initial stimulus [17]. Magnetic shape memory (MSM) is active below a martensitic transition temperature T_M and the magnetic transition temperature T_C, both of which can be compositionally tailored so the material is active at room temperature [18]. Heusler compounds can exhibit a ferro- or ferrimagnetic martensitic transition with lowered symmetry consistent with the MSM effect: indeed, the first known and best studied MSM compound is Heusler Ni_2MnGa [19]. Further examples are being discovered: Ni_2FeGa [20], Mn_2NiAl [21], and others. Ferromagnetic and ferroelastic (mechanical) order parameters are coupled in MSM compounds, allowing them to be known as multiferroic [22].

A martensitic transition has strict symmetrical requirements beyond traditional phase transitions [23]. It is a diffusionless, continuous-deformation, self-accommodating structural transition where the variants are separated by pseudomirror planar defects called twin boundaries. Atoms situated on a twin boundary sit in a double well of potential energy space, where each minimum is associated with satisfying the long range ordering position from one neighboring variant. Twin boundary motion is merely the stepwise propagation of the planar defect as a way for the material to increase the volume fraction of the variant that is favorably oriented with whatever external driving stress is being applied, stress or magnetic field. MSM occurs when, due to magnetocrystalline anisotropy coupling, the direction of tetragonal distortion to the magnetic easy axis, twin boundary propagation is energetically easier than magnetic rotation, expressed by the inequality $2\sigma_{tw} < K_u/\epsilon_0$, where σ_{tw} is the twinning stress and K_u is the anisotropy constant. This requires materials with high anisotropy and high defect mobility. Pure or stress-assisted magnetic field induced variant reorientation (MFIS or MIR) is the hallmark of MSM. Twin boundary motion is thermodynam-

ically reversible in the presence of a restoring force such as a spring.

Self-accommodating transitions also impose the structural constraint that the unit cell volume of the high and low temperature phases are to first order identical. Lower thermal hysteresis is correlated preferentially with a very slightly negative volume change as opposed to a very slightly positive change (less than 1-2% in magnitude in either case). There must exist a so-called habit plane in the austenite that also exists in the martensite, a requirement that is satisfied by the group theory constraint that the point group of the martensite be a subgroup of the austenite. Examples of phase pairs between which a contant-volume, self-accommodating transition can take place include cubic to orthorhombic and rhombohedral to monoclinic. In the most straightforward case of a cubic austenite to a tetragonal martensite, the habit plane indexed to the parent unit cell is $(101)_A$, and the twinning plane between symmetrically rotated martensitic variants is $(101)_M$, as indexed to the daughter unit cell. The most descriptive structural parameter is the c/a ratio in the parent and transformed phase, which for Ni_2MnGa is less than 1 (approximately 0.94, depending on the details of the modulation in the low temperature phase), and for inverse Heusler Mn_2NiGa is 1.21 [24]. The c/a ratio indicates the limit for the degree of mechanical strain $\epsilon = \epsilon(H, \sigma_{external}, T)$ possible as a result of transforming from a single variant with a tetragonal distortion to a single variant of orthogonal distortion by the motion of a single twin boundary: -6% for Ni_2MnGa and +21% for Mn_2NiGa. The reported 5M and 7M structures, denoting five-layer nearly tetragonal ($c < a = b$) and seven-layer orthorhombic ($c < b < a$) modulated martensite respectively, have after a decade of controversy been shown to be shuffles or nanotwins of a tetragonal but nonmodulated phase with $c > a = b$ [25]. If this is the case then the traditional detwinning procedure for single crystals by sequential compression is suspect, because total detwinning with the goal of a true single variant is more difficult in materials with a long c axis. This renders the precise determination of, for example, the anisotropy constants nontrivial, because single domain samples are not achievable.

Magnetic structure in MSM is characterized by a large drop in magnetization induced by the magnetoelastic martensitic transformation. Theoretical band calculations show that degeneracies in cubic symmetries $3d_{z^2}$ and $3d_{x^2-y^2}$ are lifted by a Jahn-Teller distortion and an abrupt decrease in the moment carried by the X atoms is predicted and observed [20, 26]. The band structure fingerprint of a Jahn-Teller distortion is where the density of states of the austenite phase at the Fermi energy E_F is divided into two peaks below and above E_F with the tetragonal distortion, lowering the total energy and permitting the evolution of the martensite. In both spin directions the E_F is on a shoulder of the DOS peak, giving high number density $N(E_F)$ and decreasing the structural stability. In the case of $X_2\mathrm{Mn}Z$ Heusler compounds, the Mn^{3+} Jahn-Teller ion has a strongly localized magnetization that can interact either parallel or antiparallel with neighboring Mn^{3+}, depending on the average separation distance. In $\mathrm{Ni_2MnGa}$, for instance, the exchange integral between the manganese atoms is negative with excess concentration, meaning they take on a character destructive to the total net moment of the material, and additional manganese substitution above 25at.% will lower the net moment. Manganese can be estimated to carry $4\mu_B$ per atom in both the $X_2\mathrm{Mn}Z$ (4.17 μ_B in $\mathrm{Ni_2MnGa}$) and Mn_2YZ compounds, although in the case of Mn_2YZ they often interact ferrimagnetically and a better estimate of the *net* magnetization comes from the valence electron count. $\mathrm{Mn_2NiAl}$, for example, has only a net moment of $1.48\mu_B$ per formula unit even in the austenite phase before the giant tetragonal distortion of $c/a = 1.22$ leads to a (predictably shape memory) martensitic phase with a total of $1.14\mu_B$ [21]. The relative volume fraction of austenite and martensite can also be estimated from a linear combination of the expected magnetizations. Magnetization as a function of temperature has a similar hysteresis although with different limiting values at high and low temperature as determined by the Curie temperature and saturation moment.

Many form factors support the expression of MSM: foams, polymer composites, single or polycrystals, epitaxial or freestanding films [16, 27, 28]. MSM in thin

films can be recognized by a sharp decrease in magnetization when a magnetic field is applied in the plane of the film because the phase transition is accompanied by a change in the easy direction of magnetization. The martensitic transition temperature T_M also decreases with application of a magnetic field as a function of the strength of the Zeeman energy in the phase stability space.

1.2.2 Magnetocaloric effect

Classical MCE is a measure of the isothermal change of the magnetic entropy in a system [29]. Because temperature and entropy are thermodynamic conjugates, it is equivalent to measure the adiabatic change in the temperature of a system induced by an external magnetic field. System entropy decreases when the magnetic moments align with an external field, releasing heat, and increases again when the field is removed and the moments are allowed to randomize, absorbing heat [30]. When the system in question absorbs heat from and expels heat to different environments, differential cooling can result. Cycles of heat flow with the goal of magnetic refrigeration (adiabatic demagnetization) are therefore reversible and energy efficient. Common materials that satisfy the requirements of permeability and heat effect include the perovskite manganites [31].

The formulaic description of MCE can be developed from the expression for the Gibbs free energy. From the Maxwell relation $(\delta S/\delta H)_T = (\delta M/\delta T)_H$ the following integral is obtained

$$\Delta S(T, H) = \int_0^H \left(\frac{\delta M}{\delta T}\right)_H dH$$

and the intrinsic entropy variable can be extracted from measurable quantities. Isothermal magnetometry can be used to measure ΔS and calorimetry (differential thermal analysis) for ΔT as independent confirmation against systematic errors. From the approximation $\Delta T_{ad} = T\Delta S/C$ where C is the heat capacity, it is apparent that a greater effect would come from a material undergoing some large

change of entropy coincident with but not necessarily a result of the magnetic reorientation, such as a structural distortion. Magnetic fields can have a significant effect on the heat capacity of a material, so it must be measured directly and not assumed to be a constant. A nearly simultaneous structural and magnetic phase transition would lead to the highest entropy change, so for example a shape memory compound with the stoichiometry tailored so that the T_C and T_M of the material were both around room temperature would be an ideal candidate. Chemically inhomogeneous samples of quintary Heusler $(Ni_{1-x}Co_x)_2(Mn_{1-y}Fe_y)Ga$ have a large entropy change across the range of temperatures where the phase transition locally takes place, allowing a wide range of operating temperatures [32]. When the magnetic and structural transitions occur coincidently the heat effect has been termed "giant MCE"[1] and its prototype materials are gadolinium and its alloys such as $Gd_5Si_2Ge_2$ [33]. The magnetic sublattices occupied by the symmetrically inequivalent Gd atoms have different ferromagnetic ordering temperatures so the magnetic transition is first order. An example of a material exhibiting MCE due to an antiferromagnet/ferromagnetic transition is $L1_0$-ordered, FeRh [34], but the AFM/FM transition has an associated volume change that makes it irreversible past the first expulsion of heat so it is not a candidate for application.

MCE material operation is optimized to slightly below ambient temperatures for cooling of buildings and to helium temperatures and beyond for ultracold physics. Therefore, the phase changes in the industrial material must be near room temperature to amplify the entropy change. Moreover, the transitions must be accessible with the workhorse of permanent magnets, NdFeB. Logistically, finding a change in temperature truly adiabatically requires a very fast magnetic field change which is not possible with superconducting magnets with higher fields, so for measurement a sample is brought in an out from between the magnetic poles quickly, and the field is allowed to remain constant.

[1] "Giant MCE" is as inappropriate yet pervasive a term for phase-transition-augmented MCE as "giant magnetostriction" is for the ferromagnetic shape memory effect.

1.3 Spintronics

Spintronics is an extension of traditional device physics with the added control dimension of the spin, with the dual advantages that since spin conduction has no eddy current losses it is more energy efficient and that the spin degree of freedom has a longer coherence length than the orbital, leading to longer spin lifetimes [35]. Spintronic devices include spin filters, injectors, sensors, hard drives, memory, read and write heads, spin transfer oscillators, and spin transistors (Datta-Das) and take advantage of the phenomena of magnetoresistance (MR) or spin momentum transfer (colloquially spin torque transfer, STT) [36].

It is impossible to understand spintronics without considering magnetism. Spintronic materials have an asymmetry in the population of spin up and spin down electrons available for conduction [37]. The asymmetry in electron population, or polarization, can be partial or full. Ideally spin polarized currents give perfect conduction of majority or minority electrons and inferior conduction of the other type and are required for current-induced magnetic domain wall motion and switching [38]. Partial polarization can be coincident with fractional magnetic charges; full polarization with integer numbers of Bohr magnetons. Materials with metallic conduction in one spin band and zero conduction (semiconducting behavior) in the other are called half metals (HM), and are exemplified by many Heusler compounds such as Co_2FeSi [39], as well as some oxides. Any electrons conducted are therefore from the majority state, and spin flip scattering to the minority state of the opposing electrode is prevented because there are no states to flip in to. In a strong ferromagnet with filled d band, $4s$ electrons conduct the charge, whereas in weak ferromagnets the d band is partially filled and conduction with both spins is possible.

The official definition of spin polarization P is from the density of states at the Fermi energy

$$P = \frac{D_{maj}(E_F) - D_{min}(E_F)}{D_{maj}(E_F) + D_{min}(E_F)}.$$

Practically, spin polarization is often measured by tunnel or giant magnetoresistance (TMR or GMR) values in thin film device stacks. A so-called magnetic tunnel junction (MTJ) for finding the TMR ratio is based on a ferromagnet/insulator/ferromagnet structure and the polarization is extracted from Julliére's formula

$$TMR\% = \frac{R_{ap} - R_p}{R_p} = \frac{2P_1P_2}{1 - P_1P_2}(\cdot 100)$$

where R_{ap} and R_p are the resistance when the ferromagnets are magnetized antiparallel and parallel, respectively, and P_1 and P_2 are the polarizations of the individual electrodes. In place of an insulator it has been shown that a semiconducting layer could also be used for spin injection as long as the interface resistances are compatible, but it is still difficult to achieve TMR values of higher than about 10% in Fe/GaAs/Fe without an additional interlayer [40]. GMR spin valves are based on a ferromagnet/metal/ferromagnet core structure and the polarization can also be extracted from a model based on the probability of interface scattering [41]. Spin polarized transport can be explored by spin-polarized photoemission [42] or scanning tunneling microscopy [43]. *Effective* spin polarization is decreased in a device relative to bulk values by interfacial roughness and enhanced by coherent tunneling through a band-selecting crystalline tunnel barrier such as MgO where of all the bands in the ferromagnetic electrodes, only the Δ_1-type can tunnel [44].

Until recently, thin film device structures depended on in-plane (left-right) magnetization, but for ultra-high density recording out-of-plane (perpendicular) magnetic anisotropy will be required to reduce the lithographic footprint of the spintronic nanopillars. Current-perpendicular-to-plane GMR (CPP-GMR) structures will eventually allow 1000 GBit/in^2 recording density compared to traditional MTJs with an order of magnitude lower (100 GBit/in^2). Current-induced magnetization reversal by spin momentum transfer is described by the Landau-Lifschitz-Gilbert equations and occurs when a ferromagnetic electrode is exchange

biased at an angle in order to exert a torque on a conduction electron.

The overall material parameters necessary to optimize a spintronic structure are a careful balance of competing metrics: higher thermal stability is linked with good data retention time, which is good, but also with a larger switching current, which is energetically expensive, and conflicts with the realization of higher speeds. The timescale of the precession of an excited magnetic moment is measured by the Gilbert damping α and must be simultaneously consistent with a long lifetime of the conducted spin but also allow angular momentum transfer through a finite electrode. For power dissipation considerations, it is also imperative to reduce the critical switching current J_{c0} for both spin directions to as many microamps as the feature size in nanometers: for example, 100 nm lateral pillars have an optimal switching current of only 100 μA [45]. The looming concern is then the bit stability, a function of bit volume and magnetic anisotropy, specified to have a statistically non-volatile state for ten years

$$\Delta_0 = \frac{K_u V}{k_B T} > 60$$

Since the switching current is proportional to $\alpha M_s^2 t$, where M_s is the net saturation magnetization and t the size dimension [46], it can be seen immediately that an ideal material for such a structure would have low damping, strong out of plane anisotropy, and a nearly compensated ferrimagnetic moment for the magnetic stability of a ferromagnet with the reduced stray field of an antiferromagnet. Permalloy (NiFe) is the benchmark for damping parameter and the high anisotropy $L1_0$ compounds and $L2_1$ Heuslers are immediately competitive, with high Curie temperatures and intrinsic spin polarization.

The first predicted HM ferromagnet was Heusler NiMnSb, followed quickly by HM ferrimagnet FeMnSb, and a later HM antiferromagnet Cr_2MnSb [12]. Cobalt-based Heusler compounds Co_2YZ are the only theoretically predicted half-metalic ferromagnets for which high spin polarization has been realized in magnetic tunnel

junctions. The gap in the minority density of states comes from hybridized Co and Y $3d$ orbitals [47] and is robust against substitutions provided Y has fewer valence electrons than Co [48]. Co_2MnSi, Co_2FeSi, and Co_2MnAl are well established as electrodes in CPP-GMR devices and MTJs [49]. Heusler MTJs deteriorate against temperature compared with CoFeB structures, falling from over 800% at 2K to only 250% at ambient [50]. This is not due to interface moments [11] but instead to the Fermi energy being too close to the conduction band and thermal fluctuations allowing spin flipping. Low coercivities of $H_c = 0.35$ Oe have been reported for $Co_2Fe_{0.4}Mn_{0.6}Si$ films fabricated by UHV sputtering [51].

However, cubic Co_2 compounds show in-plane magnetization in thin films and it should already be clear that PMA materials are more desirable for application when the out-of-plane magnetocrystalline anisotropy as from a tetragonal distortion can stabilize the bit against aspect ratio. This will have the advantage of scaling for high packing density, which is one of the key challenges for future magnetic random access memory (STT-MRAM) application. With the exception of cubic Mn_2CoSn, which is nonetheless half metallic with a saturation magnetization of 3 μ_B and a Curie temperature of 550 K in agreement with the Slater Pauling rule [22], $Mn_{2+x}Y_{1-x}Z$ compounds are highly spin polarized, strongly tetragonally distorted, and almost magnetically compensated across the entire compositional series. Electronic structure calculations of the endpoint compound (Mn_3Ga; $x = 1$) indicate a ground state with ferrimagnetic order and 88% spin polarization [52, 53]. The investigation of the magnetic properties of these samples by x-ray magnetic circular dichroism will help clarify the magnetic behavior and aid in optimizing sensors for a future application. Element- and symmetry-distinguishability is required for such ternary intermetallic compounds with independent magnetic sublattices. Site specificity will allow systematic studies of the correlations between the magnetic lattices with the spin polarization and bulk electronic structures.

1.4 Structure of the thesis

Fundamental work with the model systems of shape memory, magnetocaloric, and spintronic compositions is presented for context, with all new sample preparation and analysis methods. Synchrotron spectroscopy of novel compounds was also done with the aim of not only magnetic characterization but also of developing a systematic screening method for future examples of materials exhibiting any of the above effects. Symmetry lowering crystallographic transitions such as those involved in the MSM effect lead to an anisotropy in the magnetism that is visible to soft x-ray spectroscopy. In particular, the three independent axes of the vector magnet at ALS Beamline 4.0.2 is ideal to describe the anisotropic behaviors and coupling between the forces at play in a system: magnetic, electronic and spintronic, mechanical.

The chapter progression is as follows: an introduction to the concepts and material classes under consideration (Chapter 1); an introduction to sample preparation techniques and results and the kinds of characterization methods employed (Chapter 2); spectro- and microscopic explorations of X_2MnGa/Ge (X=Fe, Co, Ni) ribbons, thin films, and single crystals (Chapter 3); spectroscopic investigations of the composition series $Mn_{2+x}Y_{1-x}Ga$ (Y=Fe, Co; $1 > x > 0$) as well as Mn_2YGa (Y=Ni) (Chapter 4); summary, conclusions, ongoing, and upcoming work (Chapter 5). Appendices include the results of a "Think Tank" for the Graduate School of Excellence MAINZ (Appendix A); an imaging project now underway on magnetic reversal in the classical Heusler material Co_2FeSi and its relevance to polymer lithography nanodots (Appendix B).

Chapter 2

Samples and methods

Thin epitaxial films, bulk single crystals, melt-spun ribbons, and polycrystalline ingots of the desired ternary intermetallic compounds were produced for investigation. Extensive preliminary characterization in the laboratory was undertaken to detail the bulk magnetic, structural, and mechanical behavior of the materials. The opportunity to conduct synchrotron spectromicroscopy was primarily afforded at bending magnet and undulator beamlines at the Advanced Light Source, Lawrence Berkeley National Laboratory, operated by the United States Department of Energy and funded through proposals submitted to the Office of Basic Energy Sciences.

2.1 Fabrication

The highest quality intermetallic thin films were produced by magnetron sputtering (Ando, Sendai and Hitachi GST) and molecular beam epitaxy (MBE; Schmid, Berkeley). All bulk samples except for two were arc melted in Mainz (Felser), the exceptions being single crystalline pseudo-Fe_2MnGa which was grown and annealed in Sendai (Omori) and the Ni_2MnGa melt-spun ribbon and single crystals prepared in Spain (Barandiarán).

2.1.1 Thin film deposition

A high quality, well characterized epitaxial thin film is a model for systematically exploring the properties of a material. Magnetic Heusler compounds with a stable tetragonal distortion coupled to the magnetocrystalline anisotropy are candidates for low-energy, high-speed sensing and spintronic applications such as spin torque transfer and sonar transduction, but the theoretically predicted properties must first be demonstrated in devices or device-like heterostructures.

Several ferrimagnetic HM compounds based on manganese such as half-metallic Mn_3Ga and Mn_3Ge [52, 53] are promising materials with giant perpendicular anisotropy, in which the nearly compensated magnetic moment means a low magnetic energy must be expended during device actuation. Epitaxial thin film samples were synthesized by sputter and MBE, and the structural and magnetic behavior and transitions were explored with respect to prediction. Magnetic investigations with spin-polarized low-energy electron microscopy (SPLEEM) and, later, synchrotron-based soft x-ray spectroscopy were undertaken to detail the technological possibilities in these compounds as well as other isoelectronic, isofunctional binary and ternary intermetallics.

MSM compounds are challenging to grow in thin film form, either freestanding or constrained by an epitaxial substrate, and are pursued only in bulk form for the purposes of this thesis.

2.1.1.1 Sputtering

Magnetron sputtering is a physical deposition process from a vapor of ionized noble gas, typically for oxide or intermetallic films but also for carbon nanotubes or other organics. In an ultra-high vacuum (UHV) chamber with good base pressure, a target of the desired film material is held at a strong negative voltage in the presence of positively ionized argon gas. The argon ions are accelerated towards the target leading to an atomic cascade where one or more atoms from the target

overcomes the binding energy of its neighbors and flies in a line-of-sight path to an oppositely located substrate of heated glass or silicon. Because the flying target atoms ideally land to a good approximation on the substrate one at a time and not in clusters, individual monolayers of film are able to coalesce in a single crystalline way, and the resulting films are both atomically smooth and well-ordered.

An extremely relevant logistical concern for the preparation of atomically perfect films is strict adherence to cleanroom procedures (facemask, hairnet, UHV tool handling). Moreover, while the similar fabrication technique of pulsed laser deposition can theoretically be thought of as maintaining stoichiometric transfer between target and film, sputtering defies that pretense. All targets of binary or ternary compounds must be compositionally tailored to account for the sputter yield, a measure of the efficiency of the atomic cascade for each atom, which is roughly proportional to atomic mass and inversely proportional to the melting point. Alternatively, two or more targets can be simultaneously co-sputtered, with the power supplies to each gun tuned to adjust for the desired composition in the final film. This has the advantage of a widely accessible range of compositions but requires several sources in a single large chamber. As a third option, targets can be sequentially sputtered for a length of time consistent with the average stoichiometry and allowed to diffuse. Crystallinity of the resulting films can often be improved by post-annealing.

Early reports of $L1_0$-type Mn−Al [54] gave clues as to the growth sputtered epitaxial Mn_3Ga, which was first reported in 2009 by a group at Tohoku University Sendai [55]. Extraordinary Hall resistivity and conventional electrical resistivity proportional to T^3 at low temperatures indicated a one-magnon scattering process, consistent with a successful manifestation of the predicted high spin polarization [56]. The extraordinary hall effect is related to spin-orbit coupling and has more than a passing relation to perpendicular magnetic anisotropy. Films of Mn_3Ge were fabricated from single targets on the "Helicon 3" apparatus by the author in Sendai on chromium-buffered glass or heated gallium arsenide substrates

for between 60 and 90 minutes at between 200 and 500°C and under 0.1 to 2.0 Pa argon pressure as determined by a flow rate measured in standard cubic centimeters per minute (sccm), then further annealed at 300 or 500°C. Root mean square surface roughness was measured with an atomic force microscope (Spisel32) in differential mode as 9.617x10^{-2}, 2.629x10^{-1}, and 3.356x10^{-1} nm for 0.1, 0.3, and 0.5 Pa sputtering pressure, respectively. No characteristic structural peaks were observed by x-ray diffraction (XRD) but a non-zero out-of-plane magnetization was measured by vibrating sample magnetometry (VSM).

2.1.1.2 Molecular beam epitaxy

MBE is a thin film deposition method relying on stringently directed co-evaporation of solid sources. Baseline samples made with MBE are by far the most highly ordered, highly crystalline, and atomically perfect of any of the standard competitors (chemical vapor deposition, sputtering), at a cost of both time (factor of ten to a hundred or more times slower) and scalability. In so-called "Knudsen effusion cells", the elemental components of the desired film material are sublimated and directed along the long mean free path in a UHV chamber to the substrate of interest, often at fractions of a monolayer (ML) per second. Reflection high energy electron diffraction (RHEED) or low energy electron diffraction (LEED) is used to monitor the quality and crystallinity of the growth at all times. Reflectivity as a function of energy is a measure of the degree of monolayer completion as incident electrons are more likely to be diffracted by the atomic steps near an incomplete island. Composition is monitored by computing the film coverage of a calibrated ruthenium crystal placed next to each elemental doser and the evaporation modified accordingly.

An MBE growth chamber equipped with a low energy electron microscope (LEEM, [57], Figure 2.1) can be used to monitor the real-space evolution of the thin film deposition. LEEM is sensitive to the band structure of the film above the Fermi energy, and as such is very complementary to photoemission spectroscopy,

which is a probe of the band structure below E_F. At LBNL, the MBE system is further equipped with the capability to measure spin-polarized LEEM (SPLEEM, also see Section 2.2.4) down to 15 nm resolution for magnetic contrast. The origin of magnetic contrast in difference images between two polarizations of incoming electrons is the different absorption cross sections of majority and minority electrons due to spin splitting of the electronic orbitals. Strong spin polarization enables the discrimination of weak ferromagnetic signals. Upcoming improvements to the SPLEEM include aberration correction for an ultimate resolution nearer to 2 nm, the characteristic lengthscale of individual magnetic domain walls.

Considerations for MBE fabrication include a necessarily conducting substrate such a niobium-doped strontium titanate (STO:Nb) with large, atomically flat terraces (100-200 nm). Ultrathin magnetic layers are subject to suppression or complete annihilation of the magnetic properties expected from the bulk. The domain structure of the substrate is often imprinted on the first few monolayers of film. Perpendicular magnetic contrast was observed by the author at an electron energy of 5.7 eV in islands and films of Mn_3Ga grown at 25 to 350°C on Cu(100) (Figure 2.2), Fe(100), and 7x7 reconstructed Si(100). Post annealing at 400°C (nominal) was intended to give DO_{22} phase stability.

2.1.2 Bulk processing

Polycrystalline samples are necessary for novel compositions in order to obtain an orientation-averaged x-ray absorption intensity as discussed in Section 2.2.2. Stoichiometric quantities of the desired Heusler phase were arc melted under an argon atmosphere. The resulting ingots were then annealed at high temperatures in an evacuated quartz tube for a week (168h).

Single crystals are important for known compositions for a more accurate understanding of the anisotropic properties and macroscopic effects. Single crystals of off-stoichiometric $Fe_{48}Mn_{24}Ga_{28}$ were induction melted under argon, then grain grown with $\langle 100 \rangle_P$ parallel to the crystal faces and annealed at 1000°C for one

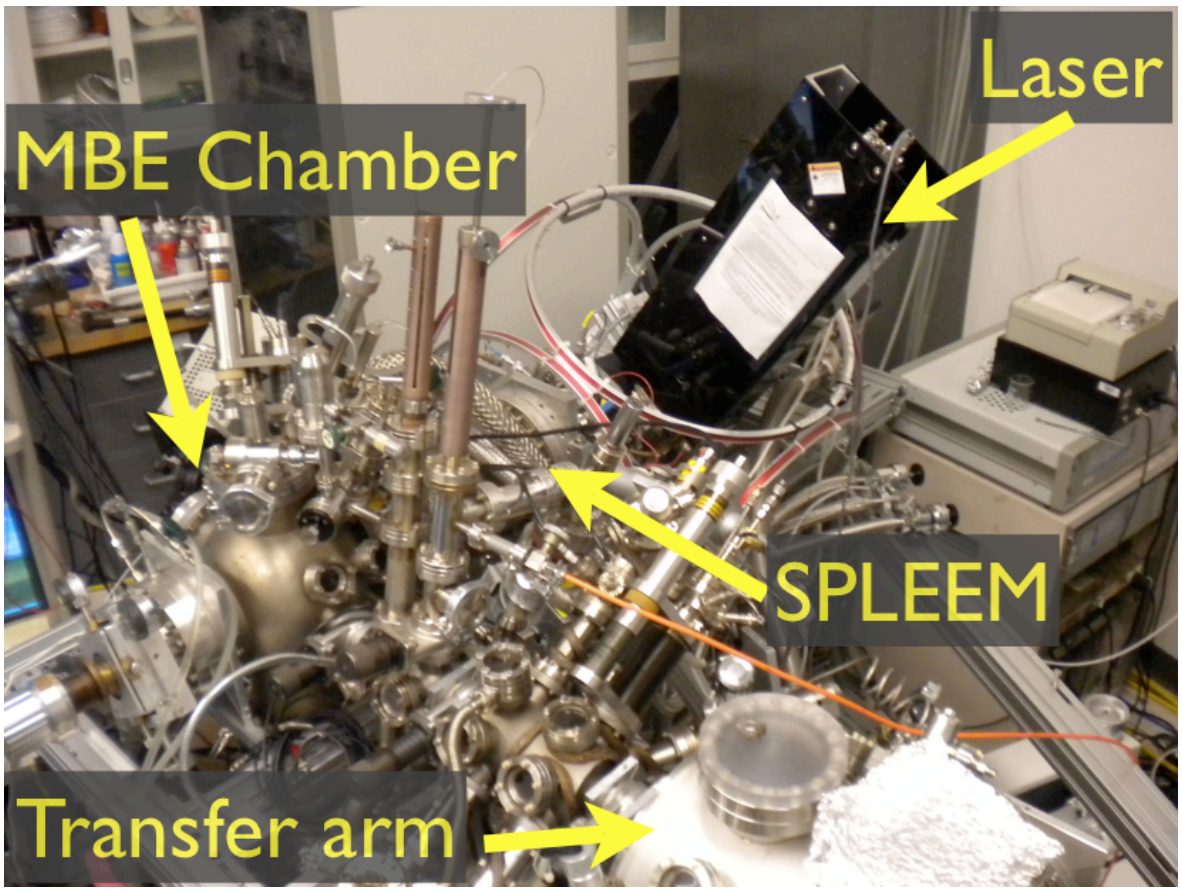

Figure 2.1: The Molecular Beam Epitaxy (MBE) deposition system at the National Center for Electron Microscopy (NCEM) in the Lawrence Berkeley Lab (LBNL). The laser is the source of the spin-polarized electrons for the spin-polarized low-energy electron microscope (SPLEEM), which images the in-plane magnetic contrast of thin films during deposition. Large magnetic windings (red) cancel the effect of the earth's magnetic field.

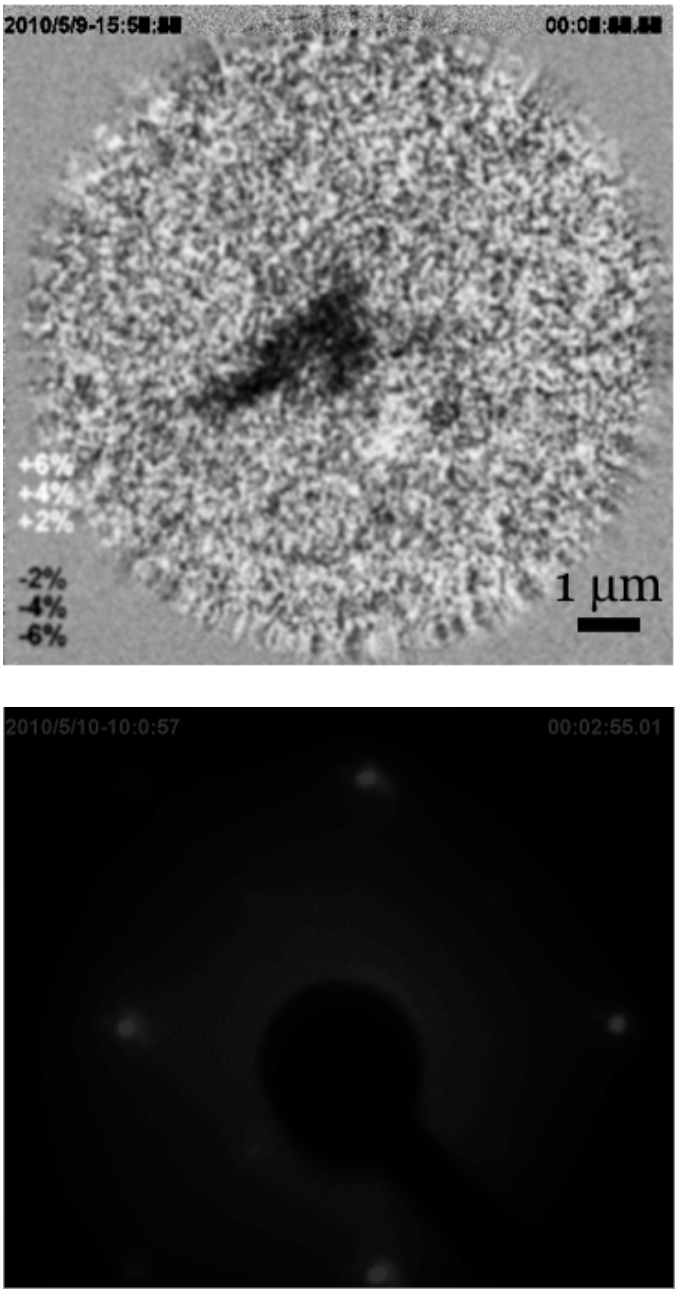

Figure 2.2: SPLEEM image (FOV=11 μm) showing magnetic contrast on an island in a ten monolayer Mn_3Ga film grown on Cu(100). Since the polarization of the probing electrons was out of plane, it is clear that the magnetic contrast is also out of plane. Additionally, in-plane polarized electrons show zero contrast. Low energy electron diffraction (LEED) image confirms the perfect orientation. With A.M. Quesada.

week and quenched in ice water [58]. Magnetic and structural transformations are shown by differential scanning calorimetry curves and SQUID measurements and the correct crystallographic structure by low-temperature XRD.

Polycrystalline ribbons of Ni−Mn−Ga were melt-spun in vacuum from an induction melted liquid onto a wheel surface with an average velocity of 17 m/s [59].

2.2 Characterization

University facilities are excellent resources for volume averaged structural, magnetic, and transport measurements. However, synchrotron characterization of materials gives element-, valence-, and crystallographic site-specific information unavailable to bulk methods. Spectroscopy and microscopy are complementary techniques and in combination provide excellent spectral and spatial information for the material system and micro/nanostructures of interest.

2.2.1 Beamlines and endstations

Beamlines at a synchrotron are classified according to how the characterizing radiation is delivered: bend and superbend magnets, undulators, or wigglers. Bending type magnets with "searchlight" radiation and polarized undulators are the most appropriate for soft-xray (250 eV to a few keV, 5 to 0.5 nm wavelength, carbon K to titanium K absorption edges) steering. Whereas wigglers have enhanced brightness compared to an undulator they also produce harder x-rays (a few keV to a few tens of keV) at wavelengths too short for the non-destructive surface science intended in this research. The Advanced Light Source at LBNL circulates at 1.9 GeV in 500 mA top-off mode with 272 bunches at 35 ps full width half max. A "beam" can be σ or π linearly polarized, 45° linear rotated (σ+π), or circularly polarized (σ+$i\pi$). In principle these four polarizations should be sufficient to completely determine the scattering tensor.

ALS beamline 6.3.1 is on a bending magnet with a resolving power $E/\Delta E$ =5,000,

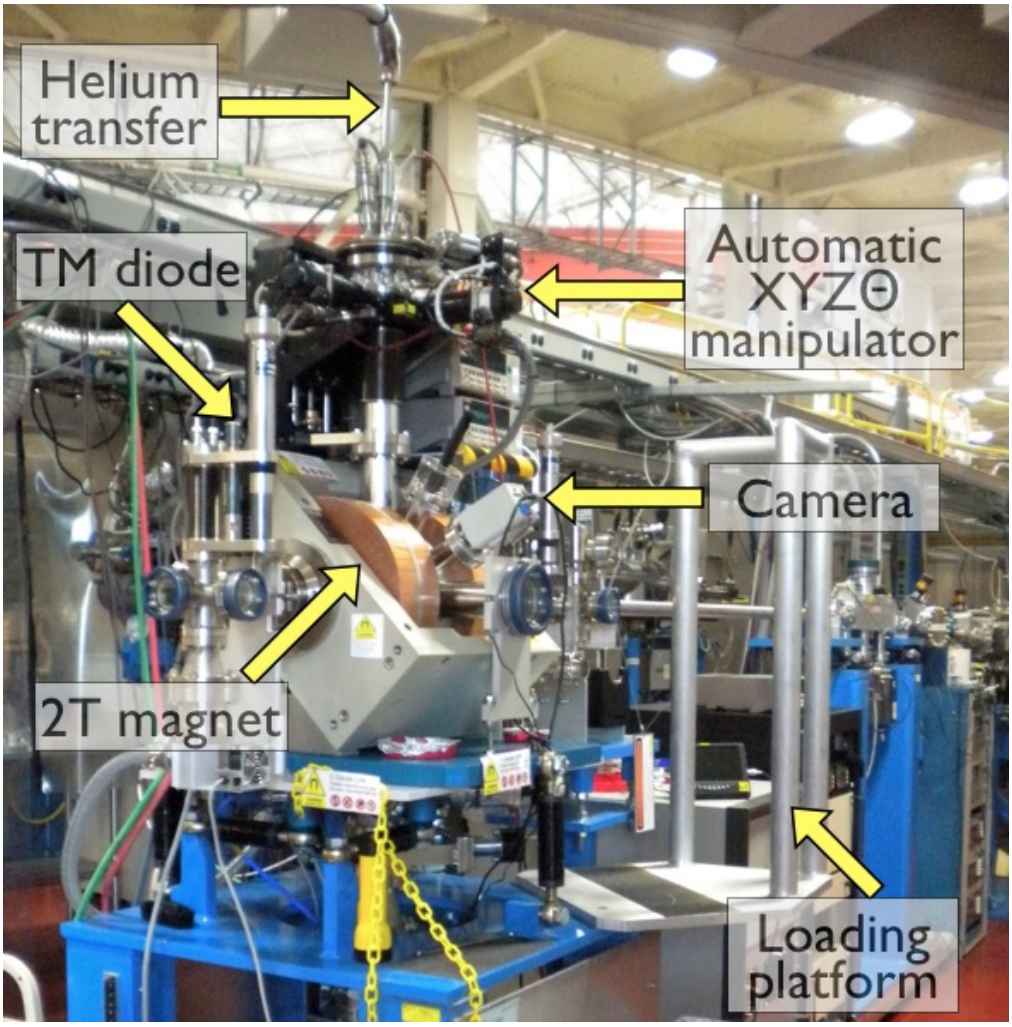

Figure 2.3: 2T endstation on BL6.3.1. Possible modes of measurement are transmission, fluorescence, and total electron yield mode. A setup with visible luminescence diodes is available on request.

a spot size of 500x500 μm, and a UHV chamber enclosed by a two Tesla dipole electromagnet with field parallel to the incident photon beam ([60] and Figure 2.3). Photon energy is set by diffraction from a variable line spacing blazed plane grating monochromator (PGM) optimized for operation between 400 and 2000 eV, comfortably including the transition metal L and the lanthanide M absorption edges, or the p to d and d to f electronic transitions where the asymmetry in the density of states associated with magnetism lies. Linear polarizations are unused and effective circular polarization is 65%. Soft x-ray beamlines such as this require only glancing incidence optics; hard x-rays are only diffracted by single crystal monochromators. Thin films, foils, and powders can be measured between 15 and 450 K in total electron yield, fluorescence, transmission, or visible luminescence modes [61]. Magnetic thin films are typically measured in grazing condition because the magnetization is easiest to saturate in the plane of the film. Polycrystals and brittle single crystals can be cleaved *in situ* to expose a UHV clean surface by an apparatus designed by the author (see Figure 2.4).

Beamline 4.0.2 is on a 50 mm period elliptically polarized undulator with an energy range of 400 to 1900 eV through the fifth harmonic, with photon energy determined by a variable-induced-angle PGM with a flux of 10^{13}/sec, 100 times greater than on BL6.3.1, and a resolving power of between two and five times better than on BL6.3.1 depending on the entrance and exit slit conditions. Polarization is continuously variable between horizontal, vertical, left circular, and right circular polarization. Linear polarization is complete (100%) and circular polarization depends on the magnitude of the off-axis component of the (odd) beam harmonic but the flux performance is optimized at 90%. Several endstations are available for this beamline including a 6 T superconducting magnet, an L-edge chamber with superconducting spectrometer, a 9 T scattering chamber, and an octupole vector magnet with up to 0.9 T in arbitrary directions for magnetic anisotropy studies (see Figure 2.5).

Beamline 11.0.1 is on a nearly identical insertion device as BL4.0.2 but the rele-

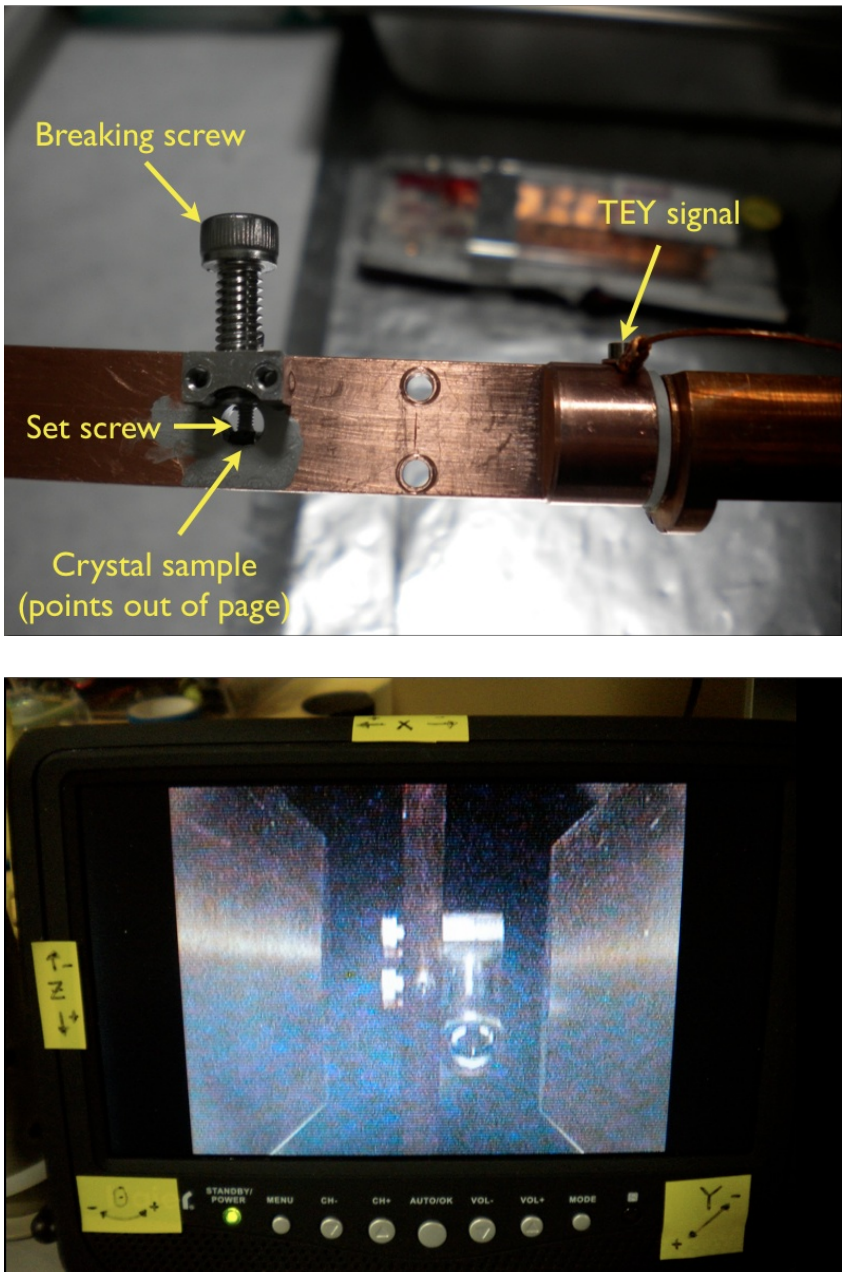

Figure 2.4: Crystal breaking apparatus employed to expose UHV-clean surfaces for poly- or single crystalline samples. A magnetic transfer rod with a hex head is used to turn the breaking screw against the resistance of the set screw and the curvature of the drilled hole where the samples is placed. In the lower image the poles from the 2T electromagnet are visible in the chamber.

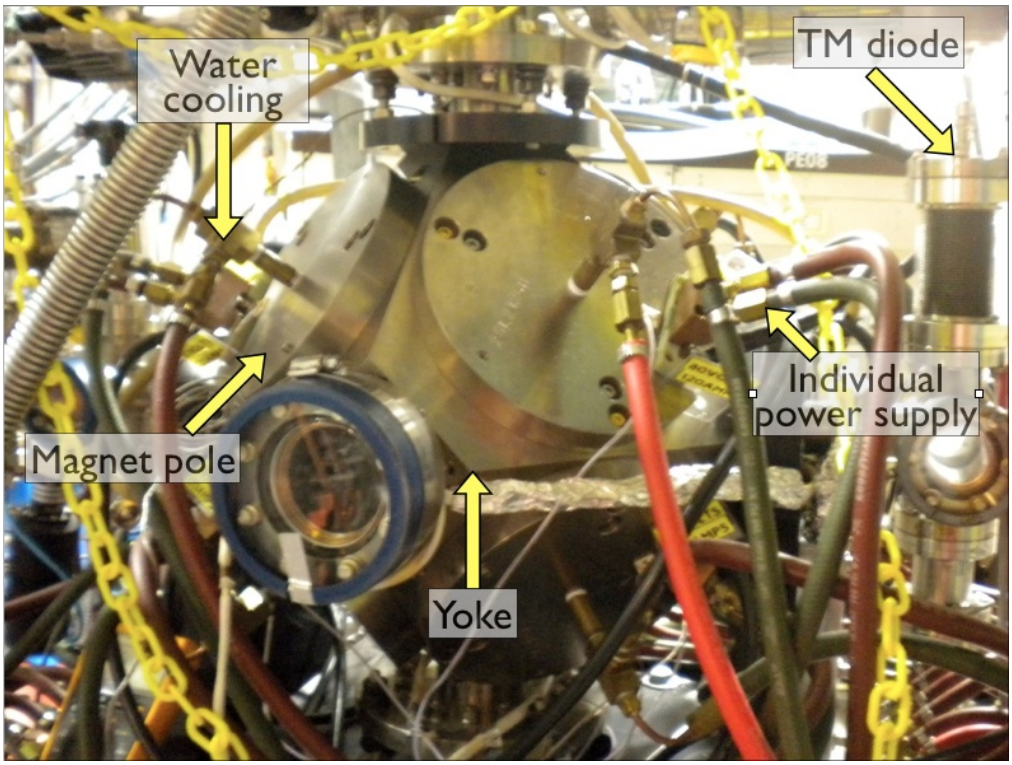

Figure 2.5: Octupole electromagnet endstation on BL4.0.2. Four pairs of magnet poles are arranged tetrahedrally and are controlled independently in order to allow application of magnetic field in an arbitrary direction up to a magnitude of 0.9 T.

vant endstation is an photoemission electron microscope (PEEM-3) with real-time and time-resolved (pump-probe) capabilities to measure magnetic and topographic sources of contrast in a surface-sensitive way at better than 50 nm spatial resolution. Emitted electrons are detected by CCD and the spot size is adjustable down to 10x10μm. Samples must be conductive and flat but can be sputter cleaned of surface oxides and annealed up to 800 K for surface reconstruction *in situ*. Cooling is limited to 105 K with nitrogen and 17 K with helium.

2.2.2 Absorption spectroscopy

Methods of spectroscopy can be broadly categorized into those that probe the electronic density of states below and above the Fermi level. Photoemission spectroscopy detects the binding energy of an electron based on the incident energy of the photon needed to dislodge it from its core or valence shell and the outgoing kinetic energy, and so measures the density of states below the Fermi level. In contrast, a simple model of absorption spectroscopy describes photon absorption as an excitation of a core electron into an unoccupied state, thus giving insight into the electronic density of states above the Fermi level. This crude division ignores diffraction, emission, reflection, and so on, and neglects the fact that true absorption is really only the imaginary component of the complex scattering tensor, but gives a useful beginning to the thought process.

Simply envisioned, x-ray absorption can be modeled as an electron being promoted from an inner shell upon absorption of an energetic photon, *e.g.* $2p^1$ to $3d^1$ above a background of white line intensity. More accurately, the model is of an *atom* being promoted from a ground state to a final state with a core hole, *e.g.* $2p^6 3d^n$ to $2p^5 3d^{n+1}$, or in the ligand field case the p band transitions to e_g/t_{2g} split d bands, or in transition metals the spin-orbit split p band transitions to the unequally occupiable d band. The difference becomes more pronounced when correlation effects between the electrons can no longer be neglected and a multiplet structure arises in the spectrum [62].

The transition probability from an initial ground state i to a final excited state f is written to first order by

$$T_{if} = \frac{2\pi}{\hbar}\langle f|H_{int}|i\rangle$$

H_{int} is the interaction Hamiltonian as a product of the momentum operator and the vector potential of the incident photon's electromagnetic wave. Second order corrections such as scattering, a process of resonant absorption and emission, allow (virtual) intermediate states and are represented by a higher order term. All resonant absorption spectra are normalized to the pre-edge and the integral of the L_3 and L_2 edges (the transition between $2p_{3/2}$ and $2p_{1/2}$ triplet ($S = 1$) and singlet ($S = 0$) to $3d$, respectively) is proportional to the number of d holes N_h. It can also be derived [62] that for a p to d excitation the absolute transition intensity is proportional in the dipole approximation to N_h and the charge sum rule of absorption spectroscopy is written as

$$\langle I_{total}\rangle = \langle I_{L3} + I_{L2}\rangle = \frac{2AR^2N_h}{15} = CN_h$$

where A and R are a constant and the radial matrix element, respectively, and N_h is estimated from a table. Only the radial rather than the angular matrix element is used because the one-electron manifolds created by the spin-orbit interaction are all spherically symmetric. Further corrections in the case of less than cubic symmetry deviate from the spherical approximation, complicating the situation enough to require mathematical models [63, 64, 65]. Qualitatively, X-ray absorption depends on orientation, polarization, and magnetization, where the difference between absorption of a spin up and a spin down electron (or left and right circularly polarized photons) is a measure of the asymmetry at the Fermi energy, or magnetic moment.

In particular for Heusler compounds the analysis is not trivial [66]. A satellite on the high energy slope of the L_3 absorption peak of the X in X_2YZ (3.8 eV above

Ni L_3 for Ni_2MnGa and 4.0 eV above Co L_3 in Co_2FeSi, for example) indicates the proper $L2_1$ Heusler ordering and is attributed to hybridization between X $3d$ and Z $2p$ states. Magnetic, structural, and electronic transitions are inferred from a change in the absorption spectra, such as the inference from the suppression of the L_3 satellite that the Ni $3d$ cubic degeneracies were lifted upon martensitic transition as predicted in [67].

2.2.3 Magnetic dichroism

Because the absorption intensity is proportional to the number of available unoccupied electronic states and spin flips are forbidden in a dipole transition, profiles of x-ray absorption intensity with respect to two opposite photon polarizations preserve information from the spin-resolved asymmetry at the Fermi energy. The difference is known as dichroism and represents the degree of asymmetry in spin-up and spin-down holes by polarization-dependent excitation, which has a quantifiable relationship to the spin magnetic moment [62]. X-ray magnetic circular dichroism (XMCD) as a technique was experimentally proven almost thirty years ago to extract quantitative $\langle M \rangle$ values [68] and information about the absolute element-specific spin and orbital magnetic moments down to within 5% of the actual value as low as 0.01 μ_B, better than polarized neutron studies [69].

XMCD in total electron yield mode is a measurement of the photocurrent due to the opposite photon polarizations and is used in the scope of this work. This mode is surface sensitive due to losses from limited mean free path of the low energy electrons that dominate the measured signal [70]. and the size of the dichroism scales as the cosine of the angle between the wavevector of the incident photons and the magnetization:

$$I_{XMCD} \propto P_{circ} \langle m \rangle \cos\theta$$

Therefore, when the photon angular momentum and the saturated sample magne-

tization are switched between parallel and antiparallel the difference is maximized. While it can be shown by symmetry that holding the magnetization constant and alternating the polarization at each measurement point and holding the polarization constant and flipping the magnetization at each measurement point are equivalent, functionally it is easier to do several runs of the latter and correct for (known and calibrated) incomplete polarization, drift, and a steplike background due to jumps in the absorption cross section.

All comments below refer to measurements on and derivations with respect to XMCD over the transition metal $L_{2,3}$-edge except where explicitly noted. There are several advantages, both experimental and analytical, for restricting the scope of the discussion. The white line intensity (integral) over the XAS edge is directly proportional to N_h, allowing a direct arithmetic of the number of filled spin-up and spin-down states as $10 - N_h$. The $2p$ to $3d$ transition has a small lifetime broadening (100 meV at the L_3 edge; 400 meV at the L_2) [71], and the cross term in the transition matrix between the $2p$ and the $4s$ states is small and can be ignored. L_2 and L_3 are more clearly separated than on the transition metal K edges where quadrupole effects must be accounted for, and the approximations used in developing the sum rules (similar to optical spectroscopy) are derived without relativistic or quadrupole corrections [72]. Rare earth elements such as gadolinium (Gd^{3+} in its most typical form) carry a strongly localized f-shell magnetization measured on the $M_{4,5}$ edge that is really just a perturbation of the electronic wave function, but the core level splitting of the $2p_{3/2}$ and $2p_{1/2}$ states are more fundamental to the transition metals.

Circularly polarized light can be thought of as being absorbed in a two-step process, where an electron from a spin-orbit split $2p$ band is excited by the absorption of the angular momentum of the incident photon. Holes (unoccupied states by definition) in the valence band then act through selection rules to detect the spin and orbital moment of the original state, since spin up (down) electrons preferentially excited by photons with angular momentum parallel (antiparallel)

to the magnetization are counted. Selection rules are pure quantum mechanics where the quantum numbers are defined as always. The orbital quantum number l is associated with the polar (θ) coordinate and is related to the conventional angular momentum $L = \sqrt{(l(l+1))}\hbar$ where l is 0 and the integers above. m_l is associated with the azimuthal (ϕ) contribution and $L_z = m_l\hbar$ and can be integers between and including $-l$ and $+l$. Disallowed transitions have no overlap in the wavefunctions but allowed transitions have $\Delta l = \pm 1$. Total angular quantum number $j = l \pm s$ must satisfy $\Delta j = -1, 0, +1$ and transitions between $j = 0$ states are not allowed.

The sum rules alluded to in Section 2.2.2 give the isotropic spin m_s and orbital m_{orb} magnetic moments per atom [73, 74]. Isotropic properties are found after orientation averaging or from a single measurement on a naturally isotropic sample such as a bulk polycrystal. The spin sum rule

$$\langle -A + 2B \rangle = \frac{C}{\mu_B} m_s$$

refers to: A, the area of the difference peak on the L_3 edge and defined negative; B, the area of the difference peak on the L_2 edge and defined positive; and C, the constant of proportionality from the charge sum rule above. Knowing that there are twice as many core electrons involved in the L_3 excitation as the L_2, an intuitive check is to see that with equal populations of spin up and spin down electrons the spin moment comes out to zero, as would be expected for a nonmagnetic material. The orbital moment rule refers to the same quantities:

$$-\langle A + B \rangle = \frac{3C}{2\mu_B} m_{orb}.$$

Late transition metals with more than half filled d-shells have parallel spin and orbital moments, with the highly anisotropic orbital moment almost always less than five percent of the magnitude of the isotropic spin moment but nonetheless crucial for understanding lattice interactions [75]. Anisotropic charge and spin

contributions are often ignored in high- or constant-symmetry materials but for MSM or other materials undergoing a magnetostructural transition with a strong crystallographic anisotropy this approximation can no longer be made, and angle-dependent measurements in anisotropic magnetic field such as the BL4.0.2 vector magnet are needed.

2.2.4 Photoemission electron microscopy

Photoelectron emission microscopy (X-PEEM, [42]) relies on the concepts of the previous two sections, XAS and XMCD, to produce images reflecting the spatial distribution of circular or linear dichroism in thin films or other flat surfaces. Electrons are emitted from a surface by a photon excitation process and are guided using aberration-corrected electron optics to a detector with lateral sensitivity. From a series of images below and above the absorption resonance, a map of differential contrasts is produced [76]. An energy spectrum can be taken at each individual pixel for a highly localized view of the spatial behavior of the spin and the orbital moments. Buried layers can be imaged, and coupled ferromagnetic and antiferromagnetic domains can be distinguished. Time resolution is possible by pump-probe techniques when the storage ring of the synchrotron is operating in two-bunch mode, and can resolve the dynamics of fundamental processes such as element-specific magnetization reversal and domain wall motion.

X-PEEM images are sensitive to contrast in local work function ϕ, local magnetization, energy dispersion due to finite exit slits, or topography. Images displaying magnetic contrast are a result of dividing either from raw images at the L_3 and L_2 edges at the same photon polarization or from two raw images at the L_3 edge but with opposite polarizations with the custom-coded PEEMVision software. In principle, with proper alignment this will normalize out all other sources of contrast such as chemical or thickness effects.

Twinning microstructures in bulk MSM single crystals or epitaxial thin films as a result of phase transformations due to external magnetic field or stress can

be recognized by a characteristic wedge or tweed surface topography coupled to magnetic domains. Polycrystalline materials can also exhibit twinning although the net effect is reduced due to the independent nature of the transformation between grains and will not be further pursued in this effort. X-PEEM will be used to clarify the dependence of the transition on the spatial arrangement of magnetic and structural domains, which has been comparatively little studied due to the small number of research groups world-wide capable of making films or crystals with high enough quality. Many vacuum and ambient microscopic methods face problems of surface sensitivity and spatial resolution. The author has designed a custom piezo-driven compression rig for *in situ* strain actuation of the MSM effect, shown in Figure 2.6.

Iron and manganese sublattice configurations will be measured with XMCD at the same time as the spatial extent of the magnetism is mapped. BL11.0.1 has the necessary spatial resolution, cooling capabilities, and vacuum conditions for a detailed study of the correlation between the magnetic atoms and the magnetostructural transformation behavior.

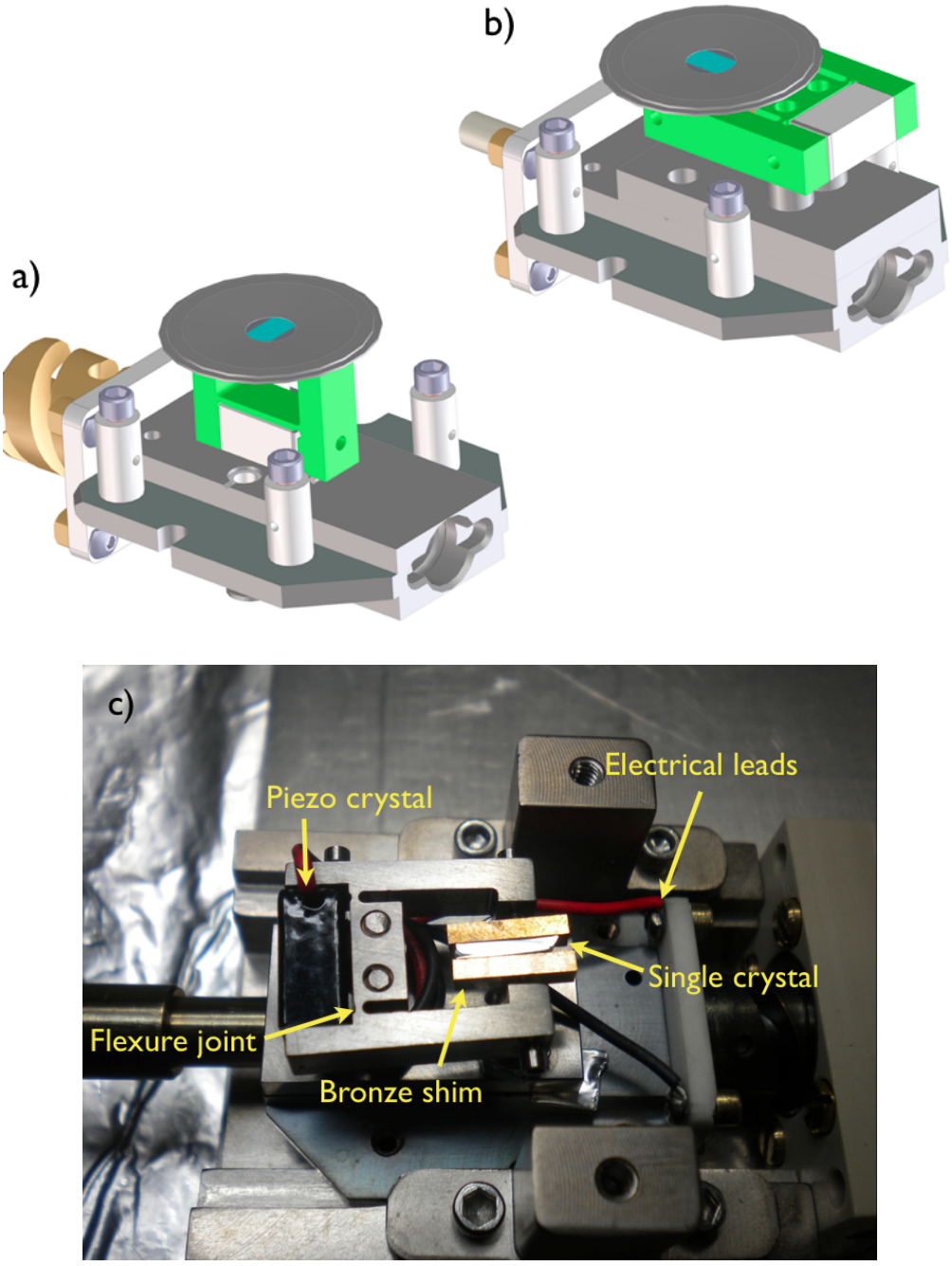

Figure 2.6: a) A three-dimensional rendering of the original design of the flexure joint, in green. b) a later optimization, with a greater mechanical advantage from the longer arms. c) A photograph of the strain actuator before loading into the vacuum chamber. The piezo crystal extends upon application of a voltage of up to +70 V, working over a mechanical advantage determined by the relative lengths of the arms in the flexure to compress the single crystal up to 2%.

Chapter 3

X_2MnGa/Ge (X=Fe, Co, Ni)

All MSM and spintronic Heuslers that undergo a magnetostructural transition have Ni_2MnGa as the prototype from which various stoichiometric deviations are developed (Sections 1.2 and 1.3). This chapter has three primary divisions, determined by the sequential substitution of adjacent elemental ferromagnets in the $3d$ transition metals. The first and second explore the magnetic spectroscopy of the main group element in the parent compound Ni_2MnGa with the goal of investigating the anomalous magnetizations found by polarized neutron diffraction on single crystals and melt-spun ribbons [59] and in spintronic Co_2MnGe to consider the origin of anomalous ferromagnetic resonance behavior in thin films [77]. The third explores the first magnetic spectroscopy and PEEM imaging of magnetic domain evolution in a novel MSM single crystal, Fe_2MnGa, as a function of both temperature and strain [58]. It is found that certain rules and predictors for the parent compound such as the origin of the magnetization are conserved in the iron-based daughter compound.

3.1 Ni_2MnGa

MSM compounds can be strongly affected by the degree of ordering, annealing and localization, where the Mn moments are strongly localized and the Ni moments are

Table 3.1: Transformation temperatures determined by differential scanning calorimetry (DSC) of the four samples under investigation. M_s and M_f are the martensite start and finish temperatures, respectively, and A_s and A_f are the same but refer to the austenite. TL11 and XA1 are single crystals and in all cases the modulation of the martensite is 7M. Note the small region of ferromagnetic austenite for the ribbons compared to the tens of Kelvin range for the single crystals.

Sample	M_s	M_f	A_s	A_f	T_C
A (ribbon as cast)	336	328	333	341	344 K
AR3 (Ribbon 18h; 600 K)	342	335	337	346	359 K
TL11 ($Ni_{52}Mn_{26}Ga_{22}$)	328	324	332	334	362 K
XA1 ($Ni_{49}Mn_{30}Ga_{21}$)	298	295	301	303	368 K

strongly delocalized (*i.e.*, participate in the conduction band) [78, 79]. In particular, the manganese exchange interactions can go from ferromagnetic to antiferromagnetic depending on average separation, which XMCD and neutron diffraction studies are well placed to elucidate [80, 81, 82]. Epitaxial films of Ni_2MnGa were first produced in Mainz in 2007 [83] and spectroscopic analysis of the magnetic behavior of the nickel and the manganese has been conducted [84, 85]. Previous studies on the behavior of the gallium in MSM compounds with XMCD have been limited primarily to delocalized K-edge ($3p$ and $4p$) measurements with no proven correlation to the quantitative local magnetic moment of the d states, although they suggest a large itinerant component of the magnetization and represent a measure of the degree of orbital magnetism [86, 87, 88].

The ideal sample for actuation has a ferromagnetic martensite, allowing magnetic actuation of the intermartensitic variants, but this is only found at room temperature in the compositions near Ni_2MnGa with significant off-stoichiometries chosen to retain a high magnetic moment. Four suitable samples were investigated here, two melt spun ribbons and two single crystals, with transition temperatures given in the table. Annealing the ribbons gives an average grain size of 45 nm and nearly ideal $L2_1$ ordering.

Single crystals were cleaved in air and mounted quickly to be measured in nor-

mal incidence. Spectroscopy at the Mn and Ni edges reveal indications of oxidation as expected after exposing the freshly prepared surface to air for the duration of the seconds between cleavage and pumping of the chamber. However, the oxidation leads to non-ferromagnetic oxides that do not contribute to the magnetic dichroism. The measured XMCD signal therefore might reflect properties of the bulk material. Ribbons were oriented for grazing incidence, although the much smaller range of ferromagnetic austenite even after annealing presented a slight difficulty with respect to precise temperature control. All samples were measured in an alternating field of 1 T at two temperatures after heating above the Curie temperature and cooling below M_s to erase any magnetic history effects. Measurement temperatures were 298 K for martensite and 351 K for austenite, with the exception of the as-cast ribbon, which was measured at 342 K to preserve the ferromagnetism. XAS/XMCD spectra were taken at the Ga L-edges and normalized to the L_3 pre-edge in order to provide a comparison to earlier K-edge data.

Earlier data indicated a strong XMCD signal on Ga-K in spite of a lack of true magnetic moment on Ga. Polarized neutron data was ambiguous since traces of moment at Ga sites were indeed observed, however, up to 4% Mn_{Ga} substitutional disorder is energetically highly probable in these compounds and the manganese could not be ruled out as the source. Gallium L-edge data from martensitic single crystal XA1 ($Ni_{49}Mn_{30}Ga_{21}$) are shown in Figure 3.1 and show a very small induced moment on the gallium edge. The qualitative characteristics of the XMCD signal are identical to L-edge XMCD of main group elements in other Heuslers, such as Ge in Co_2MnGe ([89], discussed below). L-edge data from martensitic as-cast melt-spun ribbons show no induced moment, consistent with the normal model of signal on the K-edge arising from p-band hybridization and not from a $3d$ moment.

Proper annealing is known to increase the magnetic moment carried by Mn and also to affect Mn K-edges more strongly than Ni or Ga [82], although this is not confirmed from the L-edge absorption.

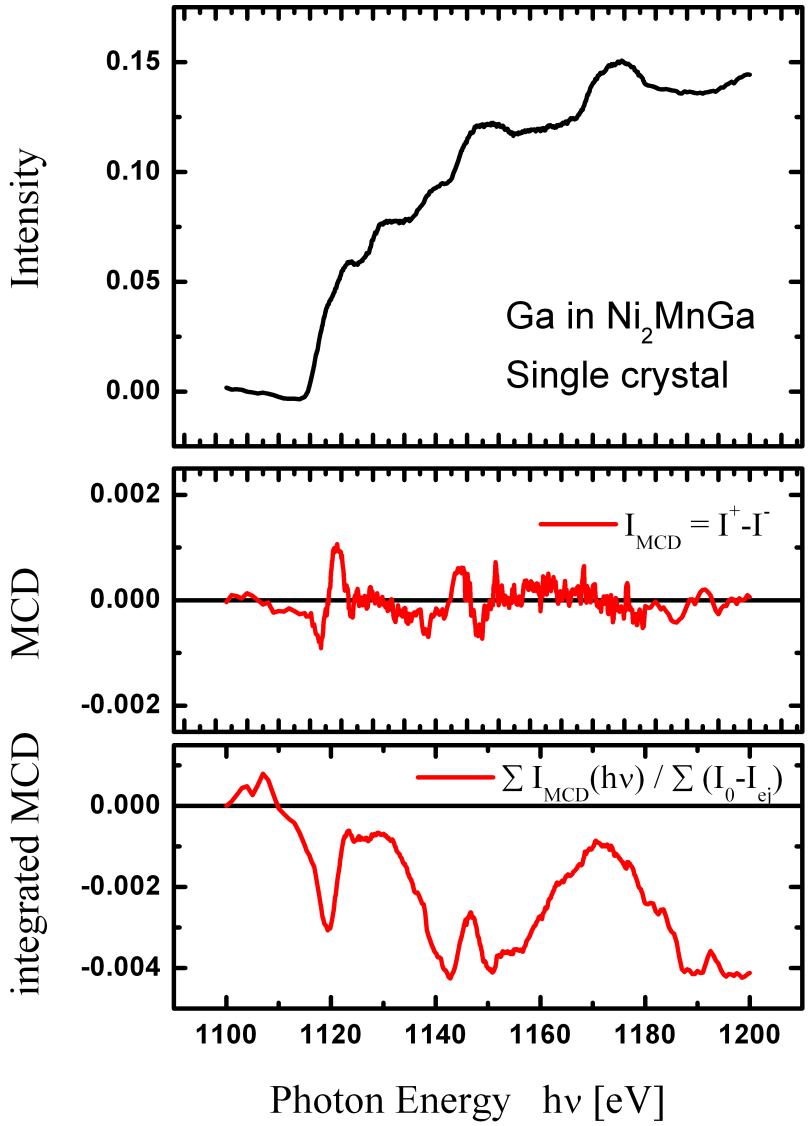

Figure 3.1: (top) X-ray absorption data from the gallium L-edge taken from single crystal XA1 ($Ni_{49}Mn_{30}Ga_{21}$) in the martensite phase. (middle) In the direct difference after normalization, a very small induced moment on the gallium edge is visible. (lower) The progressive integration of the XMCD signal shows the cumulative signal and is another indication of the orbital moment.

3.2 Co_2MnGe

Fully half metallic Heusler materials for spintronic applications have technological relevance for future hard disk drive read sensors, but such thin films must be fully characterized and synthesized in a manner compatible with industrial processing techniques such as sputtering (Section 2.1.1.1). Co_2MnGa and Co_2MnGe are promising for CPP-GMR applications because of their low damping [51], high moment and high Curie temperature. Co_2MnGe in particular requires a low annealing temperature and shows significant advantages over similar transition metal compounds [90], and shows an anomalously high GMR in Ge-rich compositions. Therefore, we detour briefly from the gallium series to a substantially similar compound and consider Co_2MnGe in detail.

Recent ferromagnetic resonance (FMR) measurements found an anomalous source of damping in sputtered films of CMG, where the field-swept linewidth vs. frequency was observed to exhibit a bump-like nonlinearity at intermediate frequencies for certain compositions and annealing temperature [77]. This anomaly can be attributed to a significant density of antiferromagnetically aligned spins on the Ge sites. Recent band structure calculations [14] predict only small amounts of negative spin density and an infinitesimal magnetic moment, which is not enough to explain the FMR results. Indeed, prior XMCD studies disagree on whether there is a moment on the Ge at all [91], and even in cases where a moment is observed, it is not quantified [89].

Element-specific XMCD was used to investigate the relative magnetic moments of the Co, Mn, and Ge in polycrystalline $(Co_2Mn)_{1-x}Ge_x$ ($0.32 > x > 0.20$; CMGe) samples as prepared by DC magnetron sputtering on glass substrates at Hitachi. The samples are capped with 2 nm Cu and 2 nm Al to prevent oxidation and corrosion, annealed after deposition in vacuum at 245°C or 300°C for 5 hours, and characterized in the laboratory (Mo K_α XRD, SQUID, perpendicular FMR from 1 to 28 GHz) before being brought to the beamline. Earlier samples were fabricated

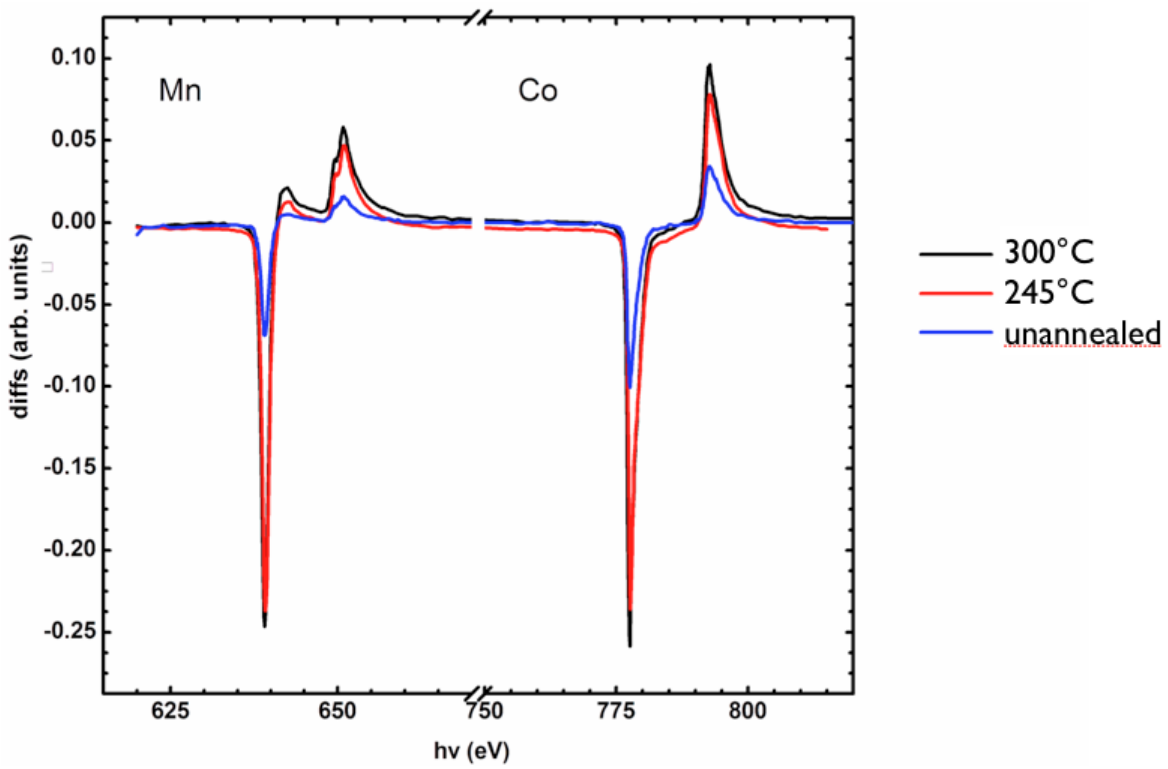

Figure 3.2: Comparison of the annealing treatments on the transition metal elements in a thin film with Ta/Cu buffer layer, 10 nm CMGe with 20 at.% Ge, and a Cu/Al cap structure. The 300°C anneal clearly produces the highest magnetic moment in the Mn and the Co but might promote B2 type disorder.

with 5 nm Cu and 5 nm Ta capping layers to replicate those in the literature [77] but soft x-ray spectroscopy on the buried layers is limited in signal intensity. Samples were considered to be saturated at the 0.5 T alternating field of the vector magnet because extensive SQUID measurements showed that irrespective of composition, H_c remained 10-20 Oe, with H_k of the same order.

Figure 3.2 shows a comparison of the annealing treatments on the transition metal elements in a thin film with Ta/Cu buffer layer, 10 nm CMGe with 20 at.% Ge, and a Cu/Al cap structure. The 300°C anneal clearly produces the highest magnetic moment in the Mn and the Co but might promote B2 type disorder so a slightly lower annealing temperature was determined to be optimal for applications. No significant evolution in the moment per atom is observed between x values of 0.20 and 0.32, or within 5 at.% of the Heusler stoichiometry.

Figure 3.3 shows representative absorption and dichroism data from a thin film with Ta/Cu buffer layer, 10 nm CMGe with 26 at.% Ge, and a Cu/Al cap structure, annealed for optimal conditions, 5 h at 245 °C. To achieve the displayed signal to noise ratio where a 0.1-0.2% magnetic signal is visible, 8 spectra were averaged, in contrast to the transition metal signal where a 30% difference was observed after a single spectrum. This data shows unambiguously that a magnetic moment is induced on the L edge of Ge in the Co_2MnGe structure, with a magnitude of 0.033 μ_B spin and 0.0062 μ_B orbital moment per d-hole, corrected for grazing incidence and 90% circular polarization of the incident photons. In the germanium as well, no significant evolution in the moment per atom is observed between x values of 0.20 and 0.32. The origin of the moment is left for future structural investigations, whether it is from the ordered Heusler bulk, grain boundaries in the polycrystal, or the interface with the Cu cap.

3.3 Fe_2MnGa

Substituting the elemental ferromagnet iron for nickel in the prototypical MSM Heusler gives Fe_2MnGa. Previous work has shown a dramatic magnetic-field induced strain in annealed off-stoichiometric polycrystals of this material ($Fe_{50}Mn_{22.5}Ga_{27.5}$), with a theoretical performance up to $(c-a)/c = 33.5\%$ [92]. The predicted performance dwarfs the theoretical strain achievable in Mn_2NiGa (about 20%, [93]) or Ni_2MnGa (about 10%, [25]) but the magnetic structure and predicted half-metallic behavior are only beginning to be studied. It can be anticipated that such large deformation will be associated with dramatic changes in the electronic structure, possibly also visible by spectroscopy.

Several important differences between ideal Ni_2MnGa and derivative Fe_2MnGa were already apparent before this study was undertaken and motivated the interest in the new compound above and beyond the fact of the enormous strain. The c/a ratio of the low temperature phase is 0.927 and the transformation is associated

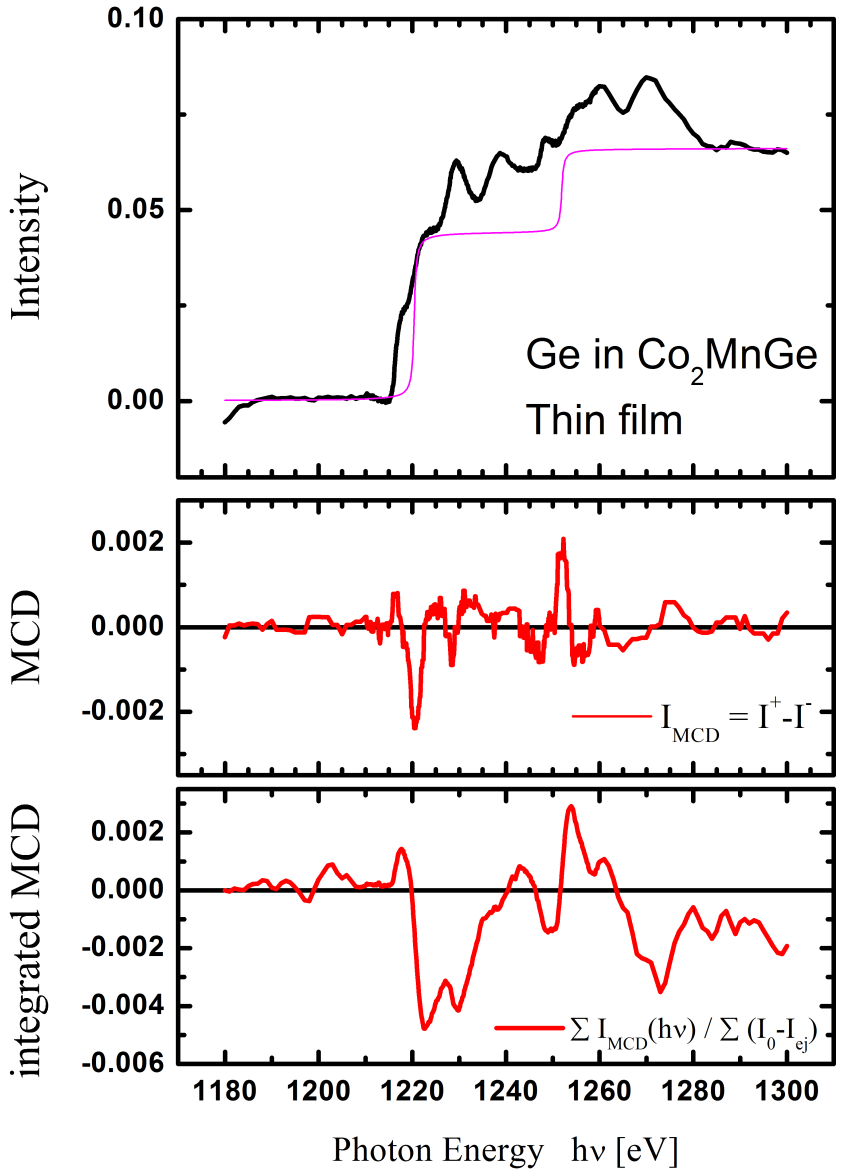

Figure 3.3: (top) X-ray absorption data from the germanium L-edge taken from a thin film with Ta/Cu buffer layer, 10 nm CMGe with 26 at.% Ge, and a Cu/Al cap structure, annealed for 5 h at 245 °C. (middle) In the direct difference after normalization, a very small induced moment on the germanium edge is visible. (lower) The progressive integration of the XMCD signal shows the cumulative signal and is another indication of the orbital moment.

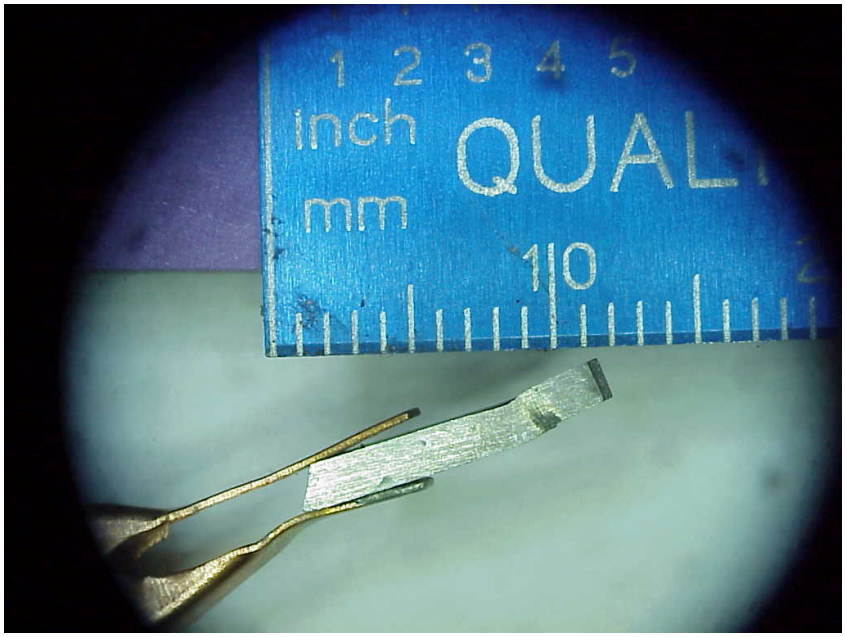

Figure 3.4: A polished, multi-variant single crystal of off-stoichiometric Fe_2MnGa deforms macroscopically in response to a low (1 MPa) shear stress.

with a unit cell volume change of $+1.35\%$, opposite to the parent compound which shrinks very slightly upon transition [58]. Magnetization vs temperature curves in the zero-field-cooled and field-cooled states indicated that the martensite has a *higher* saturation magnetization than the parent phase, which is again contrary to expectations from Ni_2MnGa. Further, the DOS at E_F goes *up* by an order of magnitude with martensitic transition, so the electrical resistivity is found to decrease in direct opposition to all previously known MSM Heuslers [92].

A multi-variant single crystal of $Fe_{48}Mn_{24}Ga_{28}$ with $M_s = 213\ K$, $M_f = 162\ K$, $A_s = 231\ K$, and $A_f = 294\ K$ (thermal hysteresis of about 80 K) was grown as described (Section 2.1.2), and preliminary bulk magnetometry and structural studies were performed. As with Ni_2MnGa, alloying can tailor the magnetic and structural transition temperatures independently, but in the ideal case a compound is found where the ferromagnetic martensite transforms directly to a ferromagnetic austenite, which only with further heating becomes paramagnetic. As is also the case in Ni_2MnGa, several distinguishable modulations of martensite are often

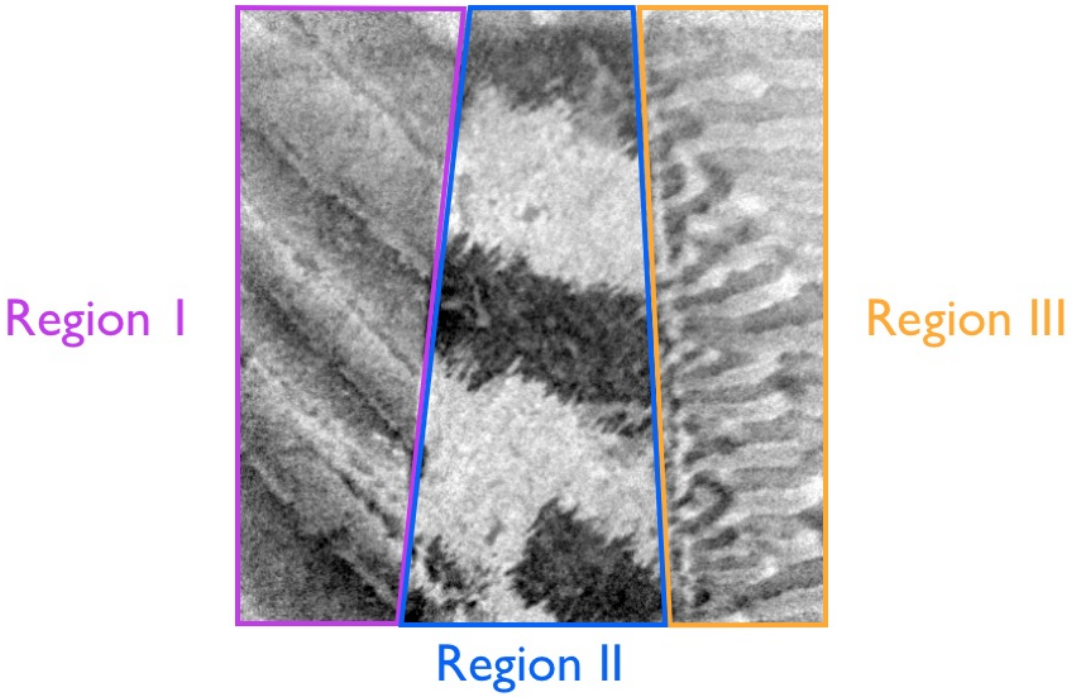

Figure 3.5: A representative region of the polished Fe_2MnGa surface. The field of view is 36 μm and the contrast comes from dividing two images taken at the Fe L_3-edge (707.5 eV) in positive and negative circular polarization. The morphology of Region I is considered to be "band" domains and that of Region II is "maze-like" in the language of Lai et al (see text). The visible structure of Region III is referred to as a bunched twill.

simultaneously available due to either compositional inhomogeneities or defect history, and can be distinguished from the surface topography [94]. Surface domains reflect the distribution of volume domains in materials with high enough coupling between the magnetization and the magnetocrystalline anisotropy to overwhelm the energetic contribution to the surface stray fields [95]. This is true in Ni_2MnGa and therefore by extension Fe_2MnGa, where the coupling is stronger, so surface-sensitive domain observation is informative regarding the volume domain behavior here as well. Temperature dependent observations of the twinning structure will give more information as to the coupling behavior between the magnetism and the tetragonal distortion. Magnetic field dependent observations of the twinning structure, while highly desirable, are not possible in a system of electron optics such as PEEM-3, so magnetic field dependence is limited to spectroscopic analysis.

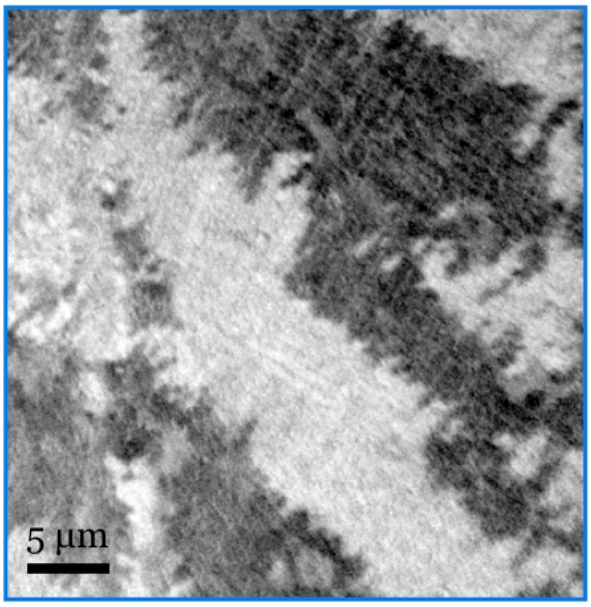

Figure 3.6: The maze-like variant of Region II can be observed over a large fraction of the surface. This degree and morphology of magnetic contrast can be recognized as having a crystallographic c-axis [001] out of the plane of the page. FOV 36 μm.

Room temperature magnetic domains are displayed in Figure 3.5, an XMCD image based on the division of two images taken at opposite photon helicity at the absorption edge of iron. The field of view of 36 μm was chosen to encompass several variants, labeled I, II, and II, respectively, although the majority of the surface polished to 0.1 μm with diamond paper manifested more like in Figure 3.6. Region boundaries are well defined by abrupt changes in the domain structure across the twins. All magnetic contrast is carried by the iron and none by the manganese, superficially opposite to what would be predicted from analogy with Ni_2MnGa but explained by the sample preparation. Photoemission is a surface-sensitive technique and the higher reactivity of the manganese atoms and the *ex situ* polishing together mean that the top 2 nm of manganese have been oxidized. Indeed, (equally surface sensitive) spectroscopy indicates strongly localized character such as would be seen in MnO instead of metallic Mn as would be expected in a Heusler structure. The less reactive iron suffers less oxidation and preserves the magnetic domain structure with origins deep in the crystal, beyond

the top few monolayers subject to oxidation in the brief period between polishing and loading into the vacuum chamber.

The morphology of Region I is considered to be "band" domains and that of Region II is "maze-like" in the language of Lai and colleagues [95]. This coincides with structural variants of the single crystal with the c-axis ([001]-direction) pointing in-plane (left-right) and out-of-plane, respectively. For the purposes of this work the visible structure of Region III is referred to as a bunched twill, as in the textile, and not as "bar" domains as in the reference, but is nonetheless consistent with the same in-plane (up-down) domain alignment. The different descriptor is because the optical microscopy technique in the reference lacked the spatial resolution and surface sensitivity to see the detail in the areas so near to the variant interface and the fine structure could not be determined. The surface structure of the domains changes across the twin as the easy axis of magnetization goes from in-plane to out-of-plane as a function of position and crystal structure.

Upon cooling (Figure 3.7), exclusively the banded Region I expands at the expense of maze-like Region II, and it can be deduced that there must be a symmetrically compatible habit plane between the two coexisting variants, allowing the plane to be mobile with the driving force of temperature. Re-heating to an intermediate temperature shows a hysteresis in the regrowth of Region II by motion of the same wall (Figure 3.8), consistent with both a large structural deformation and thermal hysteresis. XMCD spectra (not shown) are taken on BL4.0.2 at all temperatures and indicate a strong magnetic signal at 706.4 eV with the presence of an oxide peak separated by 1.4 eV that decreases in relative intensity with increasing temperature from 100 K to ambient.

The region of interest for the heating transition is outlined in the lowest panel of Figure 3.7 and several frames of the thermal evolution of this region are arranged in Figure 3.9. Images were taken approximately every 5 K upon reheating and a magnetic plane feature with no associated topographic contrast was observed to nucleate in the bunched-twill morphology of Region III and travel

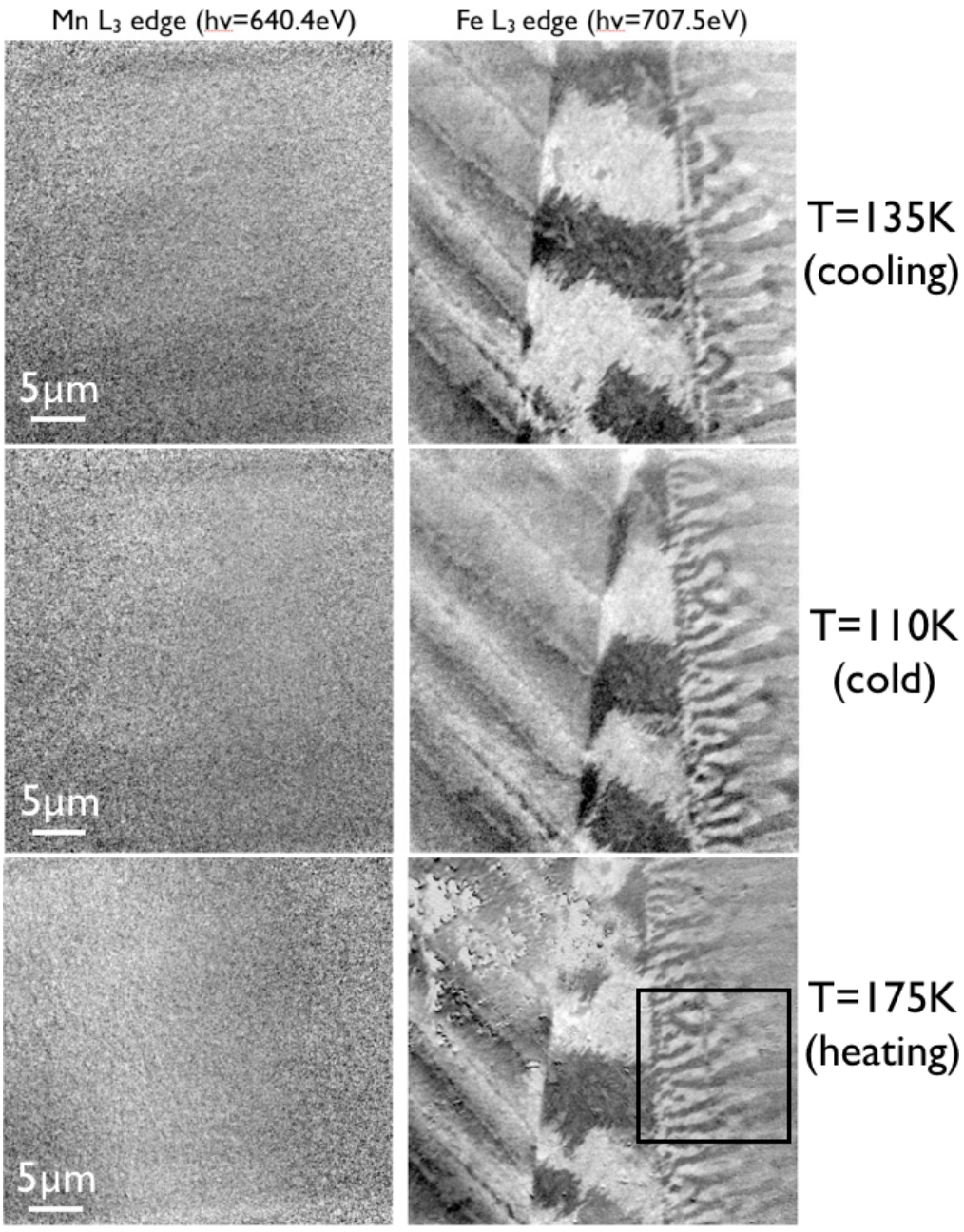

Figure 3.7: Manganese (left) and iron (right) L_3-edge contrast images from T=135 (top) and T=110 K (middle) with cooling, and then 175 K upon reheating. Mn contributes zero net magnetization visible in the surface sensitive technique and all the contrast appears in the iron. Note that the area of Region II decreases significantly but unevenly, only to the favor of Region I. The boundary between Regions II and III is immobile. The region of interest where the destructive magnetic feature appears will be in the marked square. FOV 36 μm.

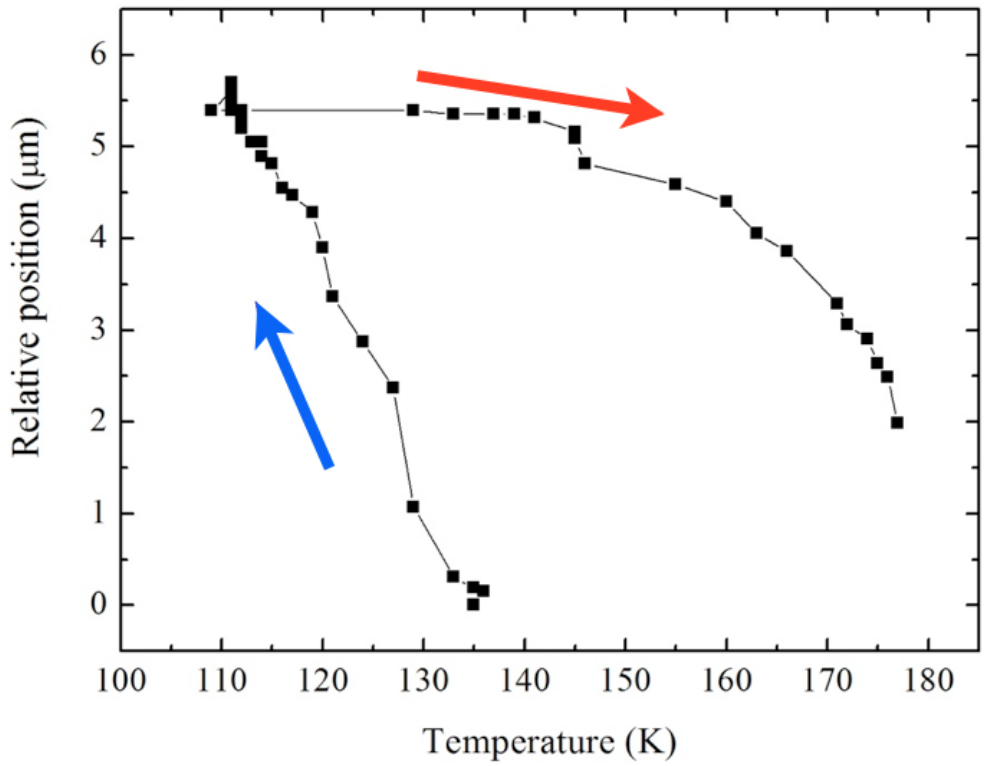

Figure 3.8: Average position of the mobile domain wall between Regions I and II with cooling (blue arrow) and then heating (red arrow). The thermal hysteresis is as large as expected from the bulk averaged data.

toward the heretofore immobile boundary between Regions II and III. The result of this is a doubling the line frequency of the affected magnetic domains and, after further heating, leaving Region III in a "wrinkled" state as in the right panel of Figure 3.10. This surface-specific branching is associated with a reduction in magnetostatic energy and could be consistent with the formalism for an adaptive martensite outlined for a pinned, twinned microstructure near a rigid interface [96]. In the original publication the rigid interface was an epitaxial substrate but here it is an immobile habit plane, indicating that the presence of the surface changes the nature of the boundary between the martensitic variants. The mobile wall between Regions I and II is symmetrically inequivalent to the immobile wall between Regions II and III. No further evolution between 231 K and ambient was observed.

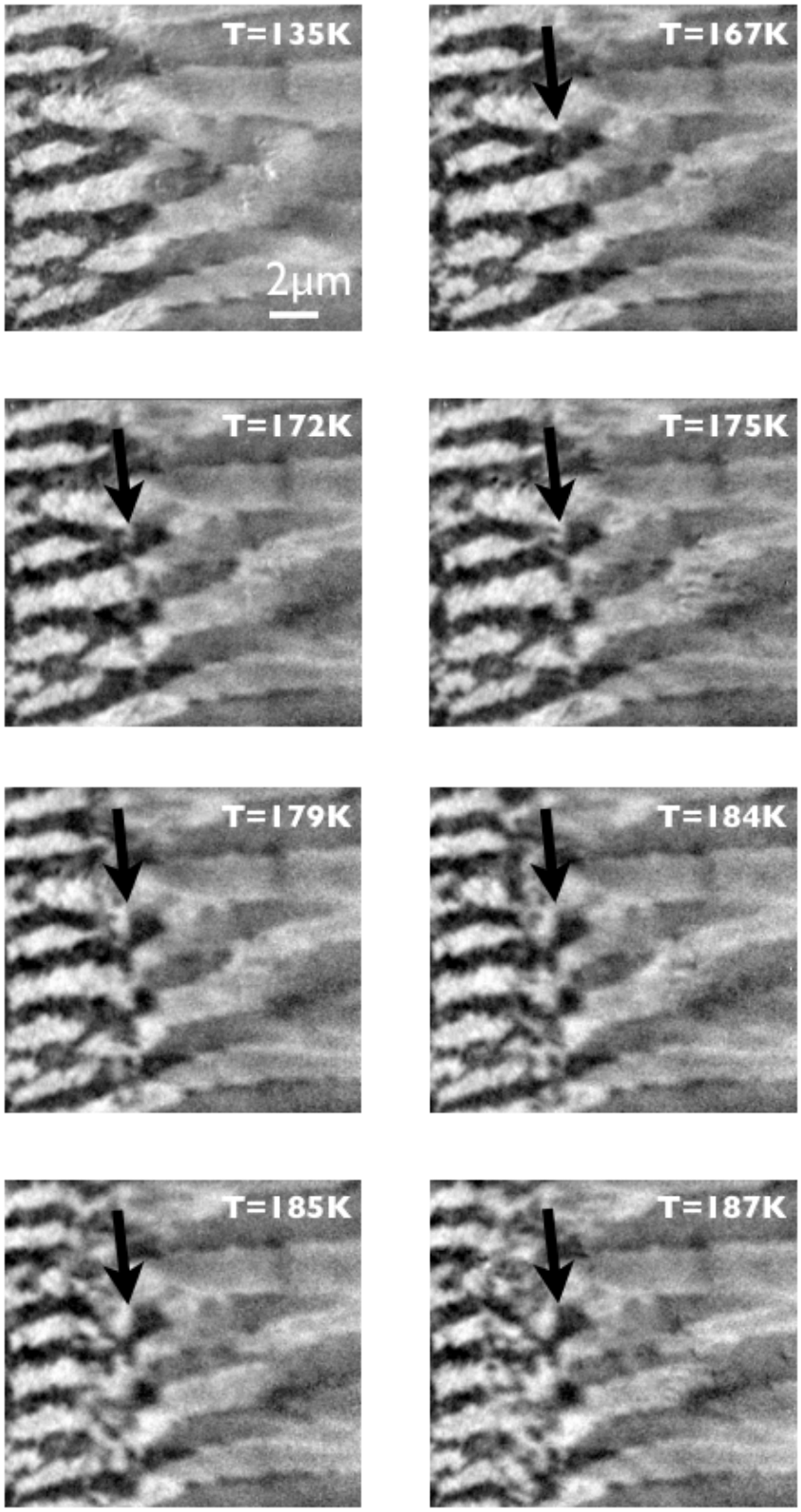

Figure 3.9: Evolution of adaptive martensite with heating. The original formalism was a martensite in contact with an epitaxial substrate but here the rigid boundary condition is a pinned twin boundary.

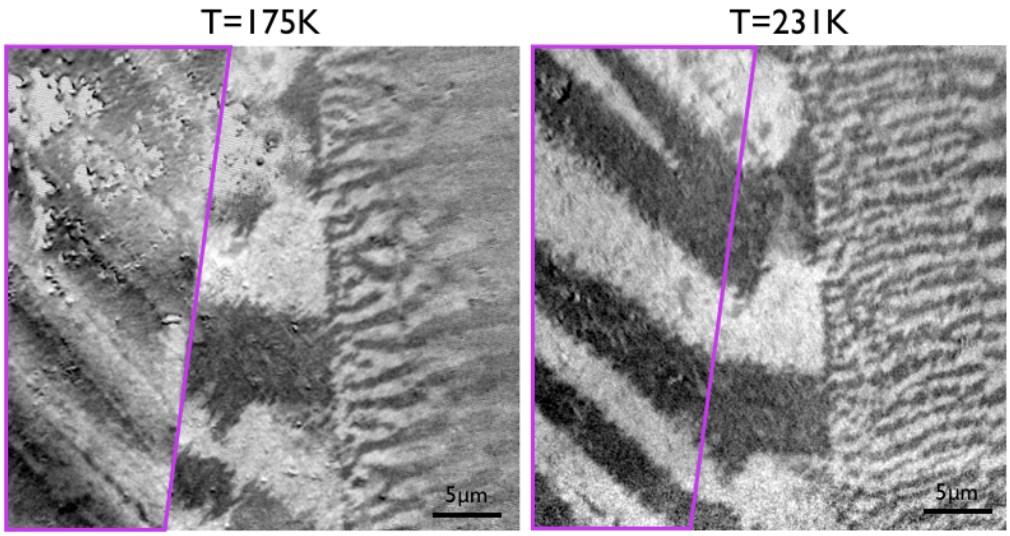

Figure 3.10: Two phenomena are occurring simultaneously here. Region I is transforming from band domains to maze domains in a simple, first order transformation. Additionally, Region III is undergoing line frequency doubling (branching) as a result of minimizing the magnetostatic energy. This branching is specific only to the surface and is not reflected in the volume. Grainy areas near the upper left of the image at intermediate temperature indicate overexposure on the detector.

Figure 3.11 is coarsely stitched example from near to the original images of a more complex intersection of magnetic and structural domains. Future investigations can be optimized to extract local spectra from each domain with a spatial resolution down to 20 nm and to assign the martensitic descriptors with more detail and confidence.

Using the custom-built piezo-actuated flexure joint from Figure 2.6, the crystal was strained *in situ* at +5 V and +60 V, for a total nominal deflection of 36 μm. Given pessimistic loss estimates of 50%, crystal orientation of [010] as the direction along which the compressive force is projected, starting dimensions of 2mm x 3mm x 11mm, and elasticity in the flexure joint this should amount to at minimum 1% strain. Small domains were visible as expected but no convincing evolution of the magnetic contrast was observed. In order to document the attempt, the decomposition of the "zipper" domains with piezoelectrical actuation in the homebuilt rig is most evident in the upper-right arm of the outlined area in

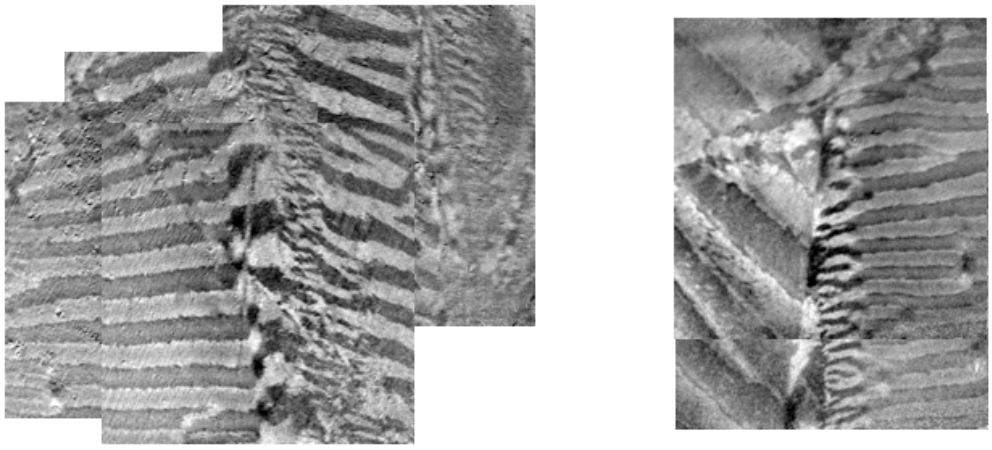

Figure 3.11: A coarsely stitched nearby example of a more complex intersection of magnetic and structural domains. Future investigations can be optimized to extract local spectra from each type of domain with a spatial resolution down to 20 nm.

Figure 3.12 and suggests some degree of strain-induced magnetic evolution. Small but visible magnetic domains are boxed in the upper panels and rotated for visual clarity in the middle panels. The static markers are circled in red. A schematic of what is being shown is illustrated in the lower panels. The domain oriented as at left can show a magnetic contrast in response to the possible polarizations of incident light available in the given crystal orientation. The domain at right has no projection of the magnetization along the photon propagation vector, and thus can have no magnetic contrast. The domain at right is oriented to be energetically favorable to the application of an external stress from the piezo actuator.

In conclusion, the evolution of the magnetic domain structure in single crystals of novel Heusler shape memory compound near the Fe_2MnGa stoichiometry was observed for the first time by high-resolution photoelectron emission microscopy in response to both temperature and strain and correlated with averaged magnetic spectroscopy measurements. A magnetic feature consistent with an adaptive martensite phase is also observed to nucleate and grow in one martensitic variant.

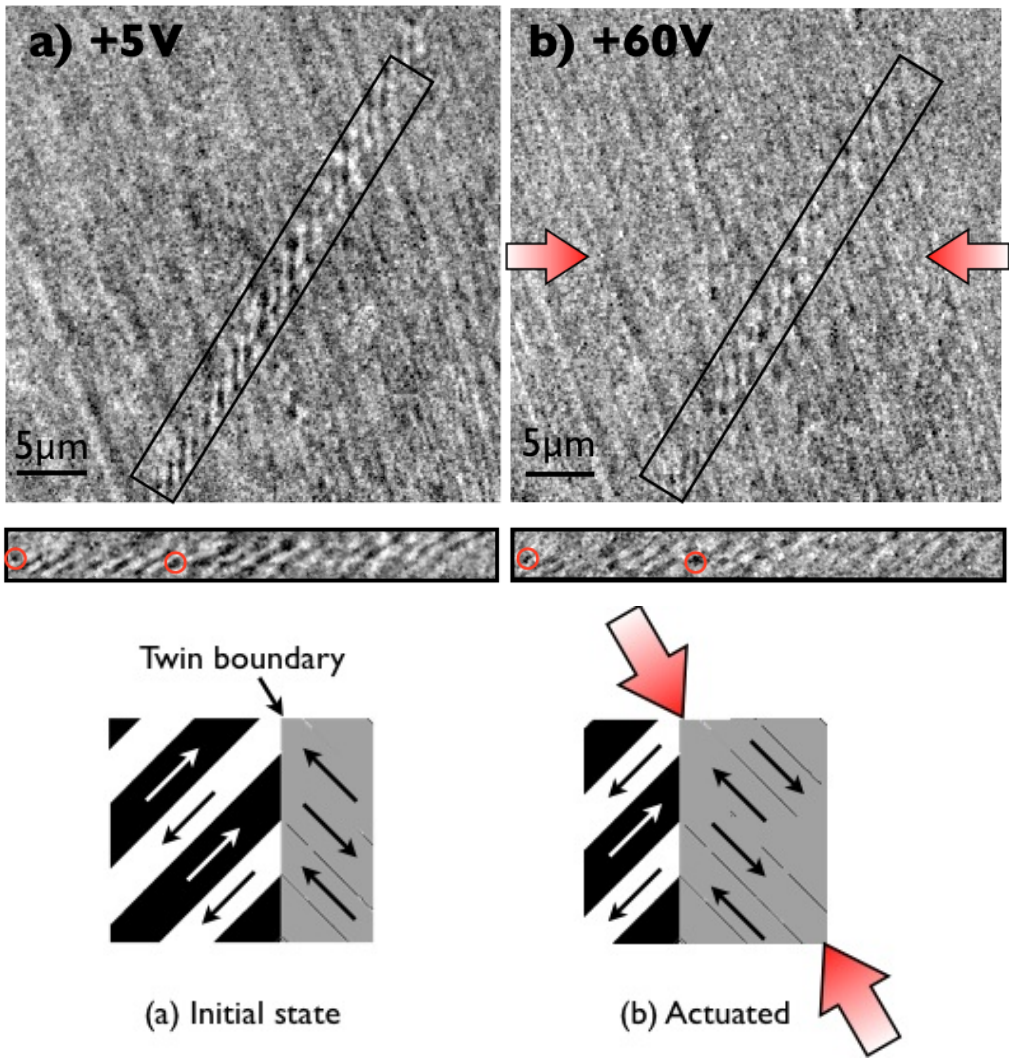

Figure 3.12: Using the custom-built piezo-actuated flexure joint from Figure 2.6, the crystal was strained *in situ* at +5 V and +60 V, for a total nominal strain of 1%. The boxed areas in the upper panels are rotated for visual clarity in the middle panels and the static markers are circled in red. A schematic of what is being shown is illustrated in the lower panels. The domain oriented as at left can show a magnetic contrast in response to the possible polarizations of incident light available in the given crystal orientation. The domain at right has no projection of the magnetization along the photon propagation vector, and thus can have no magnetic contrast. The domain at right is oriented to be energetically favorable to the application of an external stress from the piezo actuator.

Chapter 4

Mn_2YGa (Y=Fe, Co, Ni)

Heusler compounds Mn_2YZ are described in detail in Section 1.1. For the purposes of this chapter it is only important to recall that because of the high Mn content they are often tetragonally deformed, partially or completely half metallic (HM), and ferrimagnetic. Manganese compounds are of particular interest because hybridization is not only possible Mn-Mn but also Mn-TM with a transition metal neighbor.

Polycrystalline ingots in the composition series $Mn_{2+x}Fe_{1-x}Ga$ (Section 4.1) and $Mn_{2+x}Co_{1-x}Ga$ (Section 4.2) are explored by structural and magnetic spectroscopy, and doped compounds near Mn_2NiGa (Section 4.3) are probed as a candidate material for magnetocaloric applications. Ru and Rh are the isovalent analogs of Fe and Co, respectively, and compounds containing them are important for testing predictions about the interrelated effects of atomic radius and unoccupied electronic orbitals. With this in mind, spectroscopic data from powders of Mn_2RuGa were gathered because of a demonstrated point of magnetic compensation at 225 K. The samples were not further investigated after a reliable absorption signal and magnetic dichroism proved elusive because of convolution of the absorption from the ruthenium coating on the ultra-low-emission glass and silicon beamline optics.

4.1 $Mn_{3-x}Fe_xGa$

Half-metallic behavior in tetragonally distorted compounds based on Mn_2FeZ have been theoretically predicted [48] but the relevance to MSM or spin torque transfer applications was not considered. HM and MSM effects are both controlled by a symmetry-lowering magnetostructural transition that is strongly dependent on spin alignment and magnitude of the individual magnetic sublattices as mediated by the nonmagnetic (main group) intermediaries and the stress/strain history of the particular sample. Recent DFT calculations [48] suggest that the magnitude of the magnetic moments on these sublattices are strongly influenced by the size of the unit cell and that the magnetic properties arise out of a fine balance or competition among them.

Powder diffraction and laboratory-based magnetometry of the $Mn_{3-x}Fe_xGa$ series shows hard magnetic behavior and high Curie temperatures (700 K) in agreement with *ab initio* calculation, but the experimental spin polarization is found to be reduced from an ideal 100% to closer to 70%. In this rich phase space, HM is most commonly due to an asymmetry in the effective mass of the majority and minority electrons and not purely due to an energy gap in one spin band, so both majority and minority bands are metallic in all compositions but the spin-up channel is close centered near a pseudogap. Decreasing the iron content from stoichiometric end compound Mn_2FeGa is observed to decrease the c/a tetragonal distortion from almost 2 to only 1.8 for all temperatures up to about 623 K, whereupon it transforms reversibly to a hexagonal phase. Mere unit cell tetragonality is known to be a necessary but not sufficient condition for obtaining the highly desirable perpendicular anisotropy in magnetic films that would allow industrial application in spin torque transfer systems. With decreasing iron, the c/a ratio and the net saturation magnetization can be engineered to increase. This is due to the higher electronegativity of $3d$ Fe atoms occupying the tetrahedral position. In contrast, only induced moments can be found in tetragonal magnetic

compounds with heavier $4d$ elements such as Ru and Rh [97].

Arc melted ingots were mounted in the apparatus described in Figure 2.4 with a set screw, and electrical conductivity for signal transmission was ensured with a droplet of silver paint at the point of contact. Breaking pressure was better than 5x10^{-8} Torr and photon flux was maximized by using the 600 lines/mm region of the monochromator grating. XMCD parameters were negative helicity photons and 1 T field at 1 Hz switching frequency with 1 sec delay after switching to allow the eddy currents to decay and the sample holder to stabilize. Oxygen absorption spectra were taken after every XMCD scan to monitor the oxidation of the compound.

Figure 4.1 shows a compilation of all XAS and XMCD spectra of manganese (left) and iron (right) in the series of polycrystalline $Mn_{3-x}Fe_xGa$. All XAS spectra can be normalized and many of the difference spectra show clear magnetic moments, particularly in the ferromagnetic iron. Correcting for incomplete (65% on BL6.3.1) circular polarization, absolute spin and orbital moments can be computed from a slight rearrangement of the equations in Section 2.2.3 as

$$\frac{m_{orb}}{m_{spin}} = \frac{2}{3}\frac{(A+B)}{(A-2B)}$$

where A and B are, as before, the areas of the L_3 and L_2 peaks in the difference signal.

The trend in the net manganese moments is shown in Figure 4.2 to decrease with decreasing manganese content. For comparison, consider the results of self-consistent *ab initio* calculations using the spin-polarized fully-relativistic Korringa-Kohn-Rostoker method, where the total contribution to the moment from each Wyckoff site gives +2.4 or -3.1 μ_B, depending on site occupancy. Tetrahedral manganese atoms are calculated to show the highest magnitude site-specific magnetic moment and to be the most resistant to deterioration by iron substitution, showing only a slight decrease with increased iron content. The moment of octahe-

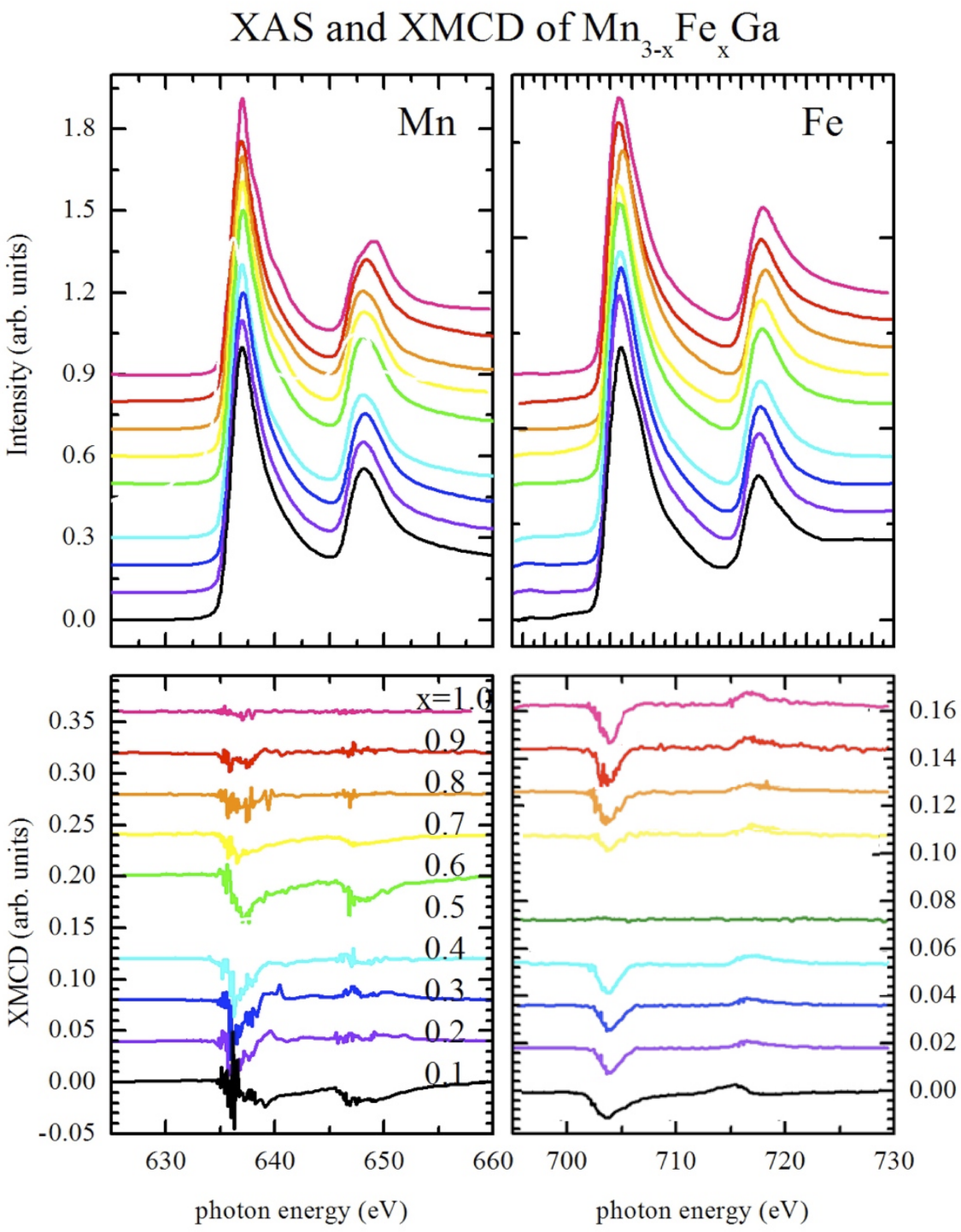

Figure 4.1: XAS and XMCD of manganese (left) and iron (right) in the series of polycrystalline $Mn_{3-x}Fe_xGa$. All XAS spectra can be normalized and many of the difference spectra show clear magnetic moments, particularly in the ferromagnetic iron. In all panels the top scan is Mn_2FeGa, decreasing iron contribution progressively towards the lowest compound $Mn_{2.9}Fe_{0.1}Ga$.

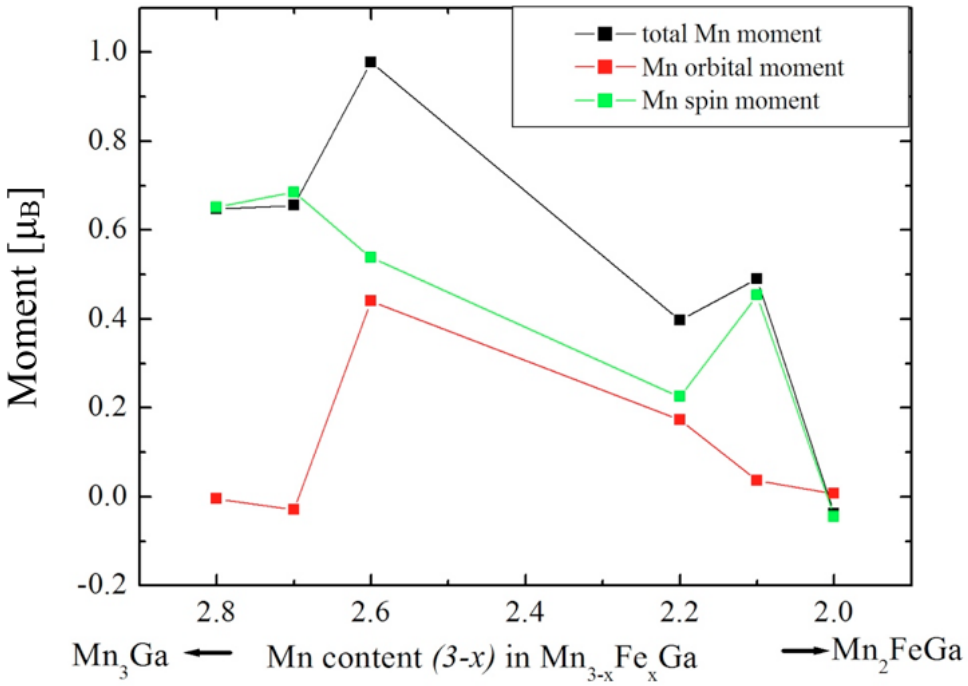

Figure 4.2: A trend of decreasing moment with decreasing manganese is observed, in contrast to *ab initio* calculations of the summed moments but absolutely consistent with both previous spectroscopic measurements and the intuition that manganese in the end compound of Mn_2FeGa interacts with itself so as to compensate nearest neighbors. The *net* moment, therefore, detectable by XMCD, is then very small.

dral manganese atoms is calculated to increase very slightly with increasing iron. Therefore, the reduction in net manganese moment per formula unit (the quantity detected by XMCD) to zero at the Heusler composition Mn_2FeGa means that the relative site occupancy is 43.6% tetrahedral (-3.1 μ_B) and 56.4% octahedral (+2.4 μ_B).

Iron interacts with other iron atoms positively and it can be seen in Figure 4.3 that with more iron, the spin moment increases approximately linearly in accordance with Slater-Pauling. The orbital moment in all instances of the $Mn_{3-x}Fe_xGa$ series is very small, consistent with a large tetragonal distortion leading to a large average separation of iron atoms. The trend of the iron moments and the small absolute values is also consistent with a small exchange splitting as in Ref. [48], and consistent with *ab initio* calculations where the total magnetic moment per

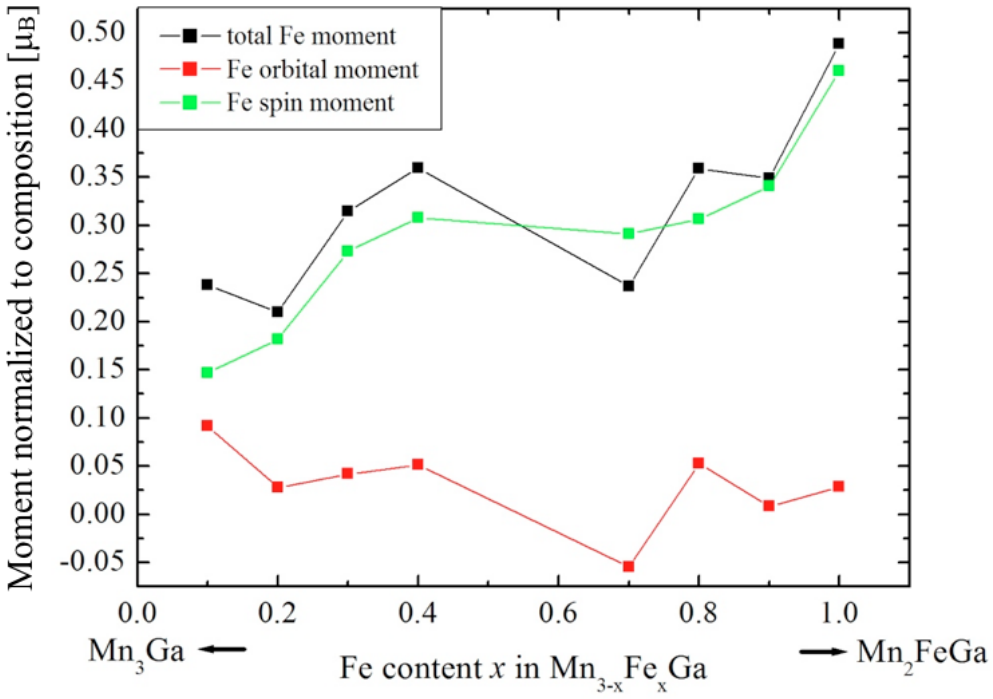

Figure 4.3: Iron interacts with other iron atoms positively so it can be seen the spin moment increases approximately linearly with increasing iron. The orbital moment in all instances of the $Mn_{3-x}Fe_xGa$ series is very small, consistent with a large tetragonal distortion leading to a large average separation of iron atoms. The trend of the iron moments and the small absolute values is also consistent with a small exchange splitting.

iron atom should be fairly constant at 1.7 μ_B. Thus with increasing iron content the iron contribution to the moment should increase.

The total magnetic moment per formula unit inferred from XMCD and weighted by the content goes almost linearly from 0.86 μ_B in $Mn_{2.9}Fe_{0.1}Ga$ to 0.49 μ_B in $Mn_{2.0}Fe_{1.0}Ga$, decreasing from $x = 0.1$ to $x = 1.0$. Electronic structure calculations optimized using the Wien2K program indicate that the total magnetic moment should decrease linearly from a maximum of 1.4 μ_B per formula unit at the end compound Mn_3Ga to a minimum of about 0.8 μ_B at the opposing end compound of Mn_2FeGa. At all compositions the experimentally derived net magnetic moment is smaller than calculated because of the antiferromagnetic coupling within the manganese.

4.2 $Mn_{3-x}Co_xGa$

Heusler Mn_2CoGa was predicted as a half-metallic ferrimagnet (HMFi) [98], and cobalt as another elemental ferromagnet like iron is a logical substitution to explore the effects of independent and partially compensating magnetic sublattices in $Mn_{3-x}Co_xGa$, in analogy to the previous section[1]. HM in cubic Heusler compounds is well established theoretically [12] and experimentally [99, 100] with a very small moment located at the Y position in X_2YZ compounds: here, Y=Co. Ferrimagnets with large local moments and half-metallic properties are predicted for cubic Heuslers including Mn_2YGa where separate populations of Mn occupy distinct tetrahedral and octahedral coordinations. Stoichiometric Mn_2CoGa in particular is an element of the series Z=Al, Ga, In, which has the unusual property of going down the rows of the *sp* element the total moment goes *up* but the Curie temperature goes *down* [101]. Another fact to consider for Mn_2CoGa as opposed to, for example, Mn_2CoGe is that HM in Mn_2CoGa is weak, with the Fermi energy lying at the minimum of a pseudogap in the majority and a true gap for the minority electrons: even though the "only" conduction electrons are of majority spin, the population is still small. In contrast, the extra valence electron in Mn_2CoGe contributes strongly to the majority spin band at E_F and the half metallicity is much more robust [98]. By extension, the damping properties are also more robust in the germanium compound.

Heusler Mn_2CoGa has a lattice parameter $a = 5.86$ Å and experimental T_C=718 K (calculated to be 886 K) and has an expected moment per formula unit of 2 μ_B. In the composition series of $Mn_{3-x}Co_xGa$ the Co atom on the B site is successively substituted by Mn as x goes from 0 to 1, thus tuning the net magnetization. The partial replacement by Mn also replaces Co on the B sites and degrades the half-metallicity effectively. The end compound Mn_3Ga has

[1]This section is being submitted to *Applied Physics Letters* as *"Disentangling the Mn moments on different sublattices in the half-metallic ferrimagnet $Mn_{3-x}Co_xGa$"* by P. Klaer, C.A. Jenkins, V.Alijani, J. Winterlik, B. Balke, C. Felser, and H.J. Elmers

been extensively investigated [52, 53] and it is known that the fully-compensated half-metallic ferrimagnetic cubic structure cannot be produced, and instead the tetragonal DO_{22} phase leads to a magnetization of roughly 1 μ_B per formula unit combined with a reduced spin polarization. An analysis of the Mn XMCD spectra will reveal the antiparallel alignment of the itinerant magnetic moment on the A site and the localized moment on the B site. A slight increase in magnetic moment on the manganese is also to be expected relative to the $Mn_{3-x}Fe_xGa$ series because of the slightly increased lattice parameter.

Ingots similar to those in Section 4.1 were broken under UHV with base pressure better than 8x10^{-9} Torr. The L absorption edges of cobalt are at higher energy than for iron so the photon flux for all scans was optimized using the 1200 lines/mm section of the BL6.3.1 grating monochromator for measurements at the ALS. Other data was taken at the UE56/1-SGM beamline at BESSY, the synchrotron in Berlin, Germany. Unfortunately the 200 eV change in energy between Mn and Co L-edges resulted in a slight change of spot position, which was neglected because despite surface roughness on the broken surface, the polycrystalline ingots should have a grain size small enough that the 500 μm beam diameter integrates good statistics.

X-ray diffraction shows that for compounds with x >0.5 a cubic unit cell is favored but that a tetragonal distortion occurs for $x \leq 0.5$, or compounds rich in manganese. This is in contrast to the $Mn_{3-x}Fe_xGa$ series where all compositions $1 \geq x \geq 0$ are tetragonally distorted. For the Heusler stoichiometry Mn_2CoGa the cubic $CuHg_2Ti$-type structure and site occupation was confirmed, but the similar scattering factors for the $3d$ transition elements prevents us from a confirmation of the structure for all values of x with a conventional diffractometer.

Element-specific spin and orbital magnetic moments were determined from XAS/XMCD spectra using sum rules (Figure 4.4). The total magnetization of the cubic compounds here obeys the generalized Slater-Pauling rule and decreases linearly with decreasing x at $2x$ Bohr magnetons per formula unit. The structural

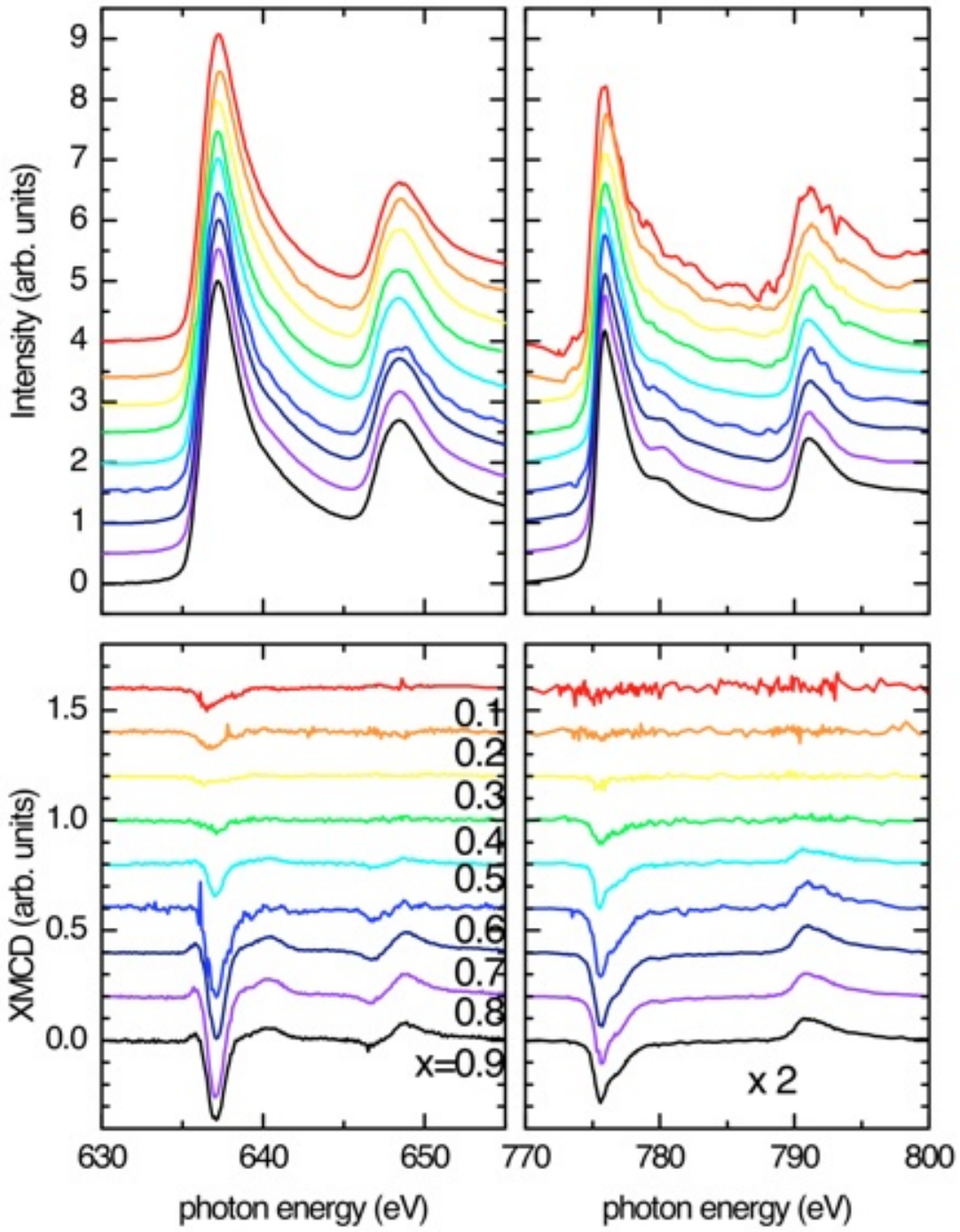

Figure 4.4: XAS and XMCD of manganese (left) and cobalt (right) in the series of polycrystalline $Mn_{3-x}Co_xGa$. All XAS spectra can be normalized and many of the difference spectra show clear magnetic moments. In all panels the top scan is Mn_2CoGa, decreasing cobalt contribution progressively towards the lowest compound $Mn_{2.9}Co_{0.1}Ga$.

change from cubic to tetragonal with increasing Mn content changes the magnetic hysteresis (not shown) abruptly from soft to hard. In contrast, the deviation of the net magnetization from the Slater-Pauling behavior is less sudden and shows up only for very low Co content as shown in Figure 4.5. For $x > 0.5$ we find a good agreement between the total magnetization determined by magnetometry and by sum rules, while spectral analysis gives smaller values for lower Co concentrations. We assume that this is caused by the limited external field and that the samples are not fully saturated. Element-specific values shown in Figure 4.5 were normalized to match the measured magnetization in saturation.

The Co moment increases with concentration for a maximum at $x = 0.3$ and assumes a nearly constant value of 1 μ_B per atom for larger concentrations. In contrast the Mn moment shows a small constant value up to $x = 0.5$, and in the higher Mn-content range the moment increases linearly with x as expected for the half-metallic phase. The decreasing Mn moment for the highest Co concentrations might indicate an increased disorder with Mn-Co antisite defects which would impede the expression of half-metallic properties. The dependence of the spin moments on the Co concentrations identifies the region of lowest Mn content (most strongly cubic and nearest to the Heusler stoichiometry $2 : 1 : 1$) as most promising for a high spin polarization at the Fermi level, although we recall from the density of states calculations that the majority band sits in the valley of a pseudogap and that the "full" spin-polarization is not robust.

Interestingly, the orbital magnetic moments of Mn and Co show an opposite behavior with increasing Co: For small Co, the orbital moment nearly vanishes while the Mn has a fairly large value. For large Co, the Mn orbital moment approaches zero and the Co orbital moment increases. The change in orbital to spin moment ratio for the summed moments with respect to the composition shows a strong decrease from the tetragonal phase to the cubic phase, which is related to the symmetry increase in the cubic phase.

Mn moments on inequivalent sites derived from a fit to reference spectra

are compared to theoretical predictions. Mn XMCD confirms the ferrimagnetic character with two symmetrically inequivalent Mn sublattices with antiparallel spin orientation and different degrees of spin localization. In order to prove the predicted ferrimagnetism in highly ordered cubic compounds we analyzed the XAS/XMCD spectra for the $Mn_{2.2}Co_{0.8}Ga$ composition by comparison with reference spectra from Heusler alloys where Mn occupies a single sublattice as shown in Figure 4.6. Co_2MnSi is seen as the prototype half-metallic Heusler alloy with a localized Mn moment on the B site. The localization of the Mn *d*-bands in this compound causes multiplet features in the XAS/XMCD spectra that can be well simulated by an atomic model. In contrast, the magnetization in Mn_2VAl originates from itinerant Mn states occupying A and C sublattices. Mn_2VAl is an ideal comparison material because it has the highest T_C for a manganese-based Heusler compound. The linear combination with equal weight of the Mn spectra from Co_2MnSi and Mn_2VAl fits the Mn XAS spectra for the chosen compound as shown in Figure 4.6. Prominent features of the Co_2MnSi spectrum, namely the L_3 shoulder and the small branching ratio is cut in half, indicating the equal occupation of both sites. The small nominal deviation (1.2:1) from equal occupation cannot be resolved by the fit. The XMCD spectra can also be fitted by a linear combination of reference spectra. In particular the positive L_3 pre-edge peak is indicative of the presence of antiparallel Mn moments. The deviation at the L_2 pre-edge likely originated from a shift of the Mn multiplet feature caused by the difference crystal field parameters.

Using the values for the averaged Mn moment (μ_{spin} =0.4μ_B, μ_{orb} =0.01μ_B) per atom and for the ratio of the Mn moment on the A and the B sites ($\mu_{spin}(B)/\mu_{spin}(A)$ =-3.9) and ($\mu_{orb}(B)/\mu_{orb}(A)$ =-1.9) determined from the fit of the reference spectra, individual Mn moments results: $\mu_{spin}(A)$ =-0.33μ_B, $\mu_{spin}(B)$ =+1.3μ_B, $\mu_{orb}(A)$ =-0.03μ_B, $\mu_{orb}(B)$ =+0.05μ_B. Similar ratios of magnetic moments are observed for neighboring Co concentrations. The Mn moments are much smaller than values calculated by early *ab initio* theory [102], but only slightly smaller than more recent calcu-

lations [101] that showed deficiencies in the original work in overestimating the manganese moment by up to 0.7 μ_B per atom. Nevertheless the remaining discrepancy may indicate a residual antisite disorder that can be sensitively detected by XMCD. For smaller Co concentrations the Mn moment on the A site vanishes completely, indicating a strong deviation from the $CuHg_2Ti$ structure.

In summary, we have demonstrated the preparation of ferrimagnetic $Mn_{2+x}Co_{1-x}Ga$ compounds with a cubic structure for high Co content. Disentangling contributions of Mn atoms on different sublattices reveals fairly large antiparallel oriented Mn moments although the average magnetization is quite small. Hence, this series is a potential candidate for the preparation of highly efficient spin torque devices given that the atomic order can be increased.

4.3 Mn_2NiGa

Thermoelastic and magnetocaloric properties often coexist because both depend on symmetry-lowering magnetostructural transitions [29]. In the case of MSM this can be most directly considered to be because of the point groups involved in the martensitic transition but in the case of giant MCE a change in entropy of any origin is required to make the adiabatic demagnetization that is the driving force of magnetic refrigeration an efficient and economical process, and a phase change is convenient and reversible. An electronic change associated with minority X states accompanies the magnetostructural transition so a fingerprint for MCE could also be developed by absorption or magnetic spectroscopy.

Since Ni_2MnGa is a known MCE benchmark [33] and Mn_2NiGa has been shown to have a high Curie temperature of 585 K and to exhibit MSM in both thin film and bulk [22, 93], it was a ready candidate for evaluation. Single crystals were grown at Southern Illinois University and characterized by XRD and VSM. For application purposes it is advantageous to have a Curie temperature around room temperature so slight compositional tailoring is required from the ideal 2:1:1 com-

pound. Unfortunately, no significant anomaly in the heating curves was observed near the structural transition temperature, so MCE was not measured directly. Figure 4.7 displays the M vs. T curves for various levels of iron doping in a parent compound of Mn_2NiGa, sadly lacking any anomaly indicative of a large entropy change.

In conclusion, the combination of these studies of Mn_2YGa leads us to determine that a study of the effects of unit cell volume and symmetry on MSM, HM, and MCE is in order, where a search for a unifying descriptor of lattice parameter, transformation symmetry, and the alignment of magnetic sublattices is explored with respect to calculations.

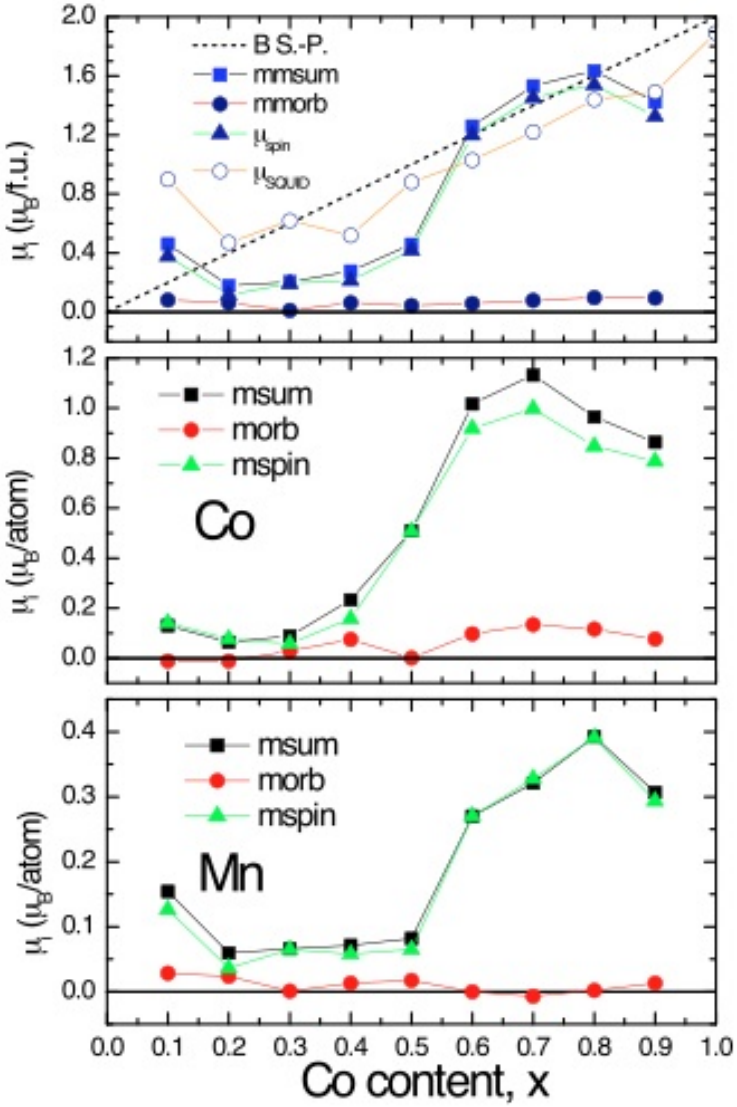

Figure 4.5: Two regimes are visible in the element-specific magnetic moments. Near the Heusler composition Mn_2CoGa the compound is cubic and the moments obey the Slater-Pauling prediction. At lower cobalt concentrations the compound is strongly tetragonally distorted and can be considered Mn_3Ga with iron defects.

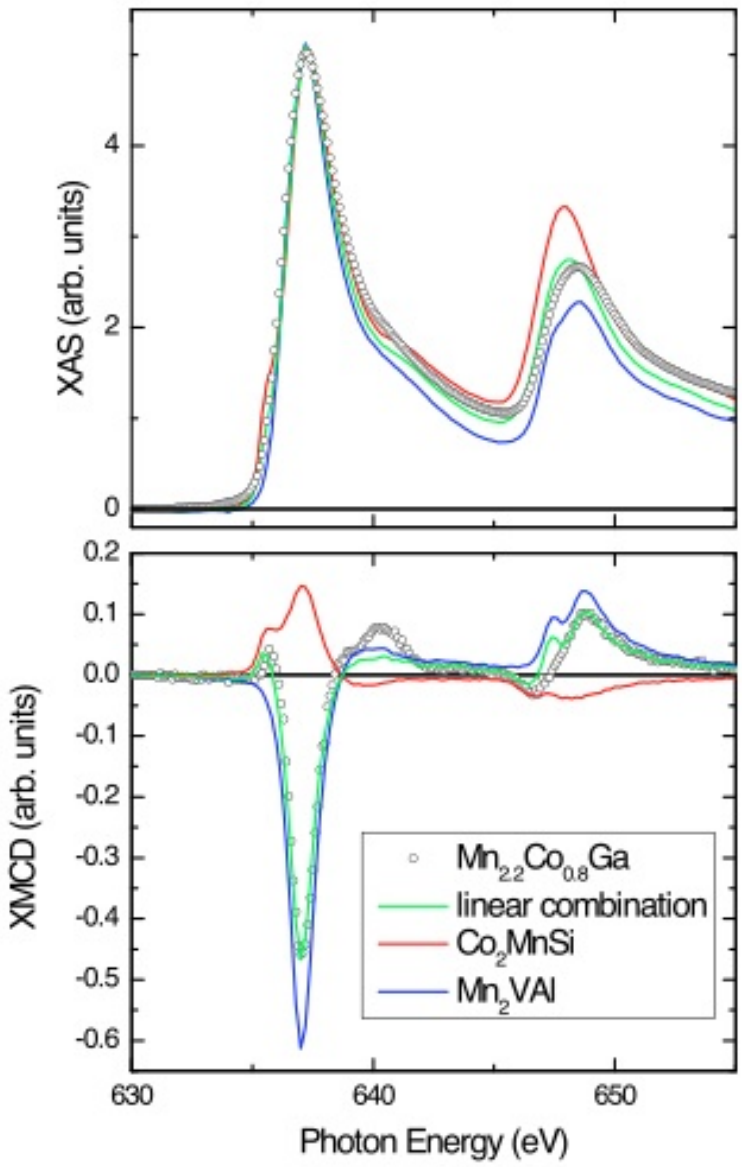

Figure 4.6: The XA of $Mn_{2.2}Co_{0.8}Ga$ fits well to a linear combination of the manganese spectra determined from prototypical Heusler compounds Co_2MnSi and Mn_2VAl, showing the partial site occupancy of both tetrahedral and octahedral manganese. Plot prepared by H.J. Elmers.

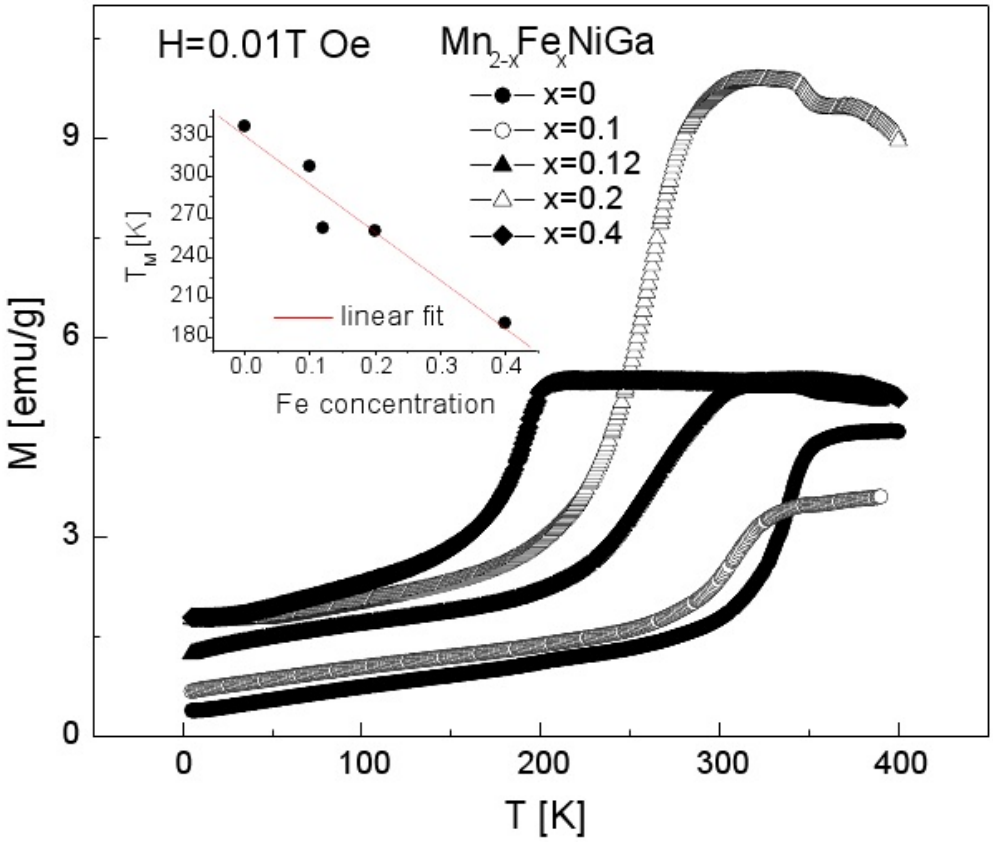

Figure 4.7: Magnetization vs temperature curves for various Fe dopings of Mn_2NiGa in search of an anomaly at the martensitic transition temperature that might indicate a large change in entropy associated with the magnetocaloric effect. No such anomaly was observed. Courtesy A. Pathak (Southern Illinois University).

Chapter 5

Conclusions

The '*Drosophila*' of magnetic spectroscopy and condensed matter magnetism are elemental iron for ferromagnetism and nickel oxide (NiO) for antiferromagnetism, but a strong case can be made for Ni_2MnGa and its daughter compounds to join the canon of functional material model systems for energy and multiferroic applications.

5.1 Summary

The structure of and phenomena in functional materials were introduced and explored in the context of several materials with a special emphasis on applications such as spintronics and energy. The concepts and capabilities of the advanced synchrotron characterization techniques used in this work were explored. In terms of physical results, sputtered films of half-metallic Mn_3Ga and Mn_3Ge, and others grown by molecular beam epitaxy, were fabricated for spin-torque transfer or perpendicular magnetic anisotropy applications for a reduced critical current. Out of plane anisotropy was indeed observed in MBE films of Mn_3Ga, promising future results in industry.

Melt-spun ribbons and single crystals of Ni_2MnGa were investigated to clarify outstanding questions raised by neutron diffraction and Ga K-edge spectroscopy

on Beamline 4.0.2 of the Advanced Light Source. Magnetic spectroscopy of thin films of Co_2MnGe determined the presence and quantitative value of the induced magnetic moment on Ge. A single crystal of Fe_2MnGa was obtained and the magnetic domains were explored by temperature- and strain-dependent photoelectron emission microscopy on Beamline 11.0.1. Anomalous destructive magnetic features are observed that are consistent with an adaptive martensite phase, and decomposition of magnetic domains correlated with piezoelectrically actuated compression is suggested.

Polycrystalline Mn_2YGa ($Y = Fe, Co, Ni$) ingots were obtained and characterized by magnetic spectroscopy at Beamline 6.3.1. The series $Mn_{3-x}Fe_xGa$ was shown to be tetragonally distorted over the range of $1 \geq x \geq 0$ and to approximately follow Slater-Pauling predictions for the magnetic moment. The magnetic structure of the manganese in $Mn_{3-x}Co_xGa$ was shown to be a linear combination of Mn spectra from Co_2MnSi and Mn_2VAl, indicating partial occupancy of tetrahedral and octahedral sites. No MCE was successfully measured in thermoelastic Mn_2NiGa despite the strong promise of the high-entropy, large-deformation phase transition.

Two important apparatus were designed and built in the course of this thesis, one for vacuum cleaving of polycrystalline ingots and another for the *in situ* piezoelectric actuation of shape memory single crystals in a photoemission microscope.

5.2 Outlook

Spectroscopic investigations are in progress to further the understanding of induced interfacial magnetism in ceramic perovskites. Prior to XMCD measurements, orthogonal double wedge samples of $0-300$ nm $La_{1-x}Sr_xMnO_3$ and $0-3$ nm $Pb(Zr_{1-x}Ti_x)O_3$ have been grown by laser-MBE in National Chiao Tung University (Taiwan) and are being investigated optically at West Virginia University.

Immediately upcoming work on the Mn_2FeGa composition series includes strain-

dependent measurements of ring diffraction on a specially designed mechanical rig at SSRL BL11-3 in order to further clarify the related effects of unit cell volume on MSM and HM behavior. Calculations must be obtained about the stability of the possible martensitic variants and the character of the magnetostructural transition.

Ongoing work with Mn_2NiGa centers not only around static measurements of magnetic refrigeration but also time-resolved demagnetization dynamics are in discussion at the Stanford LINAC coherent light source (LCLS, an x-ray free electron laser) and ALS BL6.0. Proposals have already been submitted for single-shot time on the Diffraction and Projection Imaging beamline (DiProI) at FERMI, the Italian soft x-ray FEL, in a consortium with researchers from the ALS, KAIST (Korea), and University Nancy (France) in order to investigate the femtosecond dynamics of nanoscale magnetic phase transitions and relaxation channels in spintronic Heusler compounds, among others.

The overall goals of the next three years of research involve coupling compatible multiferroic layers to explore the effect of the multiple degrees of freedom. As an already known example, consider an MSM compound as an additional layer in an MTJ. At its most fundamental, an MTJ stack is a vertical heterostructure of ferromagnet / insulating tunnel barrier / ferromagnet. If a thin film of low-coercivity MSM material was included, a magnetic field applied externally could actuate new stress states in the MSM layer. This would transfer epitaxially to a strain in the electrode material, allowing new electronic states such as spin polarization. Known and well-described ternary intermetallics Ni_2MnGa and Co_2MnSi could function as the MSM and ferromagnetic electrode, respectively, with the additional advantage that their lattice parameters are already closely matched due to their Heusler crystal structure.

A second possibility integrates thermo- and piezoelectrics. A thermoelectric material can scavenge electricity from waste heat, while a piezoelectric material converts an input voltage into strain. Combining a thermoelectric and piezoelectric

material in a vertical thin film heterostructure will allow the design of a self-limiting device. In such a device the efficiency of the thermoelectric material could be adjusted through the strain state of the piezoelectric.

These goals can all be realized by two developments in the configuration of two ALS endstations. In the first case, the vector magnet on BL4.0.2 is being decommissioned during Winter 2011 and transferred to BL6.3.1. Additionally, funding and approved collaborators are being sought to facilitate in the commissioning of an *in situ* thin film deposition chamber on BL6.3.1, most probably for dc sputtering of ternary Heusler intermetallics. This would allow for the layer-by-layer monitoring of the anisotropies, magnetizations, and chemical and structural evolution in such complex heterostructures.

Appendices

Appendix A

Think tank for MAINZ

During the 2010 student spring retreat of the Graduate School of Excellence MAINZ, Erich Brandeau, Catherine Jenkins, and Chris Mills held a Think Tank workshop consisting of two sessions of three hours each with a formal group presentation the following day. The first three hours were an introductory talk with a one page Design Project intended to stimulate discussion about the students own research. All 50 students were required to attend. The three hour afternoon session was in parallel with a strategy session for the graduate school and students could choose which to attend, so 21 students participated in the product development group work, starting from a basic idea and taking it through to some finished deliverable, either a mock press release or a sketch of a business plan and a product description. Practical design projects including an egg catapult and an MIT D-LAB style water purification project were scrapped at the last minute against student resistance.

Evaluations were collected and one followup question I should have included was to have them rate the level of organization. For enjoyment and benefit questions, 7 is best, 4 is neutral, 1 is worst. For time allocation, a negative number means too little time was spent, zero means just right, and positive number means too much time, on a scale of -1 to +1. "Design project" means questions 1-7 to be done individually and concentrated on the students own doctoral work. By

research project, the group work, press release, and product development in questions 8-9 is meant.

	Overall	Intro	Design*	Research**	Group
Enjoyment	5.43	4.63	4.53	5.30	4.60
Benefit	5.05	4.21	3.89	4.53	3.65
Time	0.05	0.14	0.00	0.05	-0.25

Selected comments: **"Yes!"**

What skills or knowledge did you gain from the Think Tank during this retreat?

"Discuss more! Exchange thoughts." "It isnt hard to find interesting projects when working with a group" "The experience how open discussion can work" "Its more fun to work on your own project than on someone elses (professor)" "Very interesting and crazy ideas". "Projects were great, very stimulating!"

How relevant did you find the design project and the problem solving presented?

"We thought of a problem and solved it by discussions." "Good to be able to explain complicated ideas in easy words." "Think outside the box is good." "More examples of real think tank outcomes." "More info about practical things (how to get investors, etc)"

How relevant did you find the research/group project? Was the information and guidance provided helpful?

"Yes, especially the experience that we could do something like that." "Real fun! Maybe for future think tanks we should be forced to more think about topics really involved with MAINZ." "Very relevant. Discussion of the idea was good. More information on funding and planning expenses, income, etc is needed."

"Guidance was helpful when the group was stuck on an idea. Discussion was fruitful and it was a good socializing activity."

Are you interested in following up with activities related to business plan development or entrepreneurship?

"Yes in form of powerpoint presentation or seminar." "Good book would be interesting"

Which product developed in the Think Tank has the best chance of success?

JUnQ: "Easy to realize and important for scientists." EGGY: "It can go to every house."

How do you volunteer to help the Think Tank evolve?

"Invite speakers, organize seminars, weekly think tank session." "Give it a room and a schedule, promote participation among the scholars." "Meet again at evening seminars with glass of wine." "Have a weekly think tank." "Have a room for students to develop ideas/build stuff." "Think tank should not be a workshop but a common method."

DNA DRUG SENSOR

Is it possible to escape having just a little amount of drug in your blood? No. Not anymore. In 2010 the idea of a sensitive drug detection was developed in MPI-P, Mainz, Germany. This detector needs very small amount of blood. Then the detection is done directly by using an atomic force microscope (AFM) and altered DNA sample.

EGGY -- The Smart ingredient!

Once you have it, you'll never want to miss it again!

We present a new, innovative kitchen supply, inspired by a magnetic lab stirrer. It stirs soups, milk, water, etc while you do other preparation. It even stirs when the lid is closed (very good when preparing tomato sauce or in high-pressure pots). The 'Eggy' is easy to use, easy to clean, and dishwasher-safe. It can be reused and re-charged. Just put it in your pot and switch it on via a remote control. The technique uses innovative wireless power chargers. In contrast to magnetic lab stirrers it is electrically driven using a gyro-technique like in Segways and can therefore be used with all your existing pots and every oven you own. Try and enjoy our non-toxic, harmless, and heat-proven kitchen aid. Spice up your cooking style!

Journal of Unsolved Questions (JUnQ)

Science is not always about success. Very often hard and thorough work only leads to the conclusion that something doesn't work. Nevertheless this 'failed' research provides useful and valuable information for fellow scientists. Traditionally scientific progress is communicated in journals. However currently only successful research projects are published. The majority in attempts in research is not successful, though. Therefore a lot of information is not accessible for the scientific community. A young group of scientists has set out to change this. With their Journal of Unsolved Questions (JUnQ) they provide a means to gather unfinished research and open problems. JUnQ is a new platform to communicate data that will never be published in traditional journals.

"You can't imagine the gain the scientific community has from this new journal. We preserve so much knowledge that is just out there" says project manager Matthias Junk.

Science never fails. Sometimes you just need to dig through the JUnQ and pick out the hidden treasures.

Figure A.1: Students divided into three main groups with three proposed companies: a DNA drug sensor, "Eggy", and the Journal of Unsolved Questions. At the time of submission (January 2011), JUnQ has just published its first issue, available at http://junq.info.

The following is the text of the handout for the personal and small group exploration section, reformatted for compactness:

1. Write a two sentence description of your doctoral thesis for yourself, emphasizing a broader context for the research. Why are you doing it?

2. Describe your research for a science professor at another university.

3. Sell the ideas behind your project to a government minister who is visiting your university with the possibility of giving you funding.

4. What direct, patentable, profitable applications does your work have?

5. What engineering (practical) limitations will interfere with this application? How would the scope of your project have to change to meet these requirements?

6. Where will your research be in five years? (Obviously you dont know. But extrapolate, make some educated guesses, state a goal).

7. What other institutions or research groups are working on similar projects as you? Why are/arent you collaborating?

8. Using the sample press releases as a template, write a statement that you would put in a university-wide publication highlighting your research project. Find a partner or two and critique each others product. Make the improvements you feel you need to, and give the text to Chris, Erich, or Kate, who will put it on the MAINZ webpage to showcase your current research activities. Use scrap paper if you need more space.

9. In small groups choose the person EITHER with the research that is closest to commercializable or has the greatest interest in developing a product that will attract outside funds (use your judgement). Develop a business plan outline and sketch a timeline for how this product will be brought to market. Begin to do this by answering such questions as:

What are you selling? It can be an idea, a process, or a product.

What problem does this technology solve?

What is the barrier to entry for a product in this market?

Will there be competition? How will your idea or product be an improvement?

Who will buy it? Military, technology companies, consumers, schools... In the best case, will there be a total worldwide market of 50? 50,000,000?

Where will the initial funds come from?

Independent startup or research unit in a company or university?

How much research is needed from today for a proof of concept?

How long would it take to get a working prototype you could demo to a potential investor or funding agency?

What skill sets would your startup company or research groups co-founders absolutely need? What are your key assets?

Some beginners economics: a back-of-the-envelope budget for feasibility, assuming employee salaries, administrative overhead like corporate taxes and legal fees, price per thing you sell, cost of raw materials, cost of fabrication....

If you wish, even include aesthetic things such as a logo or brand name.

The following is the evaluation form we prepared for our own improvement in future pedagogical exercises, again reformatted for compactness.

Dear thinker,

We worked hard to make sure that you had a productive, enjoyable experience, and we would be grateful for any comments or criticisms you have about the discussions, the projects, or anything else, so next time we can be even better.

Sincerely,

Kate, Chris, and Erich

1. Please circle how much you enjoyed each section from 1 to 7, 7 being the best.

Think tank overall	1	2	3	4	5	6	7
Introductory talk	1	2	3	4	5	6	7
Design project	1	2	3	4	5	6	7
Research project	1	2	3	4	5	6	7
Group presentation	1	2	3	4	5	6	7

What was more enjoyable about your favorite part? What was less enjoyable about your least favorite?

2. Please circle how beneficial you found each section from 1 to 7, 7 being the best.

Think tank overall	1	2	3	4	5	6	7
Introductory talk	1	2	3	4	5	6	7
Design project	1	2	3	4	5	6	7
Research project	1	2	3	4	5	6	7
Group presentation	1	2	3	4	5	6	7

What was more beneficial about your highest ranked part? What was less beneficial about your lowest ranked?

3. Please circle how much time was spent on each section.

Think tank overall	Not enough	Just right	Too much
Introductory talk	Not enough	Just right	Too much
Design project	Not enough	Just right	Too much
Research project	Not enough	Just right	Too much
Group presentation	Not enough	Just right	Too much

4. Is there anything you wish had been included but wasnt? Is there anything you feel was a waste of time?

5. What skills or knowledge did you gain from the Think Tank during this retreat?

6. How relevant did you find the design project? How can you make this outsiders approach to problem solving valuable to you as a scientist in an unrelated field?

7. How relevant did you find the research project? Did you find the information and guidance we provided useful in developing a business plan for a research project, even if it wasnt yours?

8. Are you interested in following up with any literature or seminars related to business plan development or entrepreneurship? In what format?

9. Of all the ideas presented in the research project, whose do you feel has the best chance of success and why? Would you be interested to continue working on it?

10. What ideas do you have to help the Think Tank evolve from a one-day workshop to an Institution of Excellence?

11. How do you volunteer to help the MAINZ student Think Tank in future projects?

Appendix B

Magnetic reversal in islands

Magnetic nanodot arrays [103] have recently drawn significant attention both for fundamental studies of magnetic phenomena as well as for applications in high-density patterned magnetic media. Templated block copolymer (BCP) lithography, where covalently bonded polymers phase separate into ordered periodic nanoscale structures, has been demonstrated as a possible method of fabricating this new generation of media [104]. Recent efforts in templated self-assembly of BCPs have demonstrated a promising route to control bottom-up self-organization processes through top-down lithographic templates. To achieve high densities, features with periodicities on the order of 25 nm and below are required over large areas.

Co(66at%)-Cr(22at%)-Pt(12at%) perpendicularly magnetized layers are deposited on silicon by rf magnetron sputtering at room temperature [105]. These films can be patterned using a spin-cast mask of self-assembled block co-polymer (polystyrene-polymethylmethacrylate (PS-PMMA) or polystyrene-polyferrocenyldimethylsilane (PS-PFS)). The polymer layer phase segregates to a 2-D close-packed monolayer of PFS (or PMMA) spheres in a PS matrix. The PS matrix is then removed and the pattern is transferred to the sample by a series of reactive ion etches. The magnetic islands maintain the perpendicular magnetization from the film, but show an increased coercivity of 800 1650 Oe as compared to 150 Oe in the film.

Time-dependent magnetic measurements show switching volumes V^* on the order of the physical volume of the dots, suggesting that these dots switch their magnetization coherently and independently of each other. To study the effect of island size on the magnetic properties of the arrays, samples were fabricated by using a different molecular weight of the polymer mixture, giving islands $5-15$ nm thick, $20-35$ nm average diameter, and up to $20-100$ nm periodicity [106]. Magnetic analysis suggested and micromagnetic simulation corroborated that the thicker islands reverse their magnetization in a coherent and independent fashion, the exception being the array of 5 nm thick / 28 nm diameter islands, in which inter-island interactions significantly influence the magnetic reversal.

Close-packed arrays of 5-20 nm thick Co and NiFe layers with in-plane magnetization were also fabricated [107]. In contrast to the CoCrPt structures, magnetic characterization showed strong magnetostatic interactions between the dots: the switching volume of NiFe and Co arrays was 26 times the physical volume, suggesting that several dots switch collectively, as in an array of strongly interacting single-domain particles.

First, magnetic reversal in CoCrPt, NiFe, and Co islands grown on SiN membranes and templated by self-assembled BCP lithography will be observed at Beamline 6.1.2, the full-field soft x-ray transmission microscope. The different diameters, thicknesses, and magnetization orientations available to such a flexible and controllable fabrication technique will allow us to map the regimes of coherent vs. collective magnetic switching. Later, spin-polarized Co_2FeSi or similar thin films will be grown on transmission membranes in Mainz and investigated for a world's first demonstration of magnetic reversal and domain wall motion in Heusler compounds.

Zone plate microscopy at XM-1 will be used to directly observe the dependence of the magnetic reversal on the spatial configuration of templated nanostructures. Different molecular weights of PS-PFS or PS-PMMA are used in the fabrication process to achieve the necessary series of size, periodicity, and diameter that will

allow previous mathematical simulations or inferences from bulk magnetometry data to be clarified.

Beamline 6.1.2 has the high spatial resolution ($15-20$ nm typical use, demonstrated resolution 9 nm) necessary to directly view the magnetization in individual pillars, which can be tailored to be $20-50$ nm diameter at a spacing of $20-100$ nm. The circularly polarized soft x-rays of the synchrotron allow systematic studies of the nanoscale magnetism in these transition metal intermetallic magnets, with excellent flux between $600-800$ eV photon energy, near the L-absorption edges of the elements under examination.

No technical obstacles such as signal strength or resolution remain to hinder the direct observation of the magnetization switching and rotation phenomena in perpendicular or in-plane magnetized media created by self-assembled BCP lithography. Single and binary metal samples are prepared and preliminary characterization is undertaken at the Massachusetts Institute of Technology in a research group with the material and computational experience to interpret relevant data. Ternary intermetallic samples are under development.

Bibliography

[1] P.J. Webster. Heusler alloys. *Contemp. Phys.*, 10(6):559–577, 1969.

[2] J. Kübler, A.R. Williams, and C.B. Sommers. Formation and coupling of magnetic moments in Heusler alloys. *Phys. Rev. B*, 28(4):1–11, 1983.

[3] S. Kulkova, S. Eremeev, Q.M. Hu, C.M. Li, and R. Yang. The influence of defects and composition on the magnetic properties of shape memory Heusler alloys. *ESOMAT: European Symposium on Martensitic Transformations*, (02017):1–5, Sept 2009.

[4] I. Galanakis, P.H. Dederichs, and N. Papanikolaou. Slater-Pauling behavior and origin of the half-metallicity of the full-Heusler alloys. *Phys. Rev. B*, 66(174429), 2002.

[5] J.M.D. Coey and S. Sanvito. Magnetic semiconductors and half-metals. *J. Phys. D: Appl Phys*, 37:988–993, 2004.

[6] W. Al-Sawai, H. Lin, R.S. Markiewicz, L.A. Wray, Y. Xia, S-Y. Xu, M.Z. Hasan, and A. Bansil. Topological electronic structure in half-Heusler topological insulators. *Phys. Rev. B*, 82(12):125208:1–5, Sept 2010.

[7] R.A. Dunlap. Magnetic properties of Heusler alloys. *Proc. 10th CF/DRDC Meeting on Naval Applications of Materials Technology*, pages 600–619, 2003.

[8] V. Ksenofontov, K. Kroth, S. Reiman, F. Casper, V. Jung, M. Takahashi, M. Takeda, and C. Felser. Mössbauer spectroscopic study of half-Heusler compounds. *Hyperfine Interact*, 2006.

[9] N.D. Telling, P.S. Keatley, G. van der Laan, R.J. Hicken, E. Arenholz, Y. Sakuraba, M. Oogane, Y. Ando, K. Takanashi, and T. Miyazaki. Evidence of local moment formation in Co-based Heusler alloys. *Phys. Rev. B*, 78(184438):1–7, 2008.

[10] A.T. Zayak, P. Entel, and J.R. Chelikowsky. Minority-spin polarization and surface magnetic enhancement in Heusler clusters. *Phys. Rev. B*, 77(212401):1–4, 2008.

[11] N.D. Telling, P.S. Keatley, L.R. Shelford, E. Arenholz, G. van der Laan, R.J. Hicken, Y. Sakuraba, S. Tsunegi, M. Oogane, Y. Ando, K. Takanashi, and T. Miyazaki. Temperature dependence of the interface moments in Co_2MnSi thin films. *Appl Phys Lett*, 92(192503), 2008.

[12] I. Galanakis, K. Özdoğan, E. Şaşioğlu, and B. Aktaş. *Ab initio* design of half-metallic fully compensated ferrimagnets: the case of Cr_2MnZ (Z=P, As, Sb, and Bi). *Phys. Rev. B*, 75(172405):1–4, 2007.

[13] H-J. Elmers, S. Wurmehl, G.H. Fecher, G. Jakob, C. Felser, and G. Schönhense. Enhanced orbital magnetic moments in the heusler compounds Co_2CrAl, $Co_2Cr_{0.6}Fe_{0.4}Al$, Co_2FeAl. *J. Magn. Magn. Mater.*, 272-276:758–759, 2004.

[14] I. Galanakis. Orbital magnetism in the half-metallic Heusler alloys. *Phys. Rev. B*, 71(012413):1–4, 2005.

[15] D.E. Laughlin, K. Srinivasan, M. Tanase, and L. Wang. Crystallographic aspects of $L1_0$ magnetic materials. *Scripta Materialia*, 53:383–388, April 2005.

[16] O. Heczko, N. Scheerbaum, and O. Gutfleisch. *Nanoscale Magnetic Materials and Applications*, chapter 14: Magnetic shape memory phenomena, pages 399–440. Springer, 2009.

[17] R.C. O'Handley, S.J. Murray, M. Marioni, H. Nembach, and S.M. Allen. Phenomenology of giant magnetic-field-induced strain in ferromagnetic shape-memory materials (invited). *J. Appl. Phys.*, 87(9):4712–6, May 2000.

[18] K. Bhattacharya. *Microstructure of Martensite: Why It Forms and How It Gives Rise to the Shape-Memory Effect*. Oxford University Press, 2003.

[19] K. Ullakko, J.K. Huang, C. Kantner, R.C. O'Handley, and V.V. Kokorin. Large magnetic-field-induced strains in NiMnGa single crystals. *Appl Phys Lett*, 69(13), 1996.

[20] H.J. Yu, H. Fu, Z.M. Zeng, J.X. Sun, Z.G. Wang, W.L. Zhou, and X.T. Zu. Phase transformations and magnetocaloric effect in NiFeGa ferromagnetic shape memory alloy. *J. Alloys and Compounds*, 477:732–735, 2009.

[21] H.Z. Luo, G.D. Liu, F.B. Meng, S.J. Li, W. Zhu, G.H. Wu, X.X. Zhu, and C.B. Jiang. Electronic structure and magnetism of the Heusler alloy Mn_2NiAl: a theoretical study of the shape-memory behavior. *Phys. B: Cond. Mat.*, 405(15):3092–3095, 2010.

[22] C. A. Jenkins. *Thin film Heusler compounds $Mn_{3-x}Ni_xGa$.* PhD thesis, University of California, Berkeley, 2009.

[23] M.A. Uijttewaal, T. Hickel, J. Neugebauer, M.E. Gruner, and P. Entel. Understanding the phase transitions of the Ni_2MnGa magnetic shape memory system from first principles. *Phys. Rev. Lett.*, 102(035702):1–4, 2009.

[24] G.D. Liu, X.F. Dai, S.Y. Yu, Z.Y. Zhu, J.L. Chen, G.H. Wu, H. Zhu, and J.Q. Xiao. Physical and electronic structure and magnetism of Mn_2NiGa: Experiment and density-functional theory calculations. *Phys. Rev. B*, 74(054435):1–8, 2006.

[25] O. Heczko, L. Straka, V. Novak, and S. Fähler. Magnetic anisotropy of non-modulated Ni-Mn-Ga martensite revisited. *J. Appl. Phys.*, 107(09A914):1–3, 2010.

[26] G. Jakob, T. Eichhorn, M. Kallmayer, and H-J. Elmers. Correlation of electronic structure and martensitic transition in epitaxial Ni_2MnGa films. *Phys. Rev. B*, 76(174407), 2007.

[27] J.W. Dong, J.Q. Xie, J. Lu, C. Adelmann, C.J. Palmstrøm, J. Cui, Q. Pan, T.W. Shield, R.D. James, and S. McKernan. Shape memory and ferromagnetic shape memory effects in single-crystal Ni_2MnGa thin films. *J. Appl. Phys.*, 95(5):2593–2600, March 2004.

[28] A. Backen, S.R. Yeduru, M. Kohl, S. Baunack, A. Diestel, B. Holzapfel, L. Schultz, and S. Fähler. Comparing properties of substrate-constrained and freestanding epitaxial Ni-Mn-Ga films. *Acta Materialia*, 58:3415–3421, 2010.

[29] J.R. Sun, B.G. Shen, and F.X. Hu. *Nanoscale Magnetic Materials and Applications*, chapter 15: Magnetocaloric effect and materials, pages 441–482. Springer, 2009.

[30] A. Planes and Ll. Mañosa. Magnetocaloric effect in ferromagnetic shape-memory alloys. *J. Phys. Conf. Series*, 165(012050), 2009.

[31] M. Quintero, J. Sacanell, L. Ghivelder, A.M. Gomes, A.G. Leyva, and F. Parisi. Magnetocaloric effect in manganites: metamagnetic transitions for magnetic refrigeration. *Appl Phys Lett*, 97(121916):1–3, 2010.

[32] A.K. Pathak, I. Dubenko, H.E. Karaca, S. Stadler, and N. Ali. Large inverse magnetic entropy changes and magnetoresistance in the vicinity of a field-induced martensitic transformation in $Ni_{50-x}Co_xMn_{32-y}Fe_yGa_{18}$. *Appl Phys Lett*, 97(062505):1–3, 2010.

[33] V.K. Pecharsky and K.A. Gschneider. Giant magnetocaloric effect in $Gd_5(Si_2Ge_2)$. *Phys. Rev. Lett.*, 78(23):4494–7, 1997.

[34] M.P. Annaorazov, S.A. Nikitin, A.L. Tyurin, K.A. Asatryan, and A.Kh. Dovletov. Anomalously high entropy change in FeRh alloy. *J. Appl. Phys.*, 79(3):1689–1695, 1996.

[35] D.D. Awschalom and M.E. Flatté. Challenges for semiconductor spintronics. *Nature Physics*, 3:153–159, 2007.

[36] I. Zutic, J. Fabian, and S. Das Sarma. Spintronics: Fundamentals and applications. *Reviews of Modern Physics*, 76(2):323–410, 2004.

[37] C. Felser, G.H. Fecher, and B. Balke. Spintronics: A challenge for materials science solid state chemistry. *Angew. Chem. Int. Ed*, 46:668–699, 2007.

[38] N. Logoboy, B. Ya. Shapiro, and E.B. Sonin. Shape-dependent depinning of a domain wall by a magnetic field and a spin-polarized current. *Phys. Rev. B*, 82(094419):1–8, Sept 2010.

[39] C.G.F. Blum, C. A. Jenkins, J. Barth, C. Felser, S. Wurmehl, G. Friemel, C. Hess, G. Behr, B. Büchner, A. Reller, S. Riegg, S.G. Ebbinghaus, T. Ellis, P.J. Jacobs, J.T. Kohlhepp, and H.J.M. Swagten. Highly ordered, half-metallic Co_2FeSi single crystals. *Appl Phys Lett*, 95(161903):1–3, October 2009.

[40] J. Fabian, editor. *Modern Aspects of Spin Physics*, volume 712, Berlin, February 2007. Springer.

[41] M.N. Baibich, J.M. Broto, A. Fert, F. Nguyen Van Dau, F. Petroff, P. Etienne, G. Creuzet, A. Friederich, and J. Chazelas. Giant magnetoresistance of (001)Fe/(001)Cr magnetic superlattices. *Phys. Rev. Lett.*, 61(21):1–4, 1988.

[42] D. Cahen and A. Kahn. Electron energetics at surfaces and interfaces: Concepts and experiments. *Adv. Mater.*, 15(4):271–7, Feb 17 2003.

[43] A. Gloskovskii, J. Barth, B. Balke, G.H. Fecher, C. Felser, F. Kronast, R. Ovsyannikov, H.A. Dürr, W. Eberhard, and G. Schönhense. A spatially resolved investigation of the local, micro-magnetic domain structure of single and polycrystalline Co_2FeSi. *J. Phys. D: Appl Phys*, 40:1570–1575, 2007.

[44] W.H. Butler, X-G. Zhang, T.C. Schulthess, and J.M. MacLaren. Spin-dependent tunneling conductance of Fe—MgO—Fe sandwiches. *Phys. Rev. B*, 63(054416):1–12, 2001.

[45] H. Ohno. Physics and material science of MgO-CoFeB structures. In *7th International Symposium on Metallic Multilayers*, 2010.

[46] J.C. Slonczewski. Current-driven excitation of magnetic multilayers. *J. Magn. Magn. Mater.*, 159:L1–L7, 1996.

[47] M. Kallmayer, P. Klaer, H. Schneider, E. Arbelo Jorge, C. Herbort, G. Jakob, M. Jourdan, and H-J. Elmers. Spin-resolved unoccupied density of states in epitaxial Heusler-alloy films. *Phys. Rev. B*, 80(020406(R)):1–4, 2009.

[48] H.Z. Luo, H.W. Zhang, Z.Y. Zhu, L. Ma, S.F. Xu, G.H. Wu, X.X. Zhu, C.B. Jiang, and H.B. Xu. Half-metallic properties for the Mn_2FeZ (Z=Al,Ga,Si,Ge,Sb) Heusler alloys: a first-principles study. *J. Appl. Phys.*, 103(083908):1–7, 2008.

[49] N.D. Telling, P.S. Keatley, G. van der Laan, R.J. Hicken, E. Arenholz, Y. Sakuraba, M. Oogane, Y. Ando, and T. Miyazaki. Interfacial structure and half-metallic ferromagnetism in Co_2MnSi-based magnetic tunnel junctions. *Phys. Rev. B*, 74(224439):1–7, 2006.

[50] S. Tsunegi, Y. Sakuraba, M. Oogane, K. Takanashi, and Y. Ando. Large tunnel magnetoresistance in magnetic tunnel junctions using a Co_2MnSi Heusler alloy and a MgO barrier. *Appl Phys Lett*, 93:112506, 2008.

[51] T. Kubota, S. Tsunegi, M. Oogane, S. Mizukami, T. Miyazaki, H. Naganuma, and Y. Ando. Half-metallicity and Gilbert damping constant in $Co_2Fe_xMn_{1-x}Si$ Heusler alloys depending on the film composition. *Appl Phys Lett*, 94(122504):1–3, 2009.

[52] B. Balke, G.H. Fecher, J. Winterlik, and C. Felser. Mn_3Ga, a compensated ferrimagnet with high Curie temperature and low magnetic moment for spin torque applications. *Appl Phys Lett*, 90:152504, 2007.

[53] J. Winterlik, B. Balke, G.H. Fecher, C. Felser, M.C.M. Alves, F. Bernardi, and J. Morais. Structural, electronic, and magnetic properties of tetragonal $Mn_{3-x}Ga$: experiments and first-principles calculations. *Phys. Rev. B*, 77(054406), 2008.

[54] W. Van Roy, J. De Boeck, H. Bender, C. Bruynseraede, A. Van Esch, and G. Borghs. Structural and magnetic investigations of epitaxial ferromagnetic MnAl films grown on GaAs/AlAs by molecular-beam epitaxy. *J. Appl. Phys.*, 78(1):398–404, March 1995.

[55] F. Wu, S. Mizukami, D. Watanabe, H. Naganuma, M. Oogane, Y. Ando, and T. Miyazaki. Epitaxial $Mn_{2.5}Ga$ thin films with giant perpendicular magnetic anisotropy for spintronic devices. *Appl Phys Lett*, preprint, 2009.

[56] F. Wu, E.P. Sajitha, S. Mizukami, D. Watanabe, T. Miyazaki, H. Naganuma, M. Oogane, and Y. Ando. Electrical transport properties of perpendicular magnetized Mn-Ga epitaxial films. *Appl Phys Lett*, 96(042505), 2010.

[57] European School of Magnetism: New experimental approaches to magnetism. *Magnetic imaging by LEEM, X-PEEM, x-ray microscopy, and x-ray holography*, Constanta, 2005.

[58] T. Omori, K. Watanabe, R.Y. Umetsu, R. Kainuma, and K. Ishida. Martensitic transformation and magnetic field induced strain in fe–mn–ga shape memory alloy. *Appl Phys Lett*, 95(082508), 2009.

[59] J.M. Wang, C.B. Jiang, R. Techapiesancharoenkij, D. Bono, S.M. Allen, and R.C. O'Handley. Anomalous magnetizations in melt spinning Ni-Mn-Ga. *J. Appl. Phys.*, 106(2):023923, August 2009.

[60] P. Nachimuthu, J.H. Underwood, C.D. Kemp, E.M. Gullikson, D.W. Lindle, D.K. Shuh, and R.C.C. Perera. Performance characteristics of beamline 6.3.1 from 200 eV to 2000 eV at the Advanced Light Source. In *AIP Conf. Proc.*, volume 705, page 454, 2004.

[61] M. van Veenendaal, J.B. Goedkoop, and B.T. Thole. Polarized x-ray fluorescence as a probe of ground state properties. *Phys. Rev. Lett.*, 77:1508–1511, August 1996.

[62] J. Stöhr and H.C. Siegmann. *Magnetism: from fundamentals to nanoscale dynamics*, volume 152. Springer, 2006.

[63] M.W. Haverkort, N. Hollman, I.P. Krug, and A. Tanaka. Symmetry analysis of magneto-optical effects: The case of x-ray diffraction and x-ray absorption at the transition metal $L_{2,3}$ edge. *Phys. Rev. B*, 82(094403):1–14, 2010.

[64] G. van der Laan. *Magnetism: a synchrotron radiation approach*, chapter Hitchhiker's guide to multiplet calculations, pages 142–168. Springer, 2006.

[65] E. Stavitski and F.M.F. de Groot. The CTM4XAS program for EELS and XAS spectral shape analysis of transition metal L edges. *Micron*, 41:687, 2010.

[66] M. Kallmayer, P. Pörsch, T. Eichhorn, H. Schneider, C. A. Jenkins, G. Jakob, and H-J. Elmers. Compositional dependence of element-specific magnetic moments in Ni_2MnGa films. *J. Phys. D: Appl Phys*, 42(084008):1–8, 2009.

[67] A. Ayuela, J Enkovaara, and R.M. Nieminen. Ab initio study of tetragonal variants in Ni_2MnGa alloy. *J. Phys. Condens. Mater.*, 14:5325–5336, 2002.

[68] G. van der Laan, B.T. Thole, G.A. Sawatzky, J.B. Goedkoop, J.C. Fuggle, J.-M. Esteva, R. Karnatak, J.P. Remeika, and H.A. Dabkowska. Experimental proof of magnetic x-ray dichroism. *Phys. Rev. B*, 34(9):6529, November 1986.

[69] G. van der Laan and B.T. Thole. Strong magnetic x-ray dichroism in $2p$ absorption spectra of $3d$ transition-metal ions. *Phys. Rev. B*, 43(16):13401, June 1991.

[70] R. Nakajima, J. Stöhr, and Y.U. Idzerda. Electron-yield saturation effects in L-edge x-ray magnetic circular dichroism spectra of Fe, Co, and Ni. *Phys. Rev. B*, 59(9):6421–6429, 1999-I.

[71] E. Arenholz, G. van der Laan, R.V. Chopdekar, and Y. Suzuki. Angle-dependent Ni^{2+} x-ray magnetic linear dichroism: interfacial coupling revisited. *Phys. Rev. Lett.*, 98(197201):1–4, 2007.

[72] B.T. Thole, P. Carra, F. Sette, and G. van der Laan. X-ray circular dichroism as a probe of orbital magnetization. *Phys. Rev. Lett.*, 68(12):1943–6, 1992.

[73] W.L. O'Brien and B.P. Tonner. Orbital and spin sum rules in x-ray magnetic circular dichroism. *Phys. Rev. B*, 50(17):12672, November 1994.

[74] C. Piamonteze, P. Miedema, and F.M.F. de Groot. Accuracy of the spin sum rule in XMCD for the transition-metal L edges from manganese to copper. *Phys. Rev. B*, 80(184410), 2009.

[75] G. van der Laan. Sum rules and beyond. *J. Electron Spectroscopy and Related Phenomena*, 101-103:859–868, June 1999.

[76] W. Kuch. Peem: Facts and fiction. Presentation, 2007.

[77] H.T. Nembach, T.J. Silva, J.M. Shaw, M.L. Schneider, M.J. Carey, S. Maat, and J.R. Childress. Perpendicular ferromagnetic resonance measurements of damping and the Landé g-factor in sputtered $(Co_2Mn)_{1-x}Ge_x$ thin films. *Phys. Rev. B*, in press.

[78] J. Gutiérrez, J.M. Barandiarán, P. Lázpita, C. Seguí, and E. Cesari. Magnetic properties of a rapidly quenched Ni-Mn-Ga shape memory alloy. *Sensors and Actuators A*, 129:163–166, 2006.

[79] J. Gutiérrez, P. Lázpita, J.M. Barandiarán, M.L. Fernandez-Gubieda Ruiz, J. Chaboy, and N. Kawamura. Annealing influence on the atomic ordering and magnetic moment in a Ni-Mn-Ga alloy. *J. Magn. Magn. Mater.*, 316:E610–E613, 2007.

[80] M.L. Richard, J. Feuchtwanger, S.M. Allen, R.C. O'Handley, P. Lazpita, J.M. Barandiarán, J. Gutierrez, B. Ouladdiaf, C. Mondelli, T. Lograsso, and D. Schlagel. Chemical order in off-stoichiometric Ni-Mn-Ga ferromagnetic shape-memory alloys studied with neutron diffraction. *Phil. Mag*, 87(23):3437–3447, 2007.

[81] P. Lázpita, J.M. Barandiarán, J. Gutiérrez, M.L. Richard, S.M. Allen, and R.C. O'Handley. Magnetic and structural properties of non-stoichiometric Ni-Mn-Ga ferromagnetic shape memory alloys. *European Physics Journal, Special Topics*, 158:149–154, 2008.

[82] J. Chaboy, P. Lázpita, J.M. Barandiarán, J. Gutiérrez, M.L. Fernandez-Gubieda Ruiz, and N. Kawamura. XAS and XMCD study of the influence of annealing on the atomic ordering and magnetism in an NiMnGa alloy. *J. Phys. Condens. Mater.*, 21:016002, 2009.

[83] G. Jakob and H-J. Elmers. Epitaxial films of the magnetic shape memory material Ni_2MnGa. *J. Magn. Magn. Mater.*, 310:2779–2781, 2007.

[84] M. Kallmayer, K. Hild, T. Eichhorn, H. Schneider, G. Jakob, A. Conca, M. Jourdan, H-J. Elmers, A. Gloskovskii, S. Schuppler, and P. Nagel. Solid state reaction at the interface between Heusler alloys and Al cap accelerated by elevated temperature and rough surface. *Appl Phys Lett*, 91(192501), 2007.

[85] P. Pörsch, M. Kallmayer, T. Eichhorn, G. Jakob, H-J. Elmers, C.A. Jenkins, C. Felser, R. Ramesh, and M. Huth. Suppression of martensitic phase transition at the Ni_2MnGa film surface. *Appl Phys Lett*, 93(022501), 2008.

[86] S. Aksoy, T. Krenke, M. Acet, E.F. Wasserman, X. Moya, Ll. Mañosa, and A. Planes. Magnetization easy-axis in martensitic Heusler alloys estimated by strain measurements under magnetic-field. *Appl Phys Lett*, 91:251915, 2007.

[87] Z. Islam, D. Haskel, J.C. Lang, G. Srajer, Y. Lee, B.N. Harmon, A.I. Goldman, D.L. Schlagel, and T.A. Lograsso. An x-ray study of non-zero nickel moment in a ferromagnetic shape-memory alloy. *J. Magn. Magn. Mater.*, 303:20–25, 2006.

[88] S. Roy, E. Blackburn, S.M. Valvidares, M.R. Fitzsimmons, S.C. Vogel, M. Khan, I. Dubenko, S. Stadler, N. Ali, S.K. Sinha, and J.B. Kortright. Delocalization and hybridization enhance the magnetocaloric effect in Cu-doped Ni_2MnGa. *Phys. Rev. B*, 79:235127, 2009.

[89] K. Miyamoto, A. Kimura, K. Iori, K. Sakamoto, T. Xie, T. Moko, S. Qiao, M. Taniguchi, and K. Tsuchiya. Element-resolved magnetic moments of Heusler-type ferromagnetic ternary alloy Co_2MnGe. *J. Phys. Condens. Mater.*, 16(S5797-5800), 2004.

[90] S. Maat, M.J. Carey, S. Chandrashekariaih, J. Katine, X. Liu, N. Smith, P. Vanderheijden, K. Vo, and J.R. Childress. Advanced ferromagnetic alloys and multilayer structures for CPP-GMR magnetic recording read heads. *Intermag Digest*, EA-03, 2009.

[91] A. Nefedov, J. Grabis, A. Bergmann, K. Westerholt, and H. Zabel. Soft x-ray resonant magnetic scattering studies on Co_2MnGe Heusler films. *Phys. B: Cond. Mat.*, 345(250), 2004.

[92] W. Zhu, E.K. Liu, L. Feng, X.D. Tang, J.L. Chen, G.H. Wu, H.Y. Liu, and F.B. Meng. Magnetic-field-induced transformation in FeMnGa alloys. *Appl Phys Lett*, 95(222512):1–3, Dec 2009.

[93] G.D. Liu, J.L. Chen, Z.H. Liu, X.F. Dai, G.H. Wu, B. Zhang, and X.X. Zhang. Martensitic transformation and shape memory effect in a ferromagnetic shape memory alloy: Mn_2NiGa. *Appl Phys Lett*, 87:262504, 2005.

[94] C. A. Jenkins, R. Ramesh, M. Huth, T. Eichhorn, P. Pörsch, H. J. Elmers, and G. Jakob. Growth and magnetic control of twinning structure in thin films of Heusler shape memory compound Ni_2MnGa . *Appl Phys Lett*, 93(234101), 2008.

[95] Y.W. Lai, R. Schäfer, L. Schultz, and J. McCord. Volume magnetic domain mirroring in magnetic shape memory crystals. *Appl Phys Lett*, 96(022507):1–3, January 2010.

[96] S. Kaufmann, U.K. Rößler, O. Heczko, M. Wuttig, J. Buschbeck, L. Schultz, and S. Fähler. Adaptive modulations of martensites. *Phys. Rev. Lett.*, 104(2010):1–4, April 2010.

[97] G.R. Harp, S.S.P. Parkin, W.L. O'Brien, and B.P. Tonner. Induced Rh magnetic moments in Fe-Rh and Co-Rh alloys using x-ray magnetic circular dichroism. *Phys. Rev. B*, 51(17):1–4, May 1995.

[98] N. Xing, H. Li, J. Dong, R. Long, and C. Zhang. First-principle prediction of half-metallic ferrimagnetism of the Heusler alloys Mn_2CoZ (Z=Al, Ga, Si, Ge) with a high-ordered structure. *Comput. Mater. Sci.*, 42:600–605, 2008.

[99] P. Klaer, M. Kallmayer, H-J. Elmers, L. Basit, J. Thöne, S. Chadov, and C. Felser. Localized magnetic moments in the Heusler alloy Rh_2MnGe. *J. Phys. D: Appl Phys*, 42(084001), 2009.

[100] P. Klaer, E. Arbelo Jorge, M. Jourdan, W.H. Wang, H. Sukegawa, K. Inomata, and H-J. Elmers. Temperature dependence of the XA spectra in the ferromagnetic Heusler Mn_2VAl and Co_2FeAl. *Phys. Rev. B*, 77(014424), 2010.

[101] M. Meinert, J. Schmalhorst, and G. Reiss. Exchange interactions and Curie temperatures in Mn_2CoZ compounds. *http://arxiv.org/pdf/1012.3261v1*, 2010.

[102] G.D. Liu, X.F. Dai, H.Y. Liu, J.L. Chen, Y.X. Li, G. Xiao, and G.H. Wu. Mn_2CoZ (Z=Al, Ga, In, Si, Ge, Sn, Sb) compounds: structural, electronic, and magnetic properties. *Phys. Rev. B*, 77(014424):1–12, 2008.

[103] C.A. Ross and J.Y. Cheng. Patterned magnetic media made by self-assembled block-copolymer lithography. *MRS Bulletin*, 33:838–845, 2008.

[104] J.Y. Cheng, C.A. Ross, H.I. Smith, and E.L. Thomas. Templated self-assembly of block copolymers: top-down helps bottom-up. *Adv. Mater.*, 18(19):2505–2521, 2006.

[105] J.Y. Cheng, C.A. Ross, V.Z.H. Chan, E.L. Thomas, R.G.H. Lammertink, and G.J. Vancso. Formation of cobalt magnetic dot array via block copolymer lithography. *Adv. Mater.*, 13(15):1174–1178, 2001.

[106] F. Ilievski, C.A. Ross, and G.J. Vancso. Magnetic reversal phenomena of perpendicular magnetic islands fabricated by block copolymer lithography. *J. Appl. Phys.*, 103(07C520).

[107] J.Y. Cheng, C.A. Ross, and A. Mayes. Nanostructure engineering by templated self-assembly. *Nature Materials*, 3:823–828, 2004.